Investigation of Ion and Electron Kinetic Phenomena in Capacitively Coupled Radio-Frequency Plasma Sheaths: A Simulation Study

Sarveshwar Sharma

November 2012

Investigation of Ion and Electron Kinetic Phenomena in Capacitively Coupled Radio-Frequency Plasma Sheaths: A Simulation Study

A thesis for the degree of

PHILOSOPHIAE DOCTOR

Presented to

DUBLIN CITY UNIVERSITY

By

Sarveshwar Sharma

School of Physical Sciences

Dublin City University

Research Supervisor:

Prof. Miles M. Turner

External Examiner: Dr. Pascal Chabert

Internal Examiner: Dr. Paul van Kampen

November 2012

Declaration

I hereby certify that this material which I now submit for assessment on the programme of study leading to the award of Philosophiae Doctor is entirely my own work, that I have exercised reasonable care to ensure that the work is original, and does not to the best of my knowledge breach any law of copyright, and has not been taken from the work of others save and to the extent that such work has been cited and acknowledged within the text of my work.

Signed: .....

Sarveshwar Sharma

Student ID. No.: 58115013

Date: November 2012

This thesis is dedicated to my family members for their love, endless support, and encouragement.

Abstract

Stochastic heating is an important phenomenon in low-pressure radio-frequency (RF) capacitive discharges. Recent theoretical work on this problem using several different approaches has produced results that are broadly in agreement in-so-far as scaling with the discharge parameters is concerned, but there remains some disagreement in detail concerning the absolute size of the effect. Here we report a simulation study for single and dual frequency capacitive discharges with two main aims.

In the case of single frequency discharge, this work investigates the dependence of stochastic heating on various discharge parameters by scaling of these parameters with the help of particle-in-cell (PIC) simulation. This research work produces a relatively extensive set of simulation data that may be used to validate theories over a wide range of parameters. The analytical models are satisfactory for intermediate current density amplitude $\tilde{J}_0$ (or control parameter H) and in agreement with PIC results. However in extreme cases new physical effects appear (like field reversal, electron trapping, reflection of ions etc.) and the simulation results deviate from existing analytical models. The dependence of stochastic heating on applied frequency is also investigated. The second aim is to study any evidence of wave emission with a frequency near the electron plasma frequency (ω_{pe}) at the sheath edge. This is the result of a progressive breakdown of quasi-neutrality close to the electron sheath edge. These waves are damped during their propagation from the sheath towards the bulk plasma. The damping occurs because of the Landau damping or some related mechanism. This research work reports that the emission of waves is associated with a field reversal during the expansion phase of the sheath. Trapping of electrons

near to this field reversal region is observed. Calculation shows that these waves are electron plasma waves.

In the dual frequency case, this research has produced a relatively extensive set of simulation data and shown that the dual-frequency analytical model is in agreement for wide range of parameters. However, in extreme cases, new phenomena like the presence of strong field reversal and the reflection of ions appear and the simulation results deviate from the analytical model. A further aim is the investigation of the presence of strong wave phenomena during the expanding and collapsing phase of the low frequency sheath. The characteristics of waves in the dual-frequency case is entirely different from the single-frequency case. The presence of electron trapping near to the field reversal regions is also observed at multiple times of an RF period. The frequency of these waves are calculated and to be of the order of ω_{pe}.

Acknowledgements

The present research work could not have been completed without the support of the following people whom I wish to thank.

First of all, I wish to thank Prof. Miles Turner, Director of National Centre for Plasma Science and Technology (NCPST) for providing me with the opportunity to pursue a Ph.D. in Dublin City University (DCU), Ireland. His availability and important advice encouraged me to progress rapidly in my understanding of the modelling of sheath physics. His ideas and practical advice contributed enormously to the success of this work. His ability to simplify complex problems and capture their essence in the frame of a simple model helped me greatly. I wish to thank him also for giving me numerous occasions to present my work at international conferences, where I was able to forge links with the rest of the plasma physics community. I adopted his great enthusiasm for science, he taught me to live and love my profession. Thank you!

I will be ever obliged to DCU in general and the NCPST in particular for having provided me with such an intellectually stimulating environment that is highly conducive to academic growth. I am very thankful to Prof. Greg Hughes, Head

of the school of Physics for his kind support. I would like to offer warm thanks to the NCPST operational manager, Ms. Samantha Fahy, the secretaries, Ms. Patricia James and administrator, Ms. Sarah Hayes and Ms. Sheila Boughton; and the School of Physics secretary, Ms. Lisa Peyton. I would like to thank all the library staff for their kind help. I am thankful to Mr. Ray Murphy for his technical assistance. I am also thankful to Dr. Claire McKenna for helping me in my thesis correction.

I would like to express my gratitude to Prof. P. K. Kaw, Prof. Abhijit Sen, Prof. Amita Das and Dr. Sudip Sengupta from my parent institute, Institute for Plasma Research (IPR), for constant encouragement. I am also thankful to Dr. Shantanu Karkari for fruitful scientific discussions.

A thesis would not be possible without the support of family and friends. I am grateful to many of my friends cum colleagues for fruitful scientific discussions and for maintaining a friendly environment at our work place. I particularly wish to thank Huw Leggate, for being constantly present to discuss plasma physics, world politics and cricket. I also especially wish to thanks Sean, Nina, Gurusharan, Nishant, Samir, Mubarak and Zhenning Su.

I would like to thank my wife, Sanju, for her affection, her support and most importantly her patience throughout the years and in particular during the writing of this thesis. Bhavya, my son, the axis of my life, also relaxed me during the tough time of research work. I owe my deepest gratitude to my sister and my brother for their support. And last, but by no means least, I wish to thank my grandparents, my father, Mr. Mahaveer Prasad Sharma, and my mother, Ms. Shanti, for their valuable teachings, love, and blessings which always help me to achieve my goals. I would like to dedicate this thesis to them.

Sarveshwar Sharma

Contents

List of Tables

List of Figures

List of Publications/Awards/Memberships

Peer Reviewed Publications and Conference Proceedings

1. S. Sharma, M. M. Turner: Simulation study of stochastic heating in single frequency capacitively coupled discharges with critical evaluation of analytical models, Plasma Sources Science and Technology (under preparation).

2. S. Sharma, M. M. Turner: Simulation study of wave phenomena from the sheath edge in single frequency capacitively coupled plasma discharges, Phys. of Plasmas (under preparation).

3. S. Sharma, M. M. Turner: Simulation study of stochastic heating by scaling of parameters in dual frequency capacitively coupled discharges, J. of Phys. D: Applied Phys. (under preparation).

4. S. Sharma, M. M. Turner: Simulation study of wave phenomena from the sheath edge in dual frequency capacitively coupled plasma discharges, J. of Phys. D: Applied Phys. (under preparation).

5. S. Sharma, M. M. Turner: Simulation study of wave emission from the sheath edge in capacitively coupled discharges, 30th International conference on phe-

nomena in ionized gases (ICPIG), Belfast, United Kingdom, 28th August to 2nd September 2011.

6. S. Sharma, M. M. Turner: Simulation study of stochastic heating by scaling of parameters in capacitively coupled discharges, 30th International conference on phenomena in ionized gases (ICPIG), Belfast, United Kingdom, 28th August to 2nd September 2011.

7. S. Sharma, M. M. Turner: Study of stochastic heating in single frequency capacitive discharges, 37th European physical society conference on plasma physics, P1.323, Dublin City University, Dublin, Ireland, 21-25 June 2010.

Contributed Conference Oral Presentations with Abstracts Only

1. Sarveshwar Sharma, Miles Turner: Simulation study of wave phenomena from the sheath edge in single frequency capacitively coupled plasma discharges, FUSION DAY AT DCU: Sustainable Energy from Plasmas, Dublin City University, Ireland, October 1st 2012.

2. S. Sharma, M. M. Turner: Simulation study of collisionless heating in single frequency capacitively coupled discharges, 64th Annual Gaseous Electronics Conference, Salt Lake City, Utah, USA, 14th November to 18th November 2011.

3. S. Sharma, M. M. Turner: Electron heating in capacitive discharges, Workshop on Radio Frequency Discharges, NCPST, Dublin City University, Ireland, 26th August to 27th August 2011.

Contributed Conference Poster Presentations with Abstracts Only

1. S. Sharma, M. M. Turner: Study of Stochastic Heating Using Particle-in-Cell Simulation in Single Frequency Capacitively Coupled Plasma Discharges, 39th IEEE International Conference on Plasma Science (ICOPS), Edinburgh International Conference Centre (EICC), Edinburgh, UK, 8th July to 12th July 2012.

2. S. Sharma, M. M. Turner: Simulation Study of Stochastic Heating in Dual Frequency Capacitively Coupled Plasma Discharges, 39th IEEE International Conference on Plasma Science (ICOPS), Edinburgh International Conference Centre (EICC), Edinburgh, UK, 8th July to 12th July 2012.

3. S. Sharma, M. M. Turner: Simulation study of collisionless heating in capacitively coupled discharges, 63rd Annual Gaseous Electronics Conference and 7th International Conference on Reactive Plasmas, Laboratoire de Physique des Plasmas, Ecole Ploytechnique-CNRS, Paris, France, 04th October to 08th October 2010.

Poster Presentations

1. Sarveshwar Sharma, Miles Turner: Simulation study of stochastic heating, wave phenomenon and signature of ion reflection from sheath edge in capacitively coupled plasma discharges, BOC Gases Poster Competition, Dublin City University, Ireland, 13th April 2012.

2. Sarveshwar Sharma, Miles Turner: Simulation study of collisionless heating in capacitively coupled discharges, 2nd NCPST Postgraduate Poster Competition, Dublin City University, Ireland, 08th December 2010.

3. Sarveshwar Sharma, Miles Turner: Simulation study of collisionless heating in capacitively coupled discharges, 15th European Summer School on Low Temperature Plasma Physics: Basics and Applications, and Master Class on Atmospheric Pressure Plasmas, Physikzentrum, Bad Honnef, Germany, 9th October to 17th October 2010.

4. Sarveshwar Sharma, Miles Turner: Simulation study of collisionless heating in capacitively coupled discharges, BOC Gases Poster Competition, Dublin City University, Ireland, 24th September 2010.

Academic Awards and Achievements

1. First prize winner of 3rd NCPST postgraduate poster competition at Dublin City University, Ireland, 20th December 2011. Poster titled, "Simulation Study of Stochastic Heating, Wave Phenomena and Signature of Ion Reflection from sheath edge in Capacitively Coupled Plasma".

2. Student Travel Support to attend 64th Annual Gaseous Electronics Conference, Salt Lake City, Utah, USA, 14th November to 18th November 2011.

Organization Memberships

1. Member of IEEE.

2. Associate member of Institute of Physics (IOP) (2011-2012).

3. Life time member of Plasma Science Society of India (PSSI).

Symbols and Abbreviations

IC	Integrated Circuit	1
CCP	Capacitively Coupled Plasma	2
RF	Radio Frequency	2
$PECVD$	Plasma Enhanced Chemical Vapor Deposition	3
$P3I$	Plasma Immersion Ion Implantation	3
PIC	Particle-In-Cell	4
SOL	Scrape-off Layer	4
$ICRF$	Ion Cyclotron Range of Frequency	4
f_{pi}	ion oscillation frequency (Hz)	5
f_{pe}	electron oscillation frequency (Hz)	5
l	length (m)	6
ν_m	collision frequency (Hz)	6
eV	electron volt	7
f_{rf}	rf frequency (Hz)	7
$\bar{v}_i$	mean ion thermal velocity (ms^{-1})	8
n_i	ion density (m^{-3})	8

LIST OF FIGURES

LIST OF FIGURES

CHAPTER 1

Introduction

Plasmas are widely used for industrial purposes and one of most crucial applications is the manufacture of integrated circuits (IC). As a result there has been a large amount of research carried out in both industry and academia on how to improve plasma processes. There are various applications of plasmas in the domain of surface processing and *etching* is one of the most important processes. Plasma etching is defined as the removal of material from a surface either by chemical or physical means [2, 3]. *Etch rate uniformity*, *selectivity* and *anisotropy* are the three most important parameters for etching [4, 5]. In semiconductor processing the *etch rate uniformity* is a major interest, because of significant impact on manufacturing yield. If the material is removed in vertical direction only and the horizontal etch rate is zero, is defined as *anisotropic etching*. Plasma processing is the only commercially viable technology for anisotropic removal of material from surfaces and used to fabricate integrated circuits [6]. *Selectivity* (*i.e.* removing one type of material without

affecting other material) is the another key process parameter for integrated circuit (IC) manufacturing. In fact highly-selective plasma etch processes are very difficult to design [7]. At low frequencies, capacitively coupled plasma (CCP) discharges are immensely popular in semiconductor industry because of low cost and robust uniformity over a large area. We will discuss the working mechanism and merits of CCPs here.

When a sufficiently high potential difference (few hundred to thousands of Volts) is applied between two electrodes located in gas, the gas will break down into electrons and positive ions. The electrons are accelerated by the electric field in front of the cathode and collide with the gas atoms. Inelastic collisions *i.e.* excitation and ionization are most important collisions. The emission of radiation because of excitation and de-excitations of atoms are responsible of the 'glow' discharges. Ionizing collisions create new ions and electrons. Due to the electric field, ions are accelerated toward the cathode and release new electrons by ion-induced secondary electron emission. The electrons give rise to new ionization collisions, creating new electrons and ions. A continuous current will flow through the discharge due to the constant potential difference between the cathode and anode, giving rise to a *direct current (d.c.) glow discharge*. The electrodes play an indispensable role in sustaining the plasma by secondary electron emission in d.c. glow discharges. When a time-varying potential difference is applied, as in capacitively coupled radio-frequency (RF) discharge (figure 1.1), the role of electrodes becomes less important, because the electrons can oscillate in the plasma between the two electrodes, by the time-varying electric field. When one or both of the electrodes are non-conductive, the electrodes will be charged up due to the accumulation of positive or negative charges, and the glow discharge will extinguish. By applying an alternating voltage between the electrodes, this problem can be overcome. As a result,

each electrode will act alternately as the cathode and anode, and the charge accumulated during one half-cycle will be partially neutralized by the opposite charge accumulated during the next half-cycle. A good detailed description is given in the literature [2].

In last couple of decades, the use of capacitively coupled radio-frequency (RF) discharges for dry etching and deposition of thin film layers on substrates has become common [6, 8]. Their uses include generating the plasmas for many Plasma Enhanced Chemical Vapor Deposition (PECVD) systems [9], for plasma etching systems [10], for RF sputtering systems [11], and for Plasma Immersion Ion Implantation (P3I) [12]. The other important application areas of CCPs are microelectronics etching, fabrication of thin film solar cells and thin film etching and deposition in flat panel display industries. CCPs are also important in plasma-based hardening of materials in the aerospace, automotive and steel industries. Surface hardening incorporates techniques like nitriding, carburizing and boriding [4]. Hardening the surface layer without affecting the bulk properties of the material is the objective of these techniques. Although CCPs are commonly used, there are several open technical and scientific questions. Manufacturers of plasma processing equipment have struggled with how to independently control the flux and energy of ions striking a substrate exposed to the plasma (Dual Frequency CCP). Another major scientific question is to understand how exactly electrons are heated in low pressure CCP discharges. Here in this work we will discuss a theoretical model of the heating mechanism of electrons in low pressure single frequency CCP discharges. This is reviewed briefly in section (1.4).

Recently, it is reported that the power deposition in CCPs discharges can be enhanced by replacing sinusoidal waveforms with non-sinusoidal waveforms *e.g.* Gaussian shaped voltage pulses [13]. In this work the authors used a particle-

in-cell (PIC) simulation and showed that the electron heating can be directly controlled by changing the Gaussian pulse width. Lafleur and Booth [14] used non-sinusoidal voltage waveforms, *e.g.* positive Gaussian type pulses, in their PIC simulation to control the ion flux and ion energy in CCP discharges. Later Lafleur *et al.* [15] used pulse-type tailored waveforms in argon plasma experiments in a geometrically symmetric CCP discharges and confirmed a number of predictions made by PIC simulations of a similar system [13].

The realization of the importance of sheath physics to scrape-off layer(SOL) and divertor modelling is growing in fusion devices [16–20]. It has been shown in experimental and theoretical work that the creation of RF-enhanced sheaths in the ion cyclotron range of frequency (ICRF)-heated tokamaks are responsible for much of the ICRF-edge interaction observed in tokamaks, including ICRF-specific impurity generation by the near [21] and far [19, 20] field of antenna, parallel current generation [18] and edge convection [22]. The effect of sheaths on instabilites [23] and turbulence [24] in fusion devices is also important. The plasma sheath near a conducting wall is modelled as a vacuum gap whose width is given by the Child-Langmuir law [25].

1.1 Capacitive Radio-Frequency Discharges

Plasmas are produced by supplying energy to matter until a significant fractional ionization is obtained. In an ordinary gas, each atom contains an equal number of positive and negative charges; the positive charges in the nucleus are surrounded by an equal number of negatively charged electrons so atom is electrically "neutral". A gas transforms to a plasma when the addition of heat or other energies either in electric or electromagnetic form causes a significant number of atoms to release some or all of their electrons. The remaining parts of those atoms are left with a positive charge, and the detached electrons and

ions are free to move about. Those atoms and the resulting electrically charged gas are said to be "ionized". When enough atoms are ionized then electrons and ions (normally in a quasi neutral state) exhibit collective behaviour, this state is called plasma. Typically those RF frequencies which lie between the ion oscillation frequency (ω_{pi}) and electron plasma frequency (ω_{pe}), are used in laboratory and industrial plasmas. Here, $\omega_{pe} = (n_0 e^2/\varepsilon_0 m_e)^{1/2}$ is the *electron plasma frequency*, the fundamental characteristic frequency of a plasma and $\omega_{pi} = (n_0 e^2/\varepsilon_0 m_i)^{1/2}$ is the ion plasma frequency. The industrial, scientific and medical (ISM) radio bands are reserved internationally for the use of RF energy for industrial, scientific and medical purposes other than communication. These ISM radio bands are defined by the International Telecommunication Union-Radiocommunication (ITU-R).

For pure argon plasmas at given density 10^{16} m^{-3}, the ion and electron frequencies are $f_{pi} = 3.3$ MHz and $f_{pe} = 900$ MHz respectively. The most commonly used frequency in CCP system is 13.56 MHz, the centre frequency of the second ISM band[1]. One of two electrodes is connected to the power supply (simplest one is plane parallel geometry), and the other one is grounded as shown in figure 1.1. The configuration in figure 1.1 is similar (in principle) to a capacitor in an electric circuit and also similar to the way of input power coupling into the discharge (*i.e.* by means of two electrodes and their sheaths forming a kind of capacitor), called as capacitively coupled plasma. Several books exist containing reviews of capacitive discharges, in particular the books by Y. Raizer [26], M. A. Lieberman and A. J. Lichtenberg [6] and P. Chabert and N. Braithwaite [27] are worthy of note. Such type of discharges are driven by a RF voltage/current source applied to the electrodes through a matching unit. The electrons and ions show different behaviour because of different masses.

[1]The first four ISM bands are: 6.780 $MHz \pm 0.015$ MHz, 13.560 $MHz \pm 0.007$ MHz, 27.120 $MHz \pm 0.163$ MHz and 40.68 $MHz \pm 0.02$ MHz.

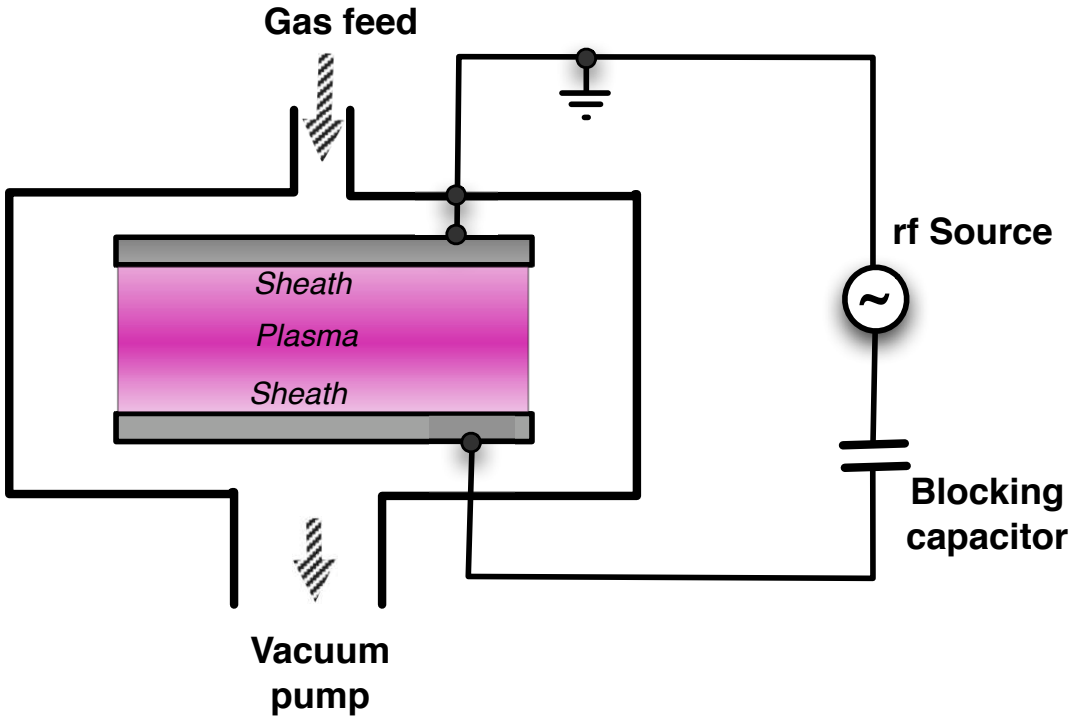

Figure 1.1: *Schematic diagram of a single frequency capacitive RF discharge.*

The light electrons can follow the instantaneous electric fields produced by the applied RF source. The heavy ions, on the other hand, can only follow the time-averaged electric field. The most commonly used gases to generate a plasma are noble gases such as argon or helium but other gases can also be used in various applications. The separation between electrodes is $l \sim 2-10$ cm and the typical voltage applied varies from a few hundred to thousands of volts. The pressure inside the chamber varies from a few mTorr to few Torr. In radio-frequency discharges operated at low pressure (few mTorr) the collision frequency is small compared to the field frequency ($\nu_m \ll \omega_{rf}$) and the electrons have rare collisions during the RF cycle. As a result, the mean free path of electrons (λ_e) may be comparable or even larger than the characteristic size of system length. The charged particle densities are on the order of $10^{14}-10^{17}$ m^{-3} in CCP discharges.

The typical temperature of the electrons ranges from $1-4$ eV and is much higher than that of ions which are nearly at room temperature, so because of the large difference in mass ($m_e \ll m_i$) electrons are not in thermal equilibrium with ions. In CCPs the potential drop across the sheath region, Φ_{sh}, is of the order of hundreds to thousands of volts and is much larger than the electron temperature T_e, which is of the order of a few volts ($\Phi_{sh} \gg T_e$). The wall is charged negatively all the time in the limit $\Phi_{sh} \gg T_e$. Electrons are pushed away from the electrode by negative charge up to a distance where a positive ion density screens its electric field. The sheath width is also significantly larger than the Debye length for the limit $\Phi_{sh} \gg T_e$, and the plasma sheath boundary can be considered as infinitely thin. The position of the boundary can be determined by the condition that the place where electrons are absent and external electric field is screened in the sheath region [28–31]. Electrons hardly lose any energy during elastic collisions. This is because for elastic collisions the energy transfer is proportional to the mass ratio of the colliding species. On the other hand heavy ions efficiently exchange energy by collisions with background gas. The highly mobile plasma electrons respond to the instantaneous electric fields produced by RF driven current and oscillate back and forth within the positive space charge cloud of ions. Due to the heavy mass, ions respond only to the time-averaged electric field. Most commonly used frequencies in industrial applications are, typically low frequencies $f_{rf} = 2$ or 13.56 MHz and high frequencies $f_{rf} = 27.12, 60$ or 160 MHz.

1.2 RF Sheath - Highly Nonlinear Region

The Debye sheath can be defined as the transition from a plasma to a solid surface [6]. In a typical discharge, plasma electrons have much smaller mass and higher temperature compared with massive positive ions. To explore this idea,

let us consider a quasi-neutral plasma in contact with a grounded conductor. In this situation more electrons than ions will initially be absorbed by the electrode because electrons have much larger thermal velocity ($\bar{v}_e = [8k_BT_e/(\pi m_e)]^{1/2}$) than the ions ($\bar{v}_i = [8k_BT_i/(\pi m_i)]^{1/2}$). Consequently, whenever a plasma is in contact with an absorbing surface like an electrode, the surface is charged negatively due to the imbalance of fluxes, and a positive potential difference appears between the plasma and the surface. In this situation, the bulk of the plasma is quasi-neutral and a net charge ($n_i >> n_e$) is found only in a narrow region adjacent to the electrode. This region is known as the sheath. The electric field inside the sheath points towards the electrode. Thus the force $-eE$ acting on electrons is directed into the bulk plasma; which reflects electrons moving towards the electrode back into the bulk plasma. On the other hand, ions from plasma that enter the sheath are accelerated and hit the electrode. The potential difference which appears between the plasma and the surface confines electrons and accelerates ions, such that the fluxes of positively and negatively charged particles absorbing at the surface become identical. The width of the sheath is the order of few electron Debye lengths, $\lambda_D^2 = \varepsilon_0 k_B T_e/n_0 e^2$, where T_e is the electron temperature in Kelvin, ε_0 is the permittivity of free space, e is the electronic charge, and n_0 is the plasma density.

The most widely used low pressure discharges are sustained by RF voltages and currents applied directly to an electrode submerged in the plasma. A neutral gas having density n_g is present between the plates. When an RF voltage or current is driven through electrode, that creates more complicated dynamics. The quasi neutrality breaks down within the oscillating sheath near the electrodes, where $n_e < n_i$ and plasma is quasi neutral *i.e.* $n_e \approx n_i$ almost everywhere except in the sheath region. The sheath dynamics is strongly nonlinear so to describe this basic phenomenon a very simple qualitative model

based on one used by Godyak and Popov in 1970s now widely known as the *homogeneous model* [29, 32, 33] will be used. Let us start by considering a semi-infinite plasma in contact with a planar electrode and which is driven by a sinusoidal RF current $I_{rf}(t)$, *i.e.* $I_{rf}(t) = \tilde{I}_{rf}\, sin\,(\omega t)$. The plates are separated by distance $\boldsymbol{l}$ and each has cross sectional area $\mathbf{A}$. For simplicity we assume that ion density $\mathbf{n}$ is uniform and constant in time everywhere, whereas the electron density is equal to the ion density except for the sheath regions near the electrode where it is zero. Considering $x_{sh}(t)$ be the instantaneous position of the highly oscillating electron sheath edge and using Gauss's law, the electric field is found to be

$$E(x,t) = \begin{cases} \frac{en}{\varepsilon_0}(x - x_{sh}(t)), & \text{for } x \geq x_{sh}(t) \\ 0, & \text{otherwise.} \end{cases} \tag{1.1}$$

The current that flows through the sheaths is almost entirely displacement current. This is true because in bulk plasma the conduction current is carried mainly by electrons, and inside time-varying sheath the electron density is negligible. This analysis also assumes that ions respond only to the time-averaged potentials *i.e.* $\omega_{pi}^2 << \omega_{rf}^2$, here ω_{pi} is ion plasma frequency, the ions carry no RF current. So the conduction current carried by the steady flow of ions across the sheath to the plates is much smaller than the displacement current. In real applications the sheath dynamics is much more complicated and the description here is only the tip of the iceberg. Ions are accelerated by the sheath electric field and these ions strike the electrode and due to ion flux conservation the density drops down. Bulk plasma also oscillates when the instantaneous electron sheath edge oscillates and there is a transition region between the sheath and bulk which is not entirely field free. All these effects makes the sheath dynamics more complex. There are other better analytical models that includes these effects like Lieberman's analytic model [30], Kaganovich's two-step ion

density model [34] etc.

1.3 The presheath and the Bohm criterion

So far we have assumed that the space charge region of the sheath terminated at the plane where the electron and ion densities became equal (undisturbed plasma). In reality there is a quasi-neutral transition region of finite electric field between these two regions. This region is typically much wider than the sheath and is called *presheath*. The effect of this region is to increase the velocity of ions so at the sheath presheath interface there is a transition from subsonic ($u_i < u_B$) to supersonic ($u_i > u_B$) ion flow, where the condition of charge neutrality must break down (the electron density drops faster than the ion density in the sheath region). The existence of this velocity change was demonstrated by Bohm [35] and the resulting criterion for sheath formation is known as *Bohm sheath criterion*. The transition can arise from geometric contraction of the plasma, from ion friction forces (collisions) in the presheath, or from ionization in the bulk plasma [36].

In single ion species case, the Bohm criterion gives

$$\langle u_s \rangle \geq u_B = \left(\frac{k_B T_e}{m_i} \right)^{1/2}, \tag{1.2}$$

where u_B is called **Bohm velocity**, u_s is the average velocity of the ions at sheath edge, k_B is the Boltzmann's constant, m_i is the ion mass and T_e is the electron temperature in Kelvin. This says that the ion velocity on entering the sheath must be greater than $(k_B T_e/m_i)^{1/2}$, *i.e.* it is determined by the electron temperature. Chen demonstrated that the physical significance of the criterion is that the acceleration of ions in the sheath and repulsion of electrons there, both of which decreases the relevant particle volume densities, must be such that the ion density decrease less rapidly than the electron density across the

sheath [37].

Riemann showed that in case of two or more ion species, the Bohm criterion is written as

$$\Sigma \frac{q_k^2 n_k}{m_k \langle u_k \rangle^2} \leq \frac{e^2 n_e}{k_B T_e}, \tag{1.3}$$

where **e** is the absolute electron charge, n_e is the electron density at the sheath edge and q_k, n_k, $\langle u_k \rangle$ denote the charge, density and average velocity at the sheath edge of the k^{th} ion species [38]. Equation (1.3) has no unique solution for the average ion velocities. Whether one can obtain special solutions depending on the plasma parameters, and what additional information is required to do so, remains an open question.

1.4 Heating Mechanisms in CCPs

Low pressure discharges are sustained by RF currents and voltages applied directly to an electrode immersed in the plasma. Due to this a high voltage capacitive sheath appears between the electrode and the bulk plasma. The applied RF current at electrode flowing across the sheath and electrons carry the currents to the bulk plasma. The electrons are energetic enough to ionize the neutral gas and maintain the ion population. So it is very important to know the mechanism by which electrons can gain energy. The different types of heating mechanisms are briefly described here:

(1) Ohmic or collisional heating occurs mainly in bulk plasma due to collisional momentum transfer between the oscillating electrons and the neutrals. The averaged power per unit volume absorbed by the plasma P_{ohm} is

$$P_{ohm} = \frac{1}{2} \tilde{J}^2 \, Re(\sigma_p^{-1}), \tag{1.4}$$

where $\tilde{J}$ is the current density, $\sigma_p = \varepsilon_0\,\omega_{pe}^2/(j\omega+\nu_m)$ is the plasma conductivity, ω is the applied frequency and ν_m is the electron neutral collision frequency for momentum transfer. Equation (1.4) can be applied to find ohmic power absorption from waves as well as from oscillating fields. This mechanism is well understood and fully described in the literature [6].

(2) For low pressure discharges (where the electron mean free path λ_e is larger than the inter electrode separation l), the ohmic power is not the main source of power absorption by the plasma electrons. Another possible heating mechanism, in which electrons interact with the high voltage oscillating sheaths, and a net momentum transfer occur due to this interaction. This heating mechanism is called collisionless or stochastic heating. Landau [39] was the first to suggest that non-ohmic electron heating could occur in the presence of an oscillatory current crossing a plasma boundary. Stochastic heating in low pressure capacitive discharges has been studied by different models [30, 34, 40–43] as well as in experiments [44]. High frequency voltage or current driven sheath structure was studied in detailed by Schneider [45]. Here 'high frequency' means, frequency less than the electron plasma frequency, $\omega_{pe}^2 = n_0e^2/\varepsilon_0 m_e$, but larger than the ion plasma frequency, $\omega_{pi}^2 = n_0e^2/\varepsilon_0 m_i$. The sheath expands with increasing applied voltage and electrons are pushed away from the electrode. Subsequently, the sheath collapses as the voltage decreases, and when the sheath voltage is minimum an electron current flows to the electrode. The place where the sheath reaches its maximum extent is also the point where the ions reach their Bohm speed, and this is known as the ion sheath edge or the Bohm point (Figure (1.2)). The instantaneous sheath edge is known as electron sheath edge. These qualitative features of the high frequency sheath were established later by few other authors [30, 32, 46, 47]. In the

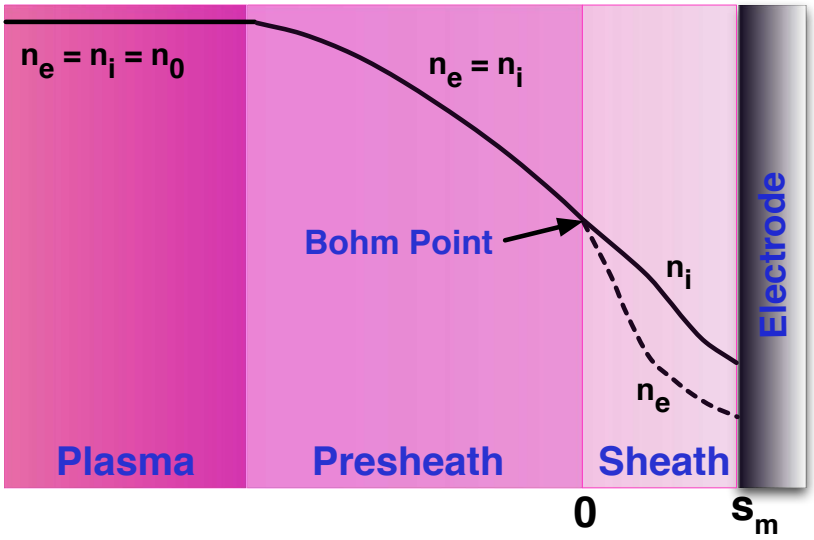

Figure 1.2: *Schematic diagram of a bulk plasma, presheath and sheath region in contact with electrode.*

present context, the most important of these later works is by Lieberman [30]. Lieberman derived an extraordinary analytic self-consistent solution of the sheath equations. The biggest advantage of this solution is that it gives a closed analytic formula for all the important parameters associated with the sheath. This solution is known to be reasonably accurate and the sheath quantities are expressed as functions of a single parameter, **H**, where

$$H = \frac{\tilde{J}_0^2}{\pi e \varepsilon_0 T_e \omega_{rf}^2 n_0} = \frac{\tilde{s}_0^2}{\pi \lambda_D^2} \,, \tag{1.5}$$

where $\tilde{J}_0$ is the oscillating current density amplitude, ω_{rf} is the angular frequency at which the sheath is driven, T_e is electron temperature, n_0 is the plasma density at the ion sheath edge, $\tilde{s}_0$ (*i.e.* $\sqrt{\tilde{J}_0^2/e^2\omega_{rf}^2 n_0^2}$) is the amplitude of oscillation of electrons at the ion sheath edge, and the Debye length, λ_D (*i.e.* $\sqrt{\varepsilon_0 T_e / e n_0}$), is evaluated at the ion sheath edge.

Theoretical interest in collisionless heating by high frequency sheaths be-

gan in the nineteen-fifties. Godyak [28, 29, 32] turned to this topic in the nineteen-seventies. He introduced a classical "hard wall" model. According to this model, the electron sheath edge is treated as a moving rigid barrier or "hard wall". Electrons move through bulk plasma towards sheath, where they 'collide' (collisions are elastic, 'Hard Wall' approximation) with the sheath electric field and bounce back. An electron that is reflected from a moving sheath experiences a change of energy. If the sheath moves toward the electron, then the energy increases; if the sheath moves away, then the energy decreases. For an oscillating sheath, some electrons gain energy and others lose energy. However, averaging over an oscillating period (because head-on collisions are most frequent), the net effect is an energy gain, corresponding to a dissipation in the sheath. This mechanism also has been called "Fermi acceleration" [40, 48] or "wave riding" [49]. The change of velocity of a single electron incident on the sheath with velocity v can be written as

$$v_r = -v + 2u_{sh} \,, \tag{1.6}$$

where v_r is the velocity of the electron after reflection and u_{sh} is the velocity of plasma sheath boundary. Godyak assumed in his model that the electron flux incident on the sheath is assumed to have a non-drifting velocity distribution function $f(v)$. The instantaneous power per unit area transferred between the electrons and the sheath edge moving at velocity, u_{sh}, is

$$S_{stoc} = \int_0^\infty \frac{m_e}{2}(v_r^2 - v^2)(v - u_{sh}) f(v)\, dv \,, \tag{1.7}$$

$$= -2m_e \int_0^\infty u_{sh}(v - u_{sh})^2 f(v)\, dv \,. \tag{1.8}$$

Here $\int_0^\infty f(v)\, dv = n$ and it is assumed that $f(v)$ can be approximated by a Maxwellian with temperature T_e and that the plasma density $\mathbf{n}$ is

uniform. Again $u_{sh} << \bar{v}_e$, where $\bar{v}_e = [8k_BT_e/(\pi m_e)]^{1/2}$ is the mean electron thermal velocity, so that the lower limit of integration can be set to zero. So an integration over velocity and an average over time can be carried out to obtain an average power per unit area for one sheath

$$\bar{S}_{stoc} = \frac{1}{2} m_e \bar{v}_e n u_0^2 \,, \tag{1.9}$$

where u_0 is the amplitude of sheath oscillation (*i.e.* u_{sh}) at some time **'t'**.

Later Lieberman [30] used a different form for the velocity distribution in equation (1.7) to take into account two important effects neglected by Godyak: that the electron densities at the ion sheath edge and the electron sheath edge are different, and that the electron drift velocity is not zero. Lieberman assumed

$$f_{sh}(v) = \frac{n_{sh}}{n_0} f_0(v - u_0) \,, \tag{1.10}$$

where quantities with subscript **0** are defined at the ion sheath edge, and quantities with subscript ***sh*** are defined at the electron sheath edge. Insert this expression into equation (1.7), and with the approximation that $\bar{v}_e >> u_{sh}$, one obtains the averaged power

$$\bar{S}_{stocL} = \frac{3\pi}{32} H m_e \bar{v}_e n_0 u_0^2 \,. \tag{1.11}$$

Here $u_0 = \tilde{J}_0/(en_0)$ is the amplitude of the bulk electron oscillation velocity and **H** is given by equation (1.5).

It is noticeable that there are inevitable problems with these models, and with any similar approach based on a "hard wall" model. In any "hard wall" model which has continuous current at the electron sheath edge, the instantaneous heating power given by equation (1.7) will vanish identically, within the framework of assumptions as discussed above. This

is compelling demonstration that the "hard wall" stochastic heating model is insufficient. Because of the difficulty of obtaining current-conserving results with hard wall calculations, Gozadinos *et al.* [43] developed an alternative treatment using fluid equations. They checked their analytic result against a specialized PIC calculation in which the ions were held fixed, obtained good agreement. Kinetic effects that distort the electron velocity distribution from Maxwellian have been examined by Kaganovich [34] by employing a two-step ion density model. He showed that a hard wall model can be used to calculate $\bar{S}_{stoc}$, provided the bulk motion is taken into account.

Apart from the analytic studies, the literature contains many investigations of electron heating by oscillating sheaths using different kinds of computer simulation that do not include self-consistent electric fields [50–54]. Generally, in the absence of self-consistent fields, current will not be conserved, and one cannot expect quantitatively correct results in such cases.

(3) "Pressure heating" is the another mechanism by which stochastic heating can be explained. Stochastic heating should be associated with the time varying fields between the electron and ion sheath edges. Here a pressure heating effect is connected with the cyclic compression and rarefaction of electrons as they flow in and out of the sheath regions during sheath oscillation. Surendra and Graves [55] initially showed the importance of acoustic effects in high frequency discharges. They explained the reason of the regions of net negative electron heating that occur in the quasi-neutral plasma bulk of some high frequency discharges are produced by electron acoustic wave propagation from the sheath regions, but they did not discuss about the electron heating inside the sheaths. In a later work,

Surendra and Dalvie [56] made the suggestive observation that electron heating observed in the oscillating sheath of a particle-in-cell simulation could be identified with the pressure-work term in a suitable set of moment equations. However, they did not proceed to develop this idea. Turner and co-workers [42, 57] further developed this idea and showed that in a model periodic system, there existed a collisionless heating mechanism comparable in efficacy with the collisionless heating seen in the oscillating sheaths of bounded plasmas. This is so called pressure heating mechanism which depends only on the existence of density gradients, and does not require the presence of a sheath edge. So the pressure effect in question is caused by the difference in plasma density and temperature between the bulk plasma and the sheath region. When a sheath expands, electrons flow into the adjacent bulk plasma and are compressed. At the same time, electrons are rarefied as they flow into the opposite collapsing sheath. Since the thermal conductivity of the bulk plasma is finite, these simultaneous rarefaction and compression effects produce nonequilibrium thermal disturbances and the net work being done is not necessarily zero. However, the analytical model developed by Turner was not extended to the case of a real oscillating sheath with a moving boundary, and consequently the possibility that additional heating mechanisms are present in that case was not excluded. Moreover, Turner's model did not lead to a convenient expression for the amount of heating to be expected in situations of practical interest.

(4) Another suggested heating mechanism is associated with the observed oscillations in the electron density near sheath edge. These oscillations are near electron plasma frequency *i.e.* ω_{pe} and generate due to quasi-neutrality failure at sheath edge. It is not yet fully clear how these oscil-

lations are excited, but it is certainly possible for the oscillation energy to be transferred to electron thermal energy by the well known mechanism of Landau damping [39] or a related process. Such type of oscillations can be seen clearly in simulations but no relevant theory has yet been put forwarded [58, 59]. However, at more moderate values of H, amplitude of such oscillations are very weak, so it cannot be the case that this is in general the main heating mechanism. Moreover, there is no evidence at present that even under extreme conditions these oscillations constitute an important heating mechanism. We will discuss all these issues in the next chapters.

(5) The wave phenomenon discussed above is different from "*series resonance*". Two dominant natural resonances occur in metal bound plasmas. One is the plasma oscillation (due to symmetric motion of bulk plasma) at the electron plasma frequency ω_{pe}, generates no net current in an external short circuit of planar two electrode system. The second one is because of antisymmetric motion of the electrons and is at lower frequency which generates an oscillatory current in an external short circuit. In capacitively coupled RF discharges this particular resonance arises because of periodic exchange between the electric field energy in the plasma sheath and the kinetic electron energy in the plasma bulk. Here a lossy inductance (the bulk plasma) and one or two capacitors (the sheaths) are analogous to a series circuit and phenomena is known as "*electron series resonance*", "*plasma series resonance*" or "*plasma-sheath resonance*". Electron inertia is the main cause of the effective inductance of the bulk plasma and the ohmic resistance due to electron-neutral collisions leads to power dissipation. The capacitive characteristic of a sheath is provided by space charge. The voltage charge relation is highly nonlinear in the sheath

which shows different behaviour from a normal capacitor [60–66]. The relation between the potential drop across the sheath and the displacement current is nonlinear because of ion and electron dynamics in the sheath. Our main interest is in nonlinearity because it induces harmonics in the electric fields and currents in the discharge. Most of the RF discharges carried out for the specific case of symmetrical RF discharges [41, 67, 68]. Only odd harmonics in the current (or in RF voltage for current driven discharges) are generated because of the symmetry of the discharge and the nonlinearity of the whole system is very weak [69, 70]. Because of these circumstances, a sinusoidal current is assumed which results in the simplification of modelling [30, 71–74] and experiment [73–75] for the frequency range significantly above the ion plasma frequency ω_{pi}. Strong nonlinearity has been observed for both symmetrical and asymmetrical RF discharges, nearby and lower than ω_{pi} [76–78].

Typically, the series resonance frequency $\omega_{sr} << \omega_{pe}$. The *Series resonance* phenomenon is detailed described by Tonk [79, 80], Dattner [81], Parker *et al.*[82], Taillet [83], Schneider and Angew [45] and Godyak [29]. The *series resonance* frequency ω_{sr} is the natural frequency and is given by

$$\omega_{sr} = \omega_{pe}\sqrt{\frac{2\bar{s}}{L}}\,, \tag{1.12}$$

where $2\bar{s}$ ($\bar{s} << L$)is the combined time average width of the left and right sheaths and 'L' is the typical bulk extension. This expression is applicable only when the electron collision frequency is low enough that the resistance of the plasma bulk is negligible. The *series resonance* effect induces high frequency oscillations (order of 100 MHz) which superimposes on the normal RF current and amplitude of these oscillations is restricted by collisions of the oscillating bulk electrons with the background neutral

gas. Because of these oscillations the sheath expansion is faster as compared with regimes where sinusoidal RF current waveforms are observed [60, 84–86].

Series resonance effects enhance both the stochastic and ohmic heating. It is shown in literature that at low pressures the *series resonance* effect increases the heating by nearly a factor of two, both with and without stochastic heating. Ohmic heating which is proportional to collisional frequency, goes to zero linearly as the pressure goes to zero, with or without nonlinear series resonance excitation. By considering stochastic heating, which is independent of pressure, there is still a significant enhancement in the heating because of the nonlinear series resonance excitation [63]. The enhancement of the ohmic heating has been also investigated by a model in literature and also shown that this enhancement is due to the *series resonance* [60–62, 87].

However, there is no complete model formulated yet to exemplify the exact mechanism and furnish predictions analogous to simulations or experiments.

1.5 Modelling Tactics

The act of simulating or modelling something generally entails representing certain key characteristics or behaviours of a selected physical or abstract system. Computer simulations have become a useful part of mathematical modelling of many natural systems in plasma physics (computational physics), astrophysics, chemistry and biology, human systems in economics, psychology, social science, and engineering. Simulations are used to explore and gain new insights into new technology, and to estimate the performance of systems too complex for analytical solutions. Even though experiments supply the basis for the percep-

tion of the proficient range of phenomena occurring in plasma, still that is not always sufficient. Sheaths are very complex in nature and experimental measurements in this region is desperately hellacious task. So modelling is a very good substitute in this case.

Modelling is also advantageous because it can create situations which are hellacious or undo-able experimentally but can be used to test theoretical models. Plasma can be modelled by several different techniques and each has its own distinction and deficiency. Following is the useful classification:

- *Equivalent Circuit models*: In such models the different parts of discharges represent simple electrical circuits. The sheath, for instance, is sometimes represent as a resistor, a capacitor and a diode in parallel. The values of the components can be either estimated theoretically or measured experimentally, and useful properties of the discharge, for example the energy of ions at the electrode, can be easily estimated. Obviously, the disadvantage of this approach is that it is somewhat crude, and one could not expect such models to provide perception into complex phenomena.

- *Fluid models*: The fluid model describes the plasma based on macroscopic quantities (velocity moments of the distribution function such as density, mean velocity, and mean energy). The equations for macroscopic quantities, called fluid equations, are obtained by taking velocity moments of the Boltzmann equation or the Vlasov equation. Usually, only the first three moments are used describing particle, momentum and energy conservation. A closure assumption is needed because for each moment equation added to the system a new unknown is introduced. The fluid equations are not closed without the determination of transport coefficients such as mobility, diffusion coefficient, averaged collision frequencies, and so on. To determine the transport coefficients, the velocity distribution function

must be assumed/chosen. But this assumption can lead to a failure of capturing some physics. The necessity of a closure assumption and the occasional restriction on the form of the distribution function are some of the disadvantages of these models. The fluid approach, although it is not so accurate compared to kinetic methods, due to the shorter computational times, one can easily go for higher dimensionality ($2D$, $3D$).

- *Kinetic models*: Kinetic models are time and space dependent solutions of the Boltzmann equation which produces electron and ion velocity distributions either by direct integration of the equation or by applying statistical techniques (Particle in Cell - Monte Carlo method) therefore do not need to assume a Maxwell-Boltzmann distribution. A kinetic description is often necessary for collisionless plasmas. There are two common approaches to kinetic description of a plasma. First one is Monte Carlo simulations, in which the fields are assumed to be known a *priori* and the equations of motion for the particles under the influence of these fields are solved. Another one is Particle-In-Cell (PIC) technique [88, 89] which gives self-consistent solution of the Boltzmann equation by simultaneously solving the particle equations together with the fields. The kinetic approach although it is computationally intensive, is the least dependent on a-priori assumptions leading to more accurate results. Finally, direct solvers of the Boltzmann equation also exist [90]

1.6 Research objectives and outline

The general outline of this thesis is as follows: *chapter 2* describes the particle-in-cell (PIC) simulation technique which is used here in entire research work. A semi-infinite plasma in contact with an electrode is modelled with the help

of PIC method. The particles are injected from the boundary. Plasma can be assumed either collisionless or collisional (using charge-exchange collisions for the ions and elastic scattering for the electrons) and ionization processes are ignored here. Scaling of physical quantities and boundary conditions are also described here. To test the theoretical models and their assumptions, only the area near the sheath/presheath regions is modelled here. Better diagnostic resolution is also achieved.

In *chapter 3*, the theory of stochastic heating through Fermi acceleration mechanism is fully examined. Application of "Hard Wall Model" in capacitive *RF* discharges is also described. This is done through self-consistent PIC simulations. The power deposition calculated by self-consistent PIC simulation is compared with the one predicted by Lieberman's model [30] and Kaganovich *et al.* [34] model in case of single frequency capacitive *RF* discharges. The presence of strong field reversal phenomena at the time of sheath expansion and the reflection of ions from the near sheath edge is observed in extreme cases. The average power per unit area scaling with frequency is also explored in this chapter.

In *chapter 4*, the evidence of the electron plasma wave propagation from sheath edge towards bulk plasma is discussed. These waves are damped during their propagation and it occurs due to Landau damping or some related process, so concept of Landau damping is discussed here. This wave phenomena is discussed with the help of PIC simulations of half-infinite plasma. The spatiotemporal profile of electron density shows that the wave starts near sheath edge and propagates in bulk plasma and finally disappears. The modification of the sheath structure is also observed. The spatiotemporal profile of electric field shows the presence of a strong field reversal region near the modified sheath region at the time of sheath expansion. Electron trapping is also observed near

to the field reversal region. The frequency of these waves are calculated to be of the order of electron plasma frequency, ω_{pe}. The effect of electron elastic collisions on electron plasma waves is also investigated.

In *chapter 5*, the analytical model of stochastic heating for dual-frequency CCPs (developed by Kawamura *et al.* [1]) is discussed. The power deposition calculated by self-consistent PIC simulation in case of dual-frequency CCPs is compared with the power estimated by the dual-frequency stochastic heating analytical model developed by Kawamura *et al.* [1]. The strong wave phenomena during the expansion and collapsing phase of low frequency sheath in dual-frequency CCP case are being observed in simulation. The presence of strong field reversal and electron trapping phenomena near to the field reversal region is also discussed. The signature of reflection of ions is observed in simulation. The frequency of these waves are calculated to be of the order of electron plasma frequency *i.e.* ω_{pe}.

Finally, in *chapter 6* we conclude that the stochastic heating predicted by the existing single frequency analytical models given by Kaganovich *et al.* [91] and dual frequency analytical model given by Kawamura *et al.* [1] are satisfactory. However in extreme cases, new physical effects appear and the simulation results deviate from analytical models. The wave phenomenon in case of single and dual frequency cases are also concluded in this chapter. Future scope of this research work is briefly discussed here.

CHAPTER 2

Semi-Infinite Particle-In-Cell Simulation Technique

2.1 Introduction

A plasma is a hot, fully ionized gas which may be regarded as a collection of positive ions and negative electrons interacting through their mutual electric and magnetic fields. Interaction between the charges and the internal fields (produced by the charges themselves) and the externally applied fields govern the dynamic behaviour of plasma. Charge and current densities (ρ and J) are related to fields by Maxwell's equations. Interaction of electromagnetic fields with charged particles is determined by the *Lorentz force*. For the system of **N** particles, the requirement is to solve **N** nonlinear coupled differential equations of motion simultaneously. Since the fields and the particle trajectories are intrinsically coupled, a self-consistent method must be used. The presence and motion of charged particles are associated with the internal fields and the internal fields also influence charged particle motions, which, in turn, modify the

internal fields. Although this self-consistent approach is conceivable in principle, at macroscopic level, Maxwell's equations along with Boltzmann's equation provide a self-consistent nonlinear system that is very difficult to analyze without the use of simplifying assumptions. On the other hand at microscopic level, a plasma can be treated as an N-body problem and further analysis is not possible.

With the advent of large and fast computers, an alternative approach for study of the plasma is through numerical and semi-numerical models. There are several types of plasma models like fluid models [6, 37, 92], equivalent-circuit models [6], kinetic models [88, 89, 93], hybrid kinetic/fluid models [88, 89, 94] and models solving the Boltzmann equation directly [6, 90, 92]. Each model has its own advantages and disadvantages. Now-a-days the Particle-In-Cell (PIC) simulation is one of the most popular kinetic schemes. PIC methods have been in use since 1955 [95], even before the first Fortran compilers were available. PIC is an indirect approach to solve the Vlasov or Boltzmann equations based on integrating the equation of motion of a set of particles. The method gained popularity for plasma simulation in the late 1950s and early 1960s when it was fully proposed by Dawson [96] (at Princeton) and Oscar Buneman [97–100] (at Cambridge) and later developed by Birdsall and Langdon [101–103] at Berkeley. A detailed description with historical background can be found here [88, 89, 101–103]. The particle-in-cell simulation technique follows the motion of individual particles in self-consistent electromagnetic fields and provides a self-consistent solution of the fields and particle dynamics from first principles, without any additional assumptions. There are a few disadvantages, *e.g.* limitations on the number of particles gives rise to numerical thermal fluctuation and PIC simulations are relatively computationally expensive. However now-a-days, the continuous development of new faster microprocessors makes it possible to run

PIC codes on even low cost desktop computers at home.

A PIC simulation has two important aspects: first, it provides insight into areas where the theory is not complete or incorrect. When the assumption of the theory can not be verified experimentally this is a most useful technique. Secondly, one can consider PIC simulations as an extension of experiments, either providing results that are unobtainable experimentally, or to compare directly to experiments, enabling us to clarify the underlying mechanisms involved in some experimental measurement. The second use is currently quite limited because of the complexities rolling out from plasma chemistry and surface processes.

It is often desirable to model plasma dynamics in the vicinity of an electrode, independent of the bulk of the plasma. So the main aim of our work is to study the electron and ion behaviour inside the sheath. Analytical [30, 36, 69] or semi-analytical [104] models dealing with these problems are useful, but at the same time these models have problems with assumptions used or a lack of self-consistency. In addition, the natural presence of two separate spatial scales in this problem (the sheath scale being the electron Debye length λ_D whereas the bulk plasma/presheath scale being the ion mean free path λ_i) requires special treatment of the boundary layer and presents difficulties to analytic approaches (see discussion in [105]). To achieve this the standard PIC scheme has been modified in order to model only the sheath region and the plasma in its neighborhood [106]. Thus in this method it is assumed that to the left of the simulation region lies a half-infinite bulk plasma of given density and temperature, while to the right a perfectly absorbing electrode exists. The left boundary emits fluxes of electrons and ions corresponding to the presence of the assumed half-infinite plasma. This modification makes it possible to model the sheath with additional details compared to the traditional PIC implemen-

tation on the same computational resources. This procedure has advantages in principle and in practice. The advantages in principle are that, there is a precise control of the density, temperature and other parameters characterizing the bulk plasma, and it also ensure that these quantities remain constant in time. In other words, the assumptions of the theories discussed above are precisely satisfied. The advantages in practice are that, since we explicitly simulate only the part of the plasma that is of direct interest, we can obtain enhanced spatial, temporal and statistical resolution for a given amount of computational work, relative to the simulation of an entire plasma. The disadvantage, however, is that the nature of the problem requires that the boundary on the bulk-side of the plasma is treated independently, and there is a difficulty in doing so in a self-consistent way. If the fluxes of particles emitted from the boundary are not quite self-consistent, a potential difference appears between the boundary and the plasma - so called "source sheath"- and particles entering or leaving the plasma via the emissive boundary must traverse this source sheath. Consequently, the velocity distributions and the densities of the electrons and ions in the plasma may be distorted in comparision with the desired bulk plasma parameters. This effect may be of no importance, it may be a nuisance [107]; in the present work it is of no importance because of the improved algorithm that makes the source sheath potential small compared to the mean energies of either electrons or ions at the emissive boundary [106]. An alternative approach of modelling a semi-infinite magnetised plasma by PIC simulation is described in [108].

2.2 PIC Technique - General Implementation

All the mathematical models to which particle simulation methods are applied can be formulated as a set of charged particles interacting through self-consistent

fields. Particles have a number of constant attributes like charge (**q**) and mass (**m**), and variable attributes like position and velocity. The variable attributes evolve according to equations of motion whose driving terms are given by the field equations. So in general the motion of particles is produced by the forces or fields. The fields are calculated from *Maxwell's equations* by knowing the positions of all the particles and their velocities. The forces on the particles can then be calculated by using the *Newton-Lorentz* equation of motion by knowing the electric and magnetic field. Fields can be calculated from initial charge and current densities and these fields move the particles (small distance). Now recalculate the fields due to the particles at their new positions and velocities and this procedure is repeated for several time steps.

In this work the PIC model assumes a 1-D planar geometry. A relatively small number of particles ($10^5 - 10^6$) are needed for 1-D case. Here, each of the simulation particles is a charge sheet which can move under the influence of self-consistent electric field inside the fixed simulation region. Each of these *super-particles* represents a large number of 'real' particles typically equivalent to approximately 10^{10} real particles. The position x and two velocities, u_x in the x-direction and $u_\perp$ in the direction perpendicular to x is assigned by every super-particle. The simulation region in which the super-particles exist is divided into N_c cells resulting in a grid with $N_c + 1$ points. So the equation of motion for the i^{th} super-particle is (since only electric fields are considered here)

$$\frac{d^2x_i}{dt^2} = \frac{q}{m_i}E(x_i, t), \tag{2.1}$$

here E represents the electric field, which can be calculated from Poisson's equation

$$\frac{d^2\Phi(x,t)}{dx^2} = -\frac{\rho}{\varepsilon_0}, \tag{2.2}$$

with

$$E(x,t) = -\frac{d\Phi}{dx}\,. \tag{2.3}$$

2.2.1 Normalization of the physical quantities

Physical quantities can be described in terms of few fundamental quantities like length, mass, time, electric charge and temperature. All physical quantities have to be normalized to dimensionless variables in order to reduce the number of calculations during computation. This can be done by normalising quantities/variables with respect to the characteristic lengths of the system: the size of each spatial cell (Δx), the time integration step (Δt) and the weight of each super-particle belonging to the s^{th} type of species ($\mathcal{W}_s$). Here weighting is dependent on particle positions [88]. It is understood that the quantities Δx, Δt, $\mathcal{W}_s$ have to be chosen in such a way that there is a balance between the desired accuracy and computational cost. Normally accuracy is concerned with local errors due to roundoff errors and truncation errors. Stability is concerned with the propagation of errors. Sometimes even if truncation and roundoff errors are very small, errors grow rapidly with time. So both criteria are very important and minimal criteria for the simulation to be stable and accurate [88] are

- $\omega_{pe}\Delta t < 0.2$,
- $\frac{\Delta x}{\lambda_D} < 0.5$,

where λ_D is the electron Debye length, so that the electron plasma time and spatial scales can be properly resolved.

The physical quantities used along with their rescaled counterparts are shown in table (2.1). Other dependent parameters such as the current or the kinetic energy can be calculated from these quantities.

2.2.2 The Particle Mover

The particle mover is the most time consuming part of PIC because it has to be done for each particle separately. Thus, the pusher is required to be of high

Table 2.1: *Conversion of physical quantities to PIC variables*

Parameter	Rescaled Parameter
Position x	$\tilde{x} = \frac{x}{\Delta x}$
Time t	$\tilde{t} = \frac{t}{\Delta t}$
Velocity u	$\tilde{u} = \frac{u\Delta t}{\Delta x}$
Charge q	$\tilde{q} = \frac{q}{\lvert q_e \rvert}$
Mass m	$\tilde{m} = \frac{m}{m_e}$
Surface number density n_s	$\tilde{n_s} = \frac{n_s \Delta x}{\mathcal{W}_s}$
Surface charge density ρ	$\tilde{\rho} = \sum_s \frac{n_s \Delta x}{\mathcal{W}_s}$

accuracy and speed and due to this reason much efforts are made on optimizing the different schemes. The most popular schemes for the particle mover are *explicit* and *implicit* solvers. Explicit methods calculate the state of a system at a later time from the state of the system at the current time, while implicit methods find a solution by solving an equation involving both the current state of the system and the later one. It is clear that implicit methods require an extra effort, and they can be much harder to implement. However, many problems arising in real life are stiff and require implicit methods as against explicit methods because it requires impractically small time steps Δt to minimize the error. For other problems explicit solvers, despite the requirement of small time steps, are preferred as they are simpler and much faster than implicit solvers. The integration scheme used here is the usual *leap-frog method*, which is an explicit solver. Here a particle's position is known at time $\mathbf{t}$, whereas its velocity is known at time $t - \frac{1}{2}\Delta t$. Thus, at the next step the position and velocity can be written as

$$x^{t+1} = x^t + u^{t-\frac{1}{2}}\Delta t, \tag{2.4}$$

$$u^{t+\frac{1}{2}} = u^{t-\frac{1}{2}} + \frac{qE(x^t, t)}{m}\Delta t, \tag{2.5}$$

where $t+1$ and $t \pm \frac{1}{2}$ indicate times at $t + \Delta t$ and $t \pm \Delta t/2$. These equations can be written in the rescaled variables as follows

$$\tilde{x}^{t+1} = \tilde{x}^t + \tilde{u}^{t-\frac{1}{2}}, \tag{2.6}$$

$$\tilde{u}^{t+\frac{1}{2}} = \tilde{u}^{t-\frac{1}{2}} + \frac{\tilde{E}(\tilde{x}^t, t)}{\tilde{m}}. \tag{2.7}$$

2.2.3 Charge Density Assignment and Electric Field Evaluation

Once all particle positions and velocities have been updated and new particles have been loaded, it is essential to calculate the charge density on the discrete grid points from the continuous particle positions. With the help of charge density, fields can be calculated and finally the force at the particles from the fields on the grid points. Let us consider the i^{th} grid point of the charge grid then the amount of charge assigned to it is given by

$$\tilde{\rho} = \sum_{s,k} \tilde{q}_s Q(\tilde{x}_k - x_i), \tag{2.8}$$

where s is the summation index for the particle species, k is the summation index for the super-particles and Q is the interpolation kernel given by

$$Q(x - x_i) = \begin{cases} 1 - |x - x_i| & \text{if } |x - x_i| \leq 1 \\ 0 & \text{otherwise.} \end{cases} \tag{2.9}$$

So here the kernel described by equation (2.9) distributes the charge of every super-particle to its two nearest grid points linearly (*first-order*), smoothing the charge density. Detailed discussion of the different interpolation kernels for both lower (*zero-order* weighting) and higher (*second-order* weighting) order interpolation schemes can be found in the literature [101]. Higher order

interpolation schemes result in an increased computational cost. Lower order schemes (*zero-order*) will produce noisy density and electric field both in space and time because of the sharp transition in density as a particle passes through a cell boundary. These noisy results may not be suitable in many plasma problems. In general the kernel described by equation (2.9) gives the best tradeoff between accuracy and speed [88].

The potential and electric field can be calculated on the grids by the use of finite difference method, once the charge density is known

$$\begin{aligned} \tilde{\Phi}_{i+1} &= -\frac{\tilde{\rho}_i}{\varepsilon_0} + 2\tilde{\Phi}_i - \tilde{\Phi}_{i-1}, \\ \tilde{E}_i &= \frac{\tilde{\Phi}_{i-1} - \tilde{\Phi}_{i+1}}{2}. \end{aligned} \tag{2.10}$$

Appropriate boundary conditions must be used for equation (2.10) and these boundary conditions will be discussed in section (2.3.1).

2.2.4 Collisions

In a real plasma, many reactions play a role, ranging from elastic collisions, such as collisions between charged and neutral particles, inelastic collisions, such as electron-neutral ionization collision and also chemical reactions, each of them requiring separate treatment. It is widely known that plasma chemistry plays an important role in plasmas. However the entire complexity of these processes cannot be fully integrated into numerical codes. The main reason is that this would radically increase the number of modelled species needed and therefore computational time, and other reason because there is lack of information (for *e.g. cross-sections*) for some of the processes. So there is a compromise and most simulations include only the most fundamental processes such as elastic collisions, ionisation and excitation. In the present work, it is assumed that ionisation is not an important process on the sheath scale (the ionisation

length being usually much larger than the sheath dimensions), therefore only two processes are taken into account: elastic scattering for electrons and charge exchange with neutrals for ions. Most of the collision models handling charged-neutral collisions use the direct Monte-Carlo scheme, in which all species carry information about their collision probability. So a collision probability is calculated for each of the reactant species depending on their velocity from a known cross-section. After that a random number is generated. The reaction occurs, if the generated random number is smaller than the collision probability.

For the purposes of present research however it is desirable to produce a simulation that compares with theoretical models which generally assume a collision frequency independent of velocity. Therefore, initially

$$\nu_m = n_g \sigma u, \tag{2.11}$$

is calculated, where ν_m is the collision frequency, n_g is the neutral gas density, σ is the energy dependent cross-section and u is the relative velocity of the participating species. Finally, $\nu_m \Delta t$ randomly picked super-particles undergo a collision, at each simulation step.

2.3 Single Ion Species Model - An Implementation

In this section the single ion species semi-infinite plasma in contact with an electrode in the case of collisions is going to be studied. We will derive the expression for electric field inside bulk plasma by using the force equation. One of the boundary condition inside bulk plasma is determined by this electric field, discussed in next section. It is assumed here that the electrode is perfectly absorbing and the plasma is isothermal in such a way that $\nabla p = k_B T \nabla n$ [6]

. Secondary electron emission from the electrode is not considered here. The objective is to construct a simulation capable of modelling a finite portion of this plasma from an arbitrary point inside the bulk, up to the electrode, and drive this region with a sinusoidal RF current

$$I_{rf} = I_0 \, sin \, (\omega_{rf} \, t). \tag{2.12}$$

Now the question is how particles can be loaded from the boundary and what should be the boundary condition for the electric field. The equilibrium macroscopic force equation for species *'s'* in the bulk of the plasma under considerations (neglecting the inertial term $\vec{u}.\nabla\vec{u}$ and magnetic field $\vec{B}$), is written as

$$q_s n_s E - kT_s \frac{dn_s}{dx} - m_s n_s \nu_{ms} u_s = 0, \tag{2.13}$$

where ν_{ms} is the momentum transfer frequency due to collisions of the relevant species. By equation (2.13)

$$u_s = \frac{q_s E}{m_s \nu_{ms}} - \frac{kT_s}{m_s \nu_{ms}} \frac{\nabla n_s}{n_s}. \tag{2.14}$$

Flux of electrons and ions at any point must be equal in order to forbid the charge built-up. So for both species, with $\Gamma_e = \Gamma_i = \Gamma$ (also $\Gamma = n_s u_s$) and $n_e = n_i = n$, we have

$$\mu_i n E - D_i \nabla n = -\mu_e n E - D_e \nabla n, \tag{2.15}$$

which gives the electric field inside the bulk

$$E = \frac{D_i - D_e}{\mu_i + \mu_e} \frac{\nabla n}{n}. \tag{2.16}$$

For one dimensional case

$$E = \frac{D_i - D_e}{\mu_i + \mu_e} \frac{1}{n} \frac{dn}{dx}. \tag{2.17}$$

Substituting this value of E into the common flux relation (in ion equation) we have

$$\begin{aligned}\Gamma &= \mu_i \frac{D_i - D_e}{\mu_i + \mu_e}\nabla n - D_i \nabla n, \\ &= -\frac{\mu_i D_e + \mu_e D_i}{\mu_i + \mu_e}\nabla n.\end{aligned} \tag{2.18}$$

For one dimensional case

$$\Gamma = -\frac{\mu_i D_e + \mu_e D_i}{\mu_i + \mu_e}\frac{dn}{dx} = -D_a \frac{dn}{dx}, \tag{2.19}$$

where $\mu_s = |q_s|/(m_s \nu_{ms})$ are the mobilities, and $D_s = kT_s/(m_s \nu_{ms})$ are the diffusion coefficient. D_a is the ambipolar diffusion coefficient. The density profile of the species in the absence of ionisation is linear inside the bulk plasma.

2.3.1 Boundary Conditions and Initial Loading

In most cases, the boundary conditions are very important for the simulation region's physical processes. Different boundary conditions may cause quite different simulation results and improper sets of boundary conditions may introduce nonphysical influences on the simulation system. From previous discussion it is clear that the constant flux is the parameter that determines the behaviour of the bulk plasma boundary. One can solve or find out the average velocity of the species $u_b = \Gamma/n_b$ at the boundary by setting a value for the flux and calculate somehow what the density n_b should be at the boundary. On the other hand, the electric field at the boundary can be calculated by equation (2.17), if gradient of the density is known at the boundary. How to get the values of the density and its gradient is discussed in section (2.3.2).

Picking the density at the sheath edge as a controlling parameter in the simulation is one way of determining flux. Then, *assuming* that the ions will arrive at the sheath edge with an average velocity *i.e.* Bohm velocity $u_B = (k_B T_e/m_i)^{1/2}$ [36], the ion flux can be calculated.

An arbitrarily chosen linear density profile is assumed, to start the simulation. Ion super-particles are loaded with velocities obtained from a warm Maxwellian drifting at a velocity $u(x)$ such that $n(x)u(x) = \Gamma = const$, where $n(x)$ is the ion density at any point. The quasi-neutrality is preserved by subsequently loading sufficient electron super-particles from a warm-drifting Maxwellian. There are different initial loading schemes and could be implemented accounting for example for a density drop in the sheath region or for particles which have suffered collisions, but it will not be discussed here.

2.3.2 Particle Loading

The loading of the particles at the boundary has to be done from particle distributions which are as consistent as possible with the boundary conditions. The artificial "*source sheath*" is created at the boundary in case of failure, as discussed in the literature [107]. The simulation procedure is illustrated in the flow chart given in figure 2.1. Once the simulation is started, at every step $\Gamma\Delta t/\mathcal{W}_i$ ion super-particles that are obtained from a warm drifting Maxwellian flux are injected from the boundary in the simulation. The drift u_b of the flux is such that $\Gamma = n_b u_b$. Moreover, almost all RF current is carried by the electrons because of $m_e << m_i$. Again the displacement current at the boundary is negligible because $\omega_{pe} >> \omega_{rf}$, so the loading of electrons can be done in following way: by calculating the amount of charge $Q(t)$ that has left or entered the simulation region from the bulk boundary (also include the newly loaded ions) at that particular step, sufficient electron super-particles are injected so as to conserve the total current *i.e.* $(Q(t) - J_{DC}\Delta t - J_{rf}\Delta t)/e\mathcal{W}_e$ super-particles. The electron super-particles are picked from time-dependent warm drifting Maxwellian fluxes having drift velocity equal to $u_d = J_{rf}(t)/en_b$.

As the simulation evolves with time, the density profile is averaged near

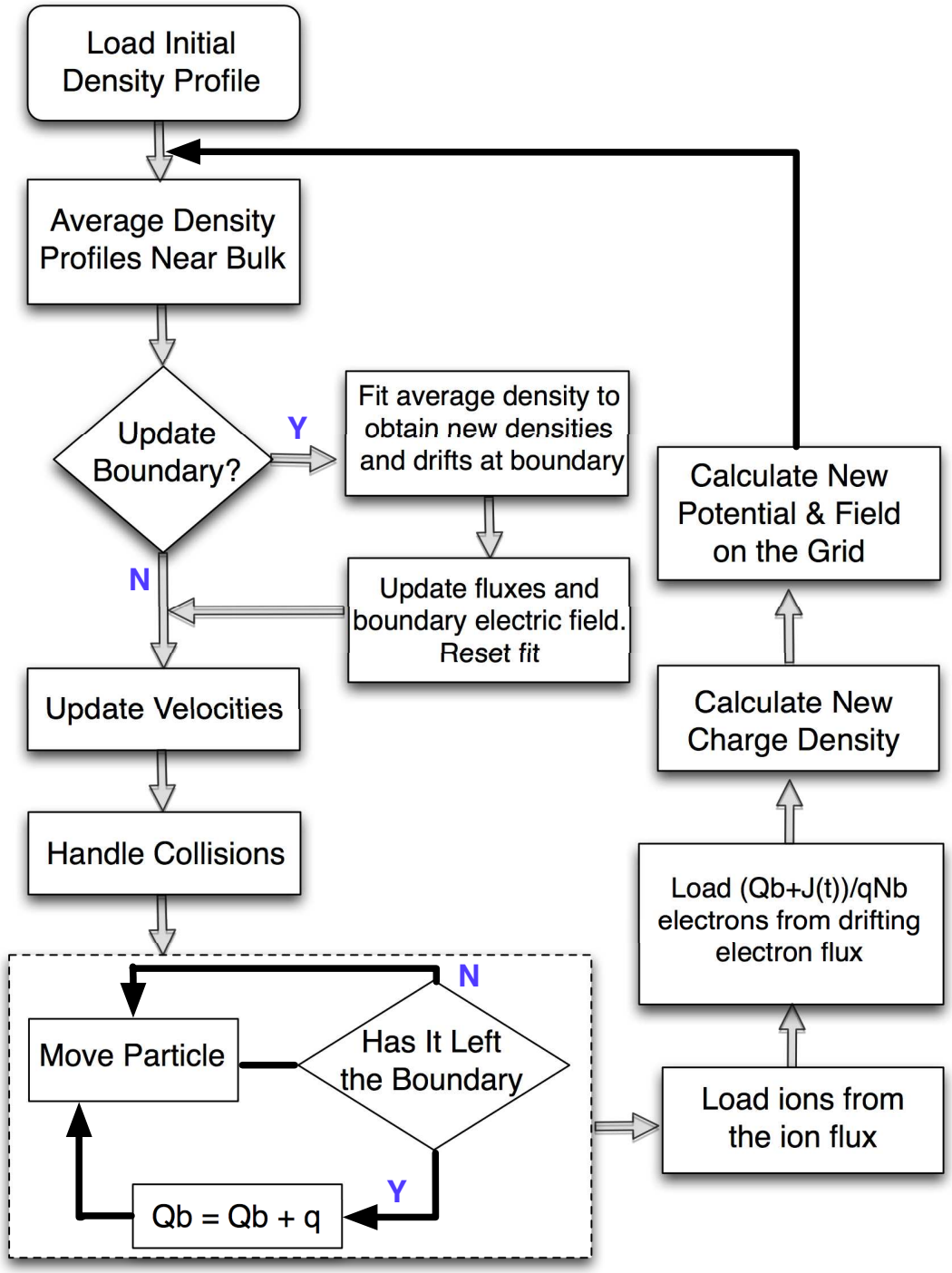

Figure 2.1: *Flow of PIC Simulation*

the bulk boundary. At a certain time (normally several ion plasma periods) the average density profile in the vicinity of bulk boundary is fitted by straight line. The extrapolation of the line to the boundary yields what the new density should be at the boundary. Also by knowing the flux, the loading fluxes for both ions and electrons are altered accordingly so as to account for the new drift velocities. Finally the electric field at the boundary is recalculated by equation (2.17). This process runs until steady state is reached.

2.4 The Collisionless Case

In previous sections, plasmas that have some finite collision frequency have been discussed. In some problems, the plasma is treated as completely collisionless (by keeping neutral gas pressure zero) and in this case previous analysis is applicable but with some simplifications. Here a presheath region for the planer geometry cannot exist without collisions, therefore the ions injected into the bulk region of the simulation area have to already satisfy the Bohm criterion. So the ion loading is done by a warm Maxwellian drifting at the Bohm velocity. This topic will be discussed again in the next chapter.

2.5 Input Parameters and Diagnostics in Code

The important input parameters used to run simulation are shown in table (2.2). These are stored in a file which is parsed at the beginning of the simulation. The diagnostics that the user would like to access are also indicated in the same file. The most useful diagnostics that are built-in to the simualtion are shown in table (2.3). These diagnostics are resolved in both time and space. In order to improve accuracy, diagnostics are averaged over the RF cycles, once convergence has occured and the simulation has reached equilibrium. For the

Table 2.2: *Input parameters for the PIC code*

General Parameters		Species Parameters		Drive Parameters	
Δt	Time-step	q_s	Charge	f_{rf}	RF frequency
N_c	Number of cells	m_s	Mass	I_{rf}	RF Current amp.
l	Simulation length	T_s	Bulk Temperature	ϕ	RF phase offset
N_{tp}	Time-steps/period	Γ_s	Particle flux		
N_t	Number of steps	$\mathcal{W}_s$	Super-particle weight		

velocity distribution diagnostic, the user can choose the temporal and spatial interval for the output distribution.

Table 2.3: *Important Diagnostics in the PIC code*

General Diagnostics	Species Diagnostics
Electric Field	Density
Potential	Velocity Distribution
Displacement Current	Temperature
Potential Energy	Phase-space
	$f(u)$ moments

2.6 Summary

Summarising, a method for modelling a semi-infinite plasma in contact with an electrode is presented which is based on particle-in-cell scheme. This implementation has couple of advantages. One is, with help of this it is possible to simulate the sheath structure and the plasma in its vicinity independently of the rest of bulk plasma. This achieves extended diagnostic detail that would be

computationally very expensive in a generic particle-in-cell simulation. Other one is, conditions that are usually used by analytic models can be imposed so that the validity of these models can be tested.

In the context of present research work, it is assumed here that ionization is not an important process on the sheath scale. The collisional model involves only charge-exchange for the ions and elastic scattering for the electrons. However the plasma can be treated as collisionless, in which the method is simplified.

Finally, simulations with only one ion species is presented here and only in planar geometry. However, the generalisation of the method to cylindrical and spherical geometries is possible and more ion species could be included.

CHAPTER 3

Stochastic Heating Phenomenon in Single Radio Frequency Capacitively Coupled Discharges: The Fermi Acceleration Mechanism

3.1 Introduction

Electrons are heated by time-varying fields in radio frequency (RF) discharges. In the case of a uniform oscillating electric field, a single electron is in coherent velocity of motion that lags the phase of the electric field force $-e\mathbf{E}$ by 90°. As a result, the time-average power transferred from the field to the electron is zero. This phase coherence of motion is disturbed by electron collisions with other particles, leading to a net transfer of power. To visualize this in detail, let us consider an ensemble of $\mathbf{n}$ electrons per unit volume. It is possible to write

the expression for macroscopic current density as

$$J = en\mathbf{u}, \tag{3.1}$$

where $\mathbf{u}$ is the average velocity of electrons, and J is the current density. It is possible to relate the amplitudes of J and E *i.e.* the strength of electric field through a local conductivity:

$$J_0 = \sigma_p E_0, \tag{3.2}$$

where $\sigma_p = e^2 n/m(\nu_m + j\omega_{rf})$ is the plasma conductivity and ν_m is the electron collision frequency for momentum transfer. The ohmic power transfer per unit volume is

$$P = \frac{1}{2} Re\,(J_0.E_0^*) = \frac{1}{2}\,|E_0|^2\, Re(\sigma_p) = \frac{1}{2}\,|J_0|^2\, Re(\sigma_p^{-1}). \tag{3.3}$$

It can be seen from equations (3.1) and (3.2) that the average electron velocity $\mathbf{u}$ oscillates coherently with the electric field and the phase offset between them is 90° in absence of collisions ($\nu_m = 0$). Although the average velocity is coherent with the field, the basic mechanism that converts electric field to thermal energy is the breaking of the phase-coherent motion of individual electrons by collisions and is not present here, therefore, the energy exchange between the field and the electrons, averaged over a whole cycle of the periodic field, is zero. In contrast, the phase of the electron oscillation motion in the field is randomized locally by inter-particle collisions ($\nu_m > 0$), individual electrons lose phase coherence with the field which gives rise to heating.

Landau [39, 109] was the first who suggested that a spatially *nonuniform* electric field by itself might lead to electron heating, even in absence of inter-particle collisions, provided that the electrons have sufficient thermal velocity to sample the field inhomogeneity. He demonstrated the collisionless damping of electrostatic waves in a warm plasma and it is variously referred in literature as *collisionless, non-collisional, stochastic, transit time,* or *anomalous* heating

or dissipation. In this case, the current density (J) at some point in the plasma is defined not only by the electric field (E) at that point, but by an integrated effect over the neighboring space. The time-varying field seen by an individual "thermal" electron is non-periodic due to the spatial variation. As a result the phase coherence can be lost since the field "observed" by an electron is non-periodic even if the field itself is strictly periodic. Under these conditions the loss of phase coherence can allow heating to occur.

The spatial variation of the time-varying field is strongly nonuniform in capacitive RF discharges and also in almost all discharges. Inside the bulk region of plasma this electric field is due to the ambipolar and RF fields, and is very weak in nature. Although this field can change the drift velocity and density of electrons and maintain quasi-neutrality, it contributes little towards heating. On the other hand, inside the sheath region near the plasma boundaries, the electric field has a strong spatial and temporal dependence and is significantly larger than the bulk plasma field. An electron, being confined between the DC ambipolar and boundary sheath potential undergoes thousands of back and forth collisions. Here an electron interacts repeatedly with the high field sheath regions, but interacts weakly during its drift through the bulk plasma. This idea suggests a dynamical model to study the energy transfer and loss of phase coherence during the electron interaction with highly oscillating sheath. This model was first introduced by Fermi [48] and will be discussed in the next section. Collisionless heating is observed in experiments as well as in simulations, and will be the key issues of discussion in this chapter.

3.2 Fermi Acceleration

Historically, Fermi acceleration is thought to be the primary mechanism by which particles gain energy beyond the thermal energy in astrophysical shock

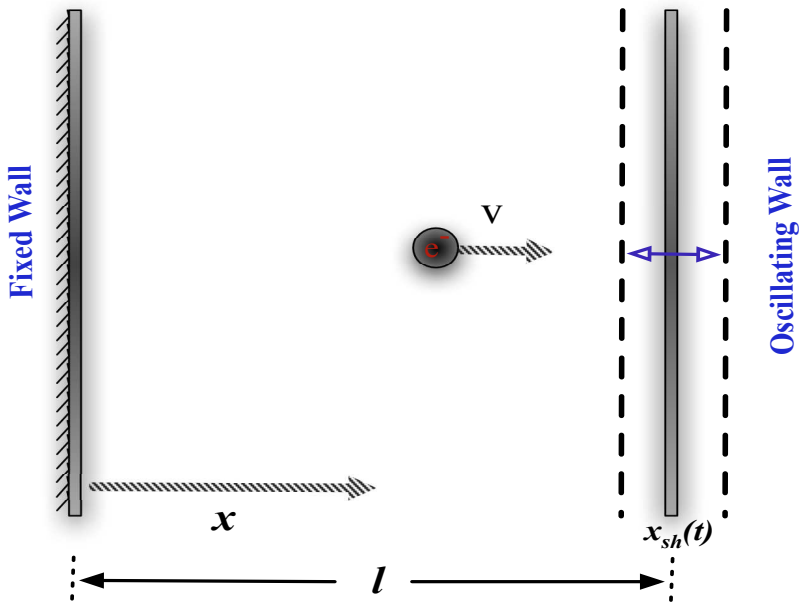

Figure 3.1: *A particle bounces between a fixed and as oscillating wall in Fermi acceleration mechanism.*

waves. In the usual model of Fermi acceleration, the wall oscillation motion is specified and the motion of the particle is then determined. From the structure of the motion of the particle in the velocity-position phase space, the conditions for phase randomization and the heating rates can be determined. However, the corresponding problem of collisionless electron heating in discharges has additional complexity, because the spatially nonuniform *RF* heating fields must be determined self-consistently with the electron motions. This self-consistent problem has been treated within conventional (warm plasma) kinetic theory for *RF* capacitive discharges assuming that all electron phases are randomized.

According to Fermi model, a particle bounces elastically between either a fixed and an oscillating wall or two oscillating walls (see figure 3.1). Then the change of velocity of a particle incident on the wall with velocity $\boldsymbol{v}$ can be

written as

$$v_r = -v + 2u_w, \tag{3.4}$$

where v_r is the velocity of the particle after reflection and u_w is the velocity of the wall at the time of the collision. Equation (3.4) shows that the particle either loses or gain energy depending on whether the particle and wall collide while moving towards the same (in phase) or opposite direction (out of phase). According to Fermi's argument, the particle will on an average gain energy because head-on collisions are most frequent, provided there is no phase correlation between the collisions.

The *fermi acceleration* process has been studied extensively as a paradigm in physics and also applied in different fields. Initially very basic work has been done to find the conditions under which phase coherence could be lost using a classical model of Hamiltonian dynamics [110]. This model of energy gain by repeated collisions of a particle with an oscillating wall was studied numerically by Ulam *et al.* [111], who observed that the particle motion appeared to be stochastic, but did not increase its energy on an average. Ulam's result was explained by subsequent authors with help of the combination of numerical and analytical work. Zaslavskii and Chirikov [112] investigated the condition in which the motion of particles collide with objects whose motion is completely deterministic (a sawtooth wall velocity was assumed), and derived conditions for the stochastic behaviour of a one-dimensional system. Similar studies has been done by Brahic [113]. A "simplified" Hamiltonian mapping, in which the oscillating wall transfer momentum to the particle but occupies a fixed position, was introduced by Lieberman and Lichtenberg [114] and studied for arbitrary wall velocities [110, 115]. Detailed discussion on Fermi acceleration can be found in several review articles [116–118].

3.3 Capacitive RF Discharges - Implementation of Fermi Acceleration

In early work, Gabor *et al.* [119] proposed an idea of electron interaction with *RF* field in their attempt to resolve the "*Langmuir paradox*" of a Maxwellian electron distribution in the positive column of a low pressure mercury arc *DC* glow discharge having negligible electron-electron Coulomb collisions. This was an astonishing result because in the pressure range where the measurements were taken the electron mean free path largely exceeded the tube dimensions. These results were explained by the self-maintained *RF* oscillations near the *DC* sheath edge of positive column dispersing the electron velocities. They believed that the electron interaction with the *RF* oscillations in the sheath was without energy exchange and maintained solely by the energy flux of low energy electrons, thus, generating a high energy tail of the distribution. Later, Pavkovich and Kino [120] and Gould [121], found a numerical solution of the appropriate Boltzmann equation. By analyzing the wall sheath impedance at frequencies close to the plasma frequency, they showed that the electron reflection in the oscillating sheath is accompanied by *RF* energy absorption due to the electron-wave interaction.

In the early 1960s, Mayer [122] was the first one who discussed collisionless heating through Fermi acceleration in the context of *RF* plasma sheaths. Later Godyak [28] discussed explicit application of Fermi acceleration to electron heating in capacitive discharges. He calculated the power deposition to the plasma for a *DC* sheath with a small sinusoidally vibrating fluctuation, and suggested that Fermi acceleration might be a major mechanism to sustain a capacitive discharge at low gas pressures. These ideas were further developed by Godyak [29, 123] and by Akhiezer and Bakai [124]. The later authors used

a simplified Fermi model to calculate the heating rate. The interaction of hot electron distribution with the RF field was studied by Alanakyan [125], and they observed that the distribution function obeys a power law in energy space. Goedde *et al.* [51] developed a partial self-consistent model of an RF discharge by assuming a sinusoidal movement of the sheath, involving the Fermi acceleration mechanism with some physical constraints. According to this model, electrons are continuously injected into a capacitive discharge at low velocity and are lost by inelastic collisions or escape to the walls at higher velocity, and determine the steady state distribution, finding a power law electron energy distribution function *i.e.* $f(E) \propto E^{1/2}$. An almost fully self-consistent model of the sheath was proposed by Lieberman [30]. Power deposition due to the Fermi acceleration mechanism is calculated with this model. For the present work this model is of particular importance, because it provides the most complete basis for comparison.

One of the other alternative possibilities to describe and evaluate collisionless heating was proposed by Kortshagen *et al.* [126]. It is based on the non-local solution of the space and time dependent Boltzmann equation by reducing it to a zero-dimensional space-time independent equation. This equation includes the space-time averaged energy diffusion coefficient $D(E)$, which gives all information required for the calculation of the power deposition to electrons. Smirnov and Kaganovich with others, used the above approach and treated RF discharges [31, 127] and stochastic heating specifically [128–130]. Phase randomization and energy diffusion processes due to non-linear effects have been investigated in Lichtenberg [118] and Buddemeier *et al.* [131] and further classified by Kaganovich *et al.* [129].

3.3.1 Stochastic Heating - An Experimental Confirmation

Early experimental evidence of stochastic heating are described in Godyak [29], Godyak *et al.* [123], Godyak [33], and Popov *et al.* [132] and are summarized in Godyak [32]. Electrical and plasma parameters were studied in a parallel-plate capacitive RF discharges symmetrically driven at 40 MHz to 110 MHz in mercury vapor in the literature. The current-voltage characteristic, the RF power, the plasma density and the electron temperature were simultaneously measured in the mercury, in the pressure range between 2×10^{-4} Torr and 1×10^{-1} Torr. The effective collision frequency ν_{eff} versus pressure was evaluated from the shape of the measured discharge current-voltage characteristic [33, 123]. Their results showed that as the pressure reduces, the effective collision frequency levels off to some finite value instead of dropping linearly as would be the case if only ohmic heating was present. The same was investigated by Popov and Godyak [132], but directly by measuring the RF power absorbed by the discharge to calculate the ν_{eff}. In all these experiments the measurements were done at relatively low RF voltages, and the power absorption due to ion acceleration in the RF sheaths was neglected.

A thorough experimental study of symmetric RF discharge characteristics in argon gas at a fixed frequency of 13.56 MHz and for a pressure range varying from 3 mTorr to 3 Torr has been performed by Godyak and Piejak [44] and Godyak *et al.* [75, 133]. The discharge length and diameter were 6.7 cm and 14.3 cm respectively, in an approximately uniform plane parallel configuration. They performed measurements of the RF voltage, RF current, total power absorbed, the central plasma density n_0, mean electron energy, electron energy distribution function (EEDF), ion current to the electrodes and DC bias voltage in the RF sheath. By averaging $V_{rf}(t)\, I_{rf}(t)$ over an RF cycle, the total power

deposition P_{tot} was calculated, and n_0, the mean electron energy and EEDF were determined using Langmuir probes [44, 75, 133]. Also, the power deposition to the ions P_{ions} was determined from the sheath DC bias voltage and the ion current. With the help of plasma conductivity formula, the collisional power absorption P_{ohm} in the plasma bulk by the electrons due to ohmic heating was calculated and it was compared to the total RF power transferred to the plasma electrons $P_{el} = P_{tot} - P_{ions}$. It was observed that at relatively high pressure ($p \geq 0.1$ Torr), the power absorption is entirely due to collisional dissipation, *i.e.* $P_{el}/P_{ohm} \approx 1$. At lowest pressure ($p \approx 3$ mTorr), collisionless power deposition could be thousands of time larger than the ohmic power deposition *i.e.* $P_{el} \gg P_{ohm}$. Such a large difference between P_{el} and P_{ohm} in the collisionless heating regime is due to the stochastic heating in the RF sheath, which produces a population of high energy electrons that maintain the discharge ionization. A simultaneous drop in collisional electron heating in the plasma because of bulk electron cooling and the associated decrease in ν_m due to the Ramsauer effect is also observed.

It was reported by Godyak *et al.* [44] that the electron cooling occurs during the heating mode transition when the discharge switches from a collisionally to a stochastically dominated mode. There is also a dramatic change in the shape of the EEDF during this process [133]. It was observed that in the ohmic heating regime the EEDF is Druyvensteyn-like, whereas in the collisionless heating regime, the EEDF could be well approximated by a bi-Maxwellian distribution with a hot and cold electron population. This transition is accompanied by a corresponding sharp change in plasma density and mean electron energy [44]. In the stochastic heating regime the most of electrons have a very low energy, and are trapped by the ambipolar DC field. These low energy electrons are not able to reach the RF sheaths where stochastic heating takes place. So the

low energy electrons have a very low electron-atom collision frequency and thus they collisionlessly oscillate in a weak RF field and are unable to gain energy. On the other hand, the high energy electrons overcome the ambipolar potential and effectively interact with the oscillating RF sheath, bouncing between them. The phase randomization can arise either directly from the dynamics or can be induced by exogenous stochastic forces (e.g., inter-particle collisions) and these electrons can be heated.

Finally, another kind of EEDF transition due to change in RF power was obtained and studied by Buddemeier *et al.* [50] through experiment and numerical simulation. Here evolution of the measured electron probability function with discharge current (and voltage) at a fixed low argon pressure (67.4 mTorr), from a Druyvesteyn-like distribution at low discharge voltage to a two-temperature distribution at higher voltage. This transition is associated with the nonlinear nature of electron heating in the RF sheath. At small discharge voltage, the sheath heating is small or comparable to the bulk collisional electron heating. As RF current increases, the stochastic heating begins to dominate with a corresponding restructuring of the electron energy distribution.

Above discussion shows that there is experimental evidence for collisionless heating but not a detailed experimental characterization, because no one yet succeeded in making direct measurement of fields and currents in capacitive discharges. Other kinds of experiments, such as phase resolved optical emission spectroscopy [134–137], also provide evidence that basic ideas are correct about these heating effects, but again, such measurements do not directly corroborate the theories. Due to all of these reasons simulation evidence of stochastic heating to validate theories [1, 43, 58, 107, 138] are very important.

3.3.2 Simulations

Simulation studies has been significantly contributed to understand stochastic heating in general, or particularly collisionless heating through Fermi acceleration. The existence of stochastic electron heating produced by oscillating electrode sheath in capacitively coupled discharges at low pressure has been studied by Monte Carlo and particle-in-cell (PIC) simulation techniques in last few decades [41, 50, 53, 54, 59, 107, 138]. Stochastic heating due to electron reflection from oscillating sheaths was observed by Kushner [53] using a Monte Carlo calculation. Monte-Carlo simulations assumes an analytic form for the electric field with which the electrons interact and calculate power deposition. This have been showed by Kushner [52] and Wendt *et al.* [54].

Experimental measurements done by Godyak and Piejak [44] were also compared with a PIC simulation obtained by Vahedi *et al.* [103]. It was done in argon plasma and a good agreement was found. The transition of the shape of the EEDF from Druyvensteyn-like (at 500 mTorr) to bi-Maxwellian (at 70 mTorr) was also observed. Vender and Boswell [67] showed the existence of more energetic electrons near the plasma edge due to local electron heating increases the ionization there at higher pressure ($\lambda_e \ll l$). The ionization is not constant, but follows the density variation in space and time of the more energetic electrons. Vender and Boswell [59] also pointed out the importance of electron inertia, power losses to the electrodes, and the lack of self-consistency in models dealing with electron-sheath interaction. Using a semi-infinite PIC simulation very similar to that described in chapter 2, Surendra and Vender [107] studied heating in a collisionless sheath and provided scalings using the ratio of the drift velocity to the thermal velocity of the electrons as a parameter. Surendra *et al.* [138] used PIC simulations in a model gas based on helium and showed that even if the secondary electron emission coefficient is set to

zero, high-energy electrons which acquire their energy near the plasma-sheath interface propagate through the discharge.

Several PIC codes have examined the spatial distribution of the electron power absorption. The absorption is positive and large enough near the RF sheath edge but it can become negative within certain regions in the discharge bulk under the conditions of strong collisionless heating [55, 139]. This is particularly apparent in simulations at low pressures where the ohmic dissipation (which is always positive) is small. When the phase of electron current (transferred from the stochastic heating at the RF sheath edge by the electron thermal motion) differs from the phase of the local electric field by more than 90^0 the negative power absorption occurs. The existence of negative power absorption inside the bulk region of capacitive RF discharges has not been confirmed yet by experimental measurements, although this phenomenon is indicated by some experimental results [140]. Another approach towards collisionless heating associated with RF sheath oscillations in capacitive RF discharges has been discussed by Surendra and Dalvie [56] and by Turner [42]. They showed that an approximation to the heating can be obtained within a macroscopic (fluid) theory by incorporating pressure effects that arise during the expansion and contraction of the sheath in a nonhomogeneous plasma model. The pressure effect is caused by the difference in plasma density and electron energy between the bulk plasma and the near-sheath plasma. When the sheath expands, electrons flow into the adjacent bulk plasma and are compressed. At the same time, electrons are rarefied as they flow into the opposite, collapsing sheath. Turner showed that using finite electron thermal conductivity, these simultaneous rarefactions and compressions of the electron gas produce nonequilibrium thermal disturbances, and the net work done is not zero. In this way, kinetic effects are incorporated approximately into fluid model. Solving the fluid equations

with the electron energy balance equation, Turner verified this approach using PIC simulation. The terms in the moment equations derived from the Boltzmann equation has calculated explicitly through PIC simulation by Surendra and Dalvie [56]. They showed that electron heating can be separated into two terms, attributed to ohmic heating and pressure work respectively. An exhaustive comparison of the results obtained from different types of models including fluid, kinetic and hybrid simulations with the experimental results of Godyak was undertaken by Surendra [141].

In final comment, the Fermi acceleration paradigm has been applied in capacitive RF discharges here as follows: electrons having temperature $T_e \approx 2.5$ eV move freely in the bulk, until they interact with the oscillating fronts of the sheath electric fields. They reflect after collision. Since the sheath voltage is the order of hundreds to thousands of volts and the electron temperature is very small *i.e.* $T_e \approx 2.5$ eV, the electrons can be treated as "particles" and the sheath field as a "hard wall". Here the collisions can be considered elastic. This approximation is referred in literature as the "Hard Wall Approximation". We will study stochastic heating model of single frequency discharges for self-consistent ion densities. We will also investigate the nature of stochastic heating, and how it depends on various parameters.

3.4 Hard Wall Models: Self Consistent Discharges

In this section, the capacitive RF sheath structure is described and the instantaneous power deposition is calculated with the help of 'hard wall' model. Problems with 'hard wall' model is also discussed. Shortcomings of the Godyak model and the Lieberman [30] model are discribed here. Kaganovich's [34] ki-

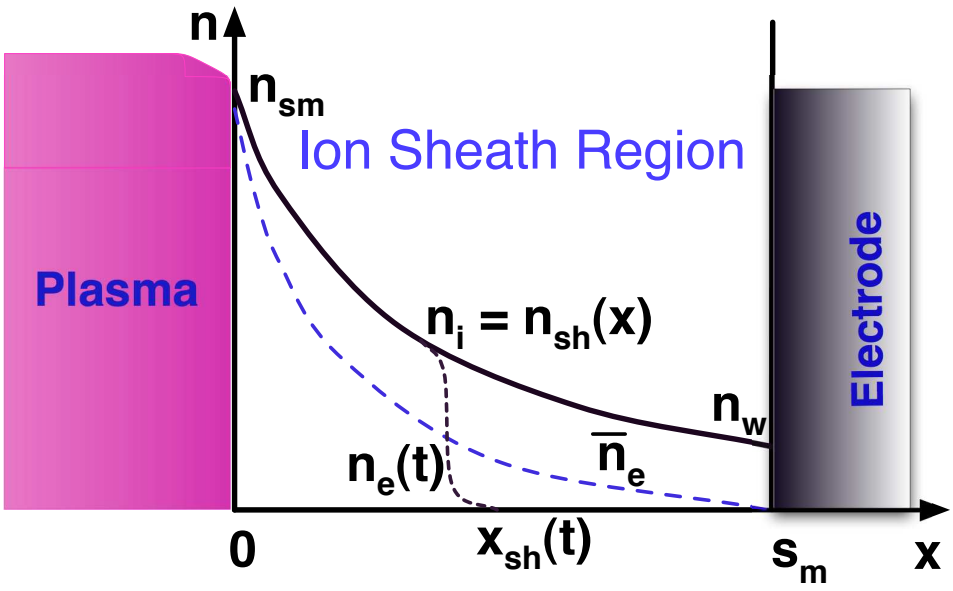

Figure 3.2: *Schematic diagram of the densities in a high voltage capacitive RF sheath.*

netic two step model is discussed and the time average stochastic heating given by Lieberman [30] and Kaganovich *et al.* [91] is also calculated.

Let us start with the calculation of stochastic heating for a collisionless nonuniform high voltage RF sheath [30]. The structure of the RF sheath is shown in figure 3.2. Ions enter the ion sheath boundary at $x = 0$ with a velocity of the order of the Bohm speed $u_B = (k_B T_e/m_i)^{1/2}$, are further accelerated within the sheath by the sheath potential, and finally strike the electrode at $x = s_m$ with high energies. The ion motion is collisionless. Since the ion velocity increases as it approaches the electrode, due to ion flux conservation, the ion density $n_{sh}(x)$ decreases continuously from its maximum value n_{sm} (at the ion-sheath plasma boundary) to its minimum value n_w (at the electrode) (see figure 3.2). So in a self-consistent discharge, the plasma density is not uniform. In the figure, $x_{sh}(t)$ is the instantaneous position of the oscillating

electron sheath edge. The electron sheath edge oscillates between the wall at $x = s_m$ and the ion sheath boundary at $x = 0$. A self-consistent analysis of the dynamics of a high voltage collisionless capacitive RF sheath is given in Lieberman [30]. We will briefly discuss it here.

Let us consider a single electron incident on the sheath with velocity v, which collides with the sheath electric field. Assuming the collision is elastic, the incident electron reflects with a velocity

$$v_r = -v + 2u_{sh}, \tag{3.5}$$

where u_{sh} is the velocity of the plasma-sheath boundary. The difference in the kinetic energy of electron after and before collision will be equal to its energy gain or loss *i.e.*,

$$\Delta E = \frac{1}{2} m_e (v_r^2 - v^2) = 2 m_e u_{sh} (u_{sh} - v). \tag{3.6}$$

Now consider the whole electron distribution function and assume that only those electrons arrive at the sheath edge which have a velocity higher than the sheath velocity. So the instantaneous power deposition $S_{stoc}(t)$ is equal to

$$\begin{aligned} S_{stoc}(t) &= \int_{u_{sh}}^{\infty} (v - u_{sh}) f_{sh}(v,t) \Delta E \, dv \\ &= -2 m_e \int_{u_{sh}}^{\infty} u_{sh} (v - u_{sh})^2 f_{sh}(v,t) \, dv, \end{aligned} \tag{3.7}$$

where f_{sh} denotes electron distribution function at the sheath edge. The electron distribution function can be assumed at the sheath edge as a drifting Maxwellian

$$f(v) = n_e \left(\frac{m_e}{2\pi k_B T_e} \right)^{\frac{1}{2}} exp \left[- \frac{m_e (v - u_d)^2}{2 k_B T_e} \right], \tag{3.8}$$

where u_d and T_e are the electron drift velocity at the sheath edge and electron temperature respectively. We will now show that in any "hard wall" model which has continuous current at the electron sheath edge, the instantaneous

heating power given by equation (3.7) will vanish identically, within the framework of hard wall assumptions. Let us begin by noting that it is always possible to write the incident particle velocity in equation (3.5) as the sum of the drift velocity of the incoming particle distribution, u_d, and a random thermal component v', so that $v = u_d + v'$. Similarly, the incoming particle velocity distribution function $f_{sh}(v)$ in terms of a non-drifting distribution function g such that $g_{sh}(v' + u_d) = f_{sh}(v)$ where $\int_{-\infty}^{\infty}(v' g_{sh}(v'))\, dv' = 0$. Then

$$\begin{aligned} S_{stoc}(t) = &-2m_e \left\{ \int_{u_{sh}-u_d}^{\infty} (u_{sh} - u_d)(v' + u_d - u_{sh})^2 g_{sh}(v')\, dv' \right. \\ &\left. + \int_{u_{sh}-u_d}^{\infty} u_d (v' + u_d - u_{sh})^2 g_{sh}(v')\, dv' \right\}. \end{aligned} \tag{3.9}$$

In the Godyak model $u_d = 0$, and in the Lieberman model $u_d = u_0$, where u_0 is the drift velocity at the ion sheath edge. But both of these cases are not defensible. In fact, the only choice consistent with current conservation at the electron sheath edge is $u_d = u_{sh}$. In this case the first integral vanishes and the second becomes

$$\begin{aligned} S_{stoc}(t) &= -2m_e u_d \int_0^{\infty} v'^2 g_{sh}(v')\, dv', \\ &= -2n_s u_d T_b, \\ &= -2n_0 u_0 T_b, \end{aligned} \tag{3.10}$$

where T_b is the effective electron temperature in the bulk plasma (which is assumed constant). Since n_0 is independent of time and u_0 is a periodic function averaging to zero, this result does not vanish instantaneously, but it is zero when averaged over time [58]. The physical significance of this outcome can be appreciated by considering the hard wall velocity exchange formula, equation (3.5), when $v = u_d + v'$ and $u_{sh} = u_d$. In this case $v_r = u_d - v'$, whereupon it becomes clear that when current is conserved, only the sign of the thermal part of the particle velocities is exchanged on reflection from the moving sheath, so

that the distribution of thermal velocities g_{sh} is the same for particles leaving the sheath as for those entering. This is why the first integral in equation (3.9) is identically zero. Although the energy of electrons does change on reflection at the electron sheath edge, this is necessary to preserve the drift energy, and is not to be considered as a heating effect, any more than the oscillation of electrons in the bulk plasma is considered a heating effect in the absence of collisions. Thus the non-vanishing term in equation (3.9) is a contribution to the oscillation of the electron drift energy, its presence required by the assumption of a point-like electron sheath edge. To show a heating effect, a mechanism must exist for modifying the distribution of thermal velocities. There is, therefore, no such phenomenon as "hard wall" stochastic heating when a current conservation condition must be satisfied in the vicinity of the wall. The only possible exception to this result appears to arise when the thermal velocity distribution of the incoming electrons varies with time. Lieberman has obtained a positive net power deposition for a collisionless RF sheath driven by a sinusoidal current $J(t) = \tilde{J}_0\, sin\,(\omega_{rf} t)$, by assuming $f_{sh} = g_{sh}(v - u_0)$ instead of $f_{sh} = g_{sh}(v - u_{sh})$. Here u_0 is the electron drift velocity at the Bohm point. By using the analytic expression for the sheath velocity calculated in Lieberman [30], with above assumption, $S_{stoc}(t)$ becomes

$$S_{stocL} = \frac{3\pi}{32} H m_e n_{sm} \bar{v}_e u_0^2\,, \tag{3.11}$$

where $\bar{v}_e = [8k_B T_e/(\pi m_e)]^{1/2}$ is the mean electron thermal velocity, n_{sm} is the ion density at the ion-sheath plasma boundary and $\mathbf{H}$ is a dimensionless parameter given by equation (1.5). Taking the drift velocity of the electrons (u_0) at the sheath edge violates the electron flux continuity and therefore current conservation: for the flux to be conserved between the Bohm point and the electron sheath edge, the essential condition is $n_{sh} u_{sh} = n_e(x) u_e(x) = n_0 u_0$ everywhere. Since the electron density drops as we approach the electron sheath

edge, it is apparent that u_{sh} has to increase in order to satisfy continuity, and therefore Lieberman's model is inconsistent. Surendra and Dalvie [56] noticed it first and also remarked that using the correct drift velocity for the electrons produces zero net heating as already shown above.

Lieberman [30] also neglected the bulk oscillation, and neglecting the bulk motion tends to overestimate the stochastic heating. Kaganovich [34] investigated the kinetic effects that distort the electron velocity distribution from a Maxwellian by using a two-step ion density model. If the bulk motion is taken into account then the hard wall model can be used for the calculation of S_{stoc} has been shown by Kaganovich *et al.* [91]. The transitional electric field was calculated by Kaganovich, which gives the non-stationary component of the distribution required for the current conservation. He showed that this transitional field redistributes energy between the fast and slow electrons without substantially changing the total stochastic heating. We will briefly discuss it here.

Lieberman [30] described the self-consistent analysis of the dynamics of a high voltage collisionless capacitive RF sheath. At the electron sheath edge, the plasma density $n_{sh}[x = x_{sh}(t)]$, is given as a parametric function of the phase of the sheath motion $\phi = \omega_{rf}\, t$ (see figure 3.2). For condition $0 < \phi < \pi$, we have

$$n_{sh}(\phi) = \frac{n_{sm}}{HN(\phi) + 1}\,, \tag{3.12}$$

where

$$N(\phi) \equiv -\left(\frac{3}{8} sin\, 2\phi - \frac{1}{4}\phi\, cos\, 2\phi - \frac{1}{2}\phi\right)\,. \tag{3.13}$$

The electron plasma sheath edge starts at the ion sheath boundary where $n_{sh} = n_{sm}$ at $\phi = 0$ and reaches the wall or electrode where $n_{sh} = n_w$ at $\phi = \pi$. Thus the ion density at the wall is given by

$$n_w = n_{sh}(\pi) = \frac{n_{sm}}{1 + 3\pi H/4}\,. \tag{3.14}$$

Because of current continuity condition,

$$n_{sh}(\phi)\, v_{sh}(\phi) = \frac{\tilde{J}_0}{e}\, sin\, \phi = n_{sm} u_b\, sin\, \phi\,, \tag{3.15}$$

on an average the electron sheath velocity $v_{sh}(\phi)$ is much larger than the bulk electron oscillation $v_b(\phi) = u_b\, sin\, \phi$ that supports the current. The hard wall model used by Lieberman neglects this bulk motion to calculate S_{stoc}, given by equation (3.11).

A result for S_{stoc} for the nonuniform ion sheath density profile $n_{sh}(\phi)$ is derived by Kaganovich *et al.* [91] and is shown by equation (3.12). In his kinetic two-step model, Kaganovich [34] showed that the transitional electric field $E_1(x)$ redistributed energy from the fast to the slow electrons without affecting the total heating. Kaganovich *et al.* [91] used this result to justify a hard wall calculation for S_{stoc} in a nonuniform sheath, which neglected $E_1(x)$, but took the bulk oscillation into account. Note that the sheath velocity is given by the effective sheath velocity $(v_{sh} - v_b)$ in the reference frame moving with the bulk, and assuming that the electron velocity distribution is a stationary Maxwellian in this frame. Now by using equation (3.7), the final expression for stochasting heating given by Kaganovich *et al.* [91] is

$$S_{stocK} = G_K(H) S_{stocL}\,, \tag{3.16}$$

where

$$G_K(H) = \left\langle \frac{N(\phi)^2 sin^2\phi}{N(\phi) + 1/H} \right\rangle \approx \frac{H}{H + 1.1}\,. \tag{3.17}$$

Here $G_K(H) \to 1$ for large H and S_{stocL} provides an upper limit for S_{stocK}.

Finally by substituting equation (3.14) for n_{sm} in equation (1.5), we have

$$H = \frac{\tilde{J}_0^2}{\pi e \varepsilon_0 T_e \omega_{rf}^2 n_w (1 + 3\pi H/4)}\,. \tag{3.18}$$

Since $\tilde{J}_0$, T_e and n_w are all available from the PIC data, the above quadratic

equation (3.18) in H can be solved to obtain

$$H = -\frac{2}{3\pi} + \frac{2}{3\pi}\sqrt{1 + \frac{3\tilde{J}_0^2}{e\varepsilon_0 T_e \omega_{rf}^2 n_w}}\,. \tag{3.19}$$

Once H is known, n_{sm} can be calculated by using equation (3.14).

3.5 Single Frequency Self-Consistent PIC Simulation

It is clear from the previous discussion that for the basis of consistent theory, a hard wall approach is not sufficient. In kinetic theory and the kinetic-fluid approach [42, 43, 57, 142], it is not easy to see how to avoid the heuristic elements in a mathematically tractable fashion. The other possibility is that a better sheath model than that of Lieberman [30] is needed, in particular, because the representation of the electron sheath edge as a step function may be one of the less satisfactory approximations that feature in all models [143, 144]. In a further step to improve these models, the results should be compared with simulations and experiments. Simulations are the only choice because there are no experiments that fulfill the purpose. In this regard, it is to be noted that all theoretical models lead to a result given by the following equation

$$S_{stoc} = \frac{3\pi}{32} H m_e n_{sm} \bar{v}_e u_0^2 G(H)\,, \tag{3.20}$$

where **H** can be interpreted as a sheath structure factor defined by equation (1.5). All theories agree on the form given by the above equation (3.20) and this facilitates both the comparisons of theories and that of theories with simulations. Furthermore, if the theories are correct in agreeing on the above form, then we can set aide the differences between the theories and simply choose $G(H)$ to agree with simulation data. In effect, this approach has been pursued in recent work by Kawamura *et al.* [1]. It is briefly described here.

Kawamura *et al.* [1] conducted a PIC simulation of current-driven argon discharges in which both ions and electrons were moved. The applied *RF* frequency f_{rf} was 27.12 MHz and the *RF* current drive amplitude $\tilde{J}_0$ varied from $\tilde{J}_0 = 18 - 100$ A/m^2 for the density variation $n_{sm} = 5 \times 10^{14} - 6 \times 10^{15}$ m^{-3}. The corresponding value of H increased from 1.7 to 5.7. Here the electron

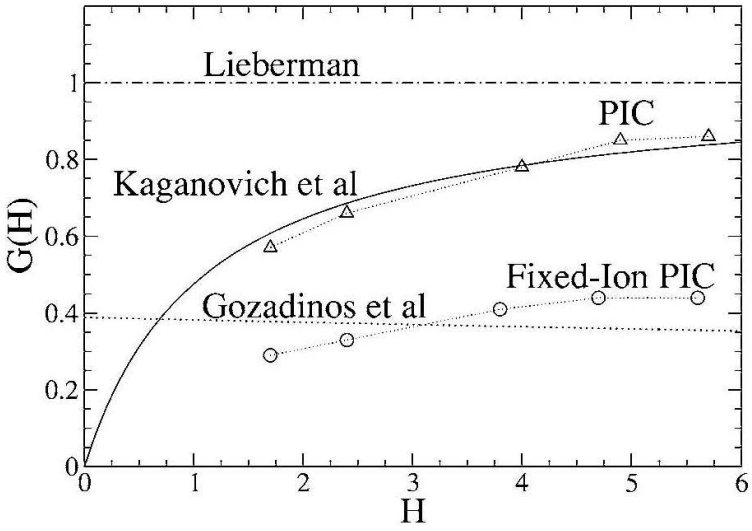

Figure 3.3: *Comparisons of different theoretical expressions with particle-in-cell simulations of stochastic heating in single frequency capacitive discharges, from Kawamura et al. [1]. The solid line denotes 'Kaganovich et al.' corresponds to equation (3.16) and the dashed-dot line denotes 'Lieberman' corresponds to equation (3.11). The number of data points are rather small i.e. five points from* $H = 1.7 - 5.7$.

temperature T_e is 2 eV and the ion temperature T_i is 0.03 eV. They concluded that simulation data takes the form of equation (3.20), and that equation (3.16) best agrees with their numerical values. These data are reproduced in figure (3.3). On these grounds, equation (3.16) is the most appropriate formula. Here it is to be noted that the number of data points is rather small, and an improved formula might be found by generating a larger simulation database.

From equation (3.21), it is clear that there are four scaling parameters (*i.e.* $\tilde{J}_0$, T_e, ω_{rf} and n_{sm}) which can control the stochastic heating.

$$H = \frac{\tilde{J}_0^2}{\pi e \varepsilon_0 T_e \omega_{rf}^2 n_{sm}} \tag{3.21}$$

There are different ways to scale these parameters. We will discuss three approaches for the given applied RF frequency of $f_{rf} = 27.12$ MHz in our simulations to investigate the validation of analytical models. Here the PIC simulation is conducted for current-driven argon discharges in which both electrons and ions were moved by the usual PIC method. Plasma is considered collisionless here so there are no electron-neutral and ion-neutral collisions etc. The ions and electrons are loaded initially and evolve with time until the self-consistent steady-state configuration is achieved. The basic input parameters for these PIC simulations are: electron temperature $T_e \sim 2.5$ eV, ion temperature $T_i \sim 0.03$ eV and system length $l \sim 0.04 - 0.1$ m.

The first approach : In the first approach benchmarking of the analytical model is the same as that used by Kawamura *et al.* [1] where H is calculated by varying $\tilde{J}_0$ and n_{sm} simultaneously. The value of $H \approx 0.6 - 18$ for a current drive amplitude of $\tilde{J}_0 = 5 - 185$ A/m^2 and the corresponding densities are $n_{sm} \approx 2 \times 10^{14} - 6 \times 10^{15}$ m^{-3}. The electron thermal velocity, $\bar{v}_e \approx 1.058 \times 10^6$ m/s, stays approximately constant.

Figure (3.4) shows the averaged ion and snapshots of the electron density profile in the collisionless case. The ion sheath density $n_{sh}(x)$ decreases monotonically from a maximum density at the ion sheath boundary to a minimum of $n_w = 2.62 \times 10^{14}$ m^{-3} at the wall. Here argon gas is used at $\tilde{J}_0 = 110$ A/m^2 *i.e.* $H = 7.57$. In figure (3.4), *plasma wave* propagation can also be observed. These waves are the result of the progressive failure of quasi-neutrality at the electron sheath edge and are more visible during the expansion of the sheath towards the bulk plasma. This phenomena will be discussed in the next chapter.

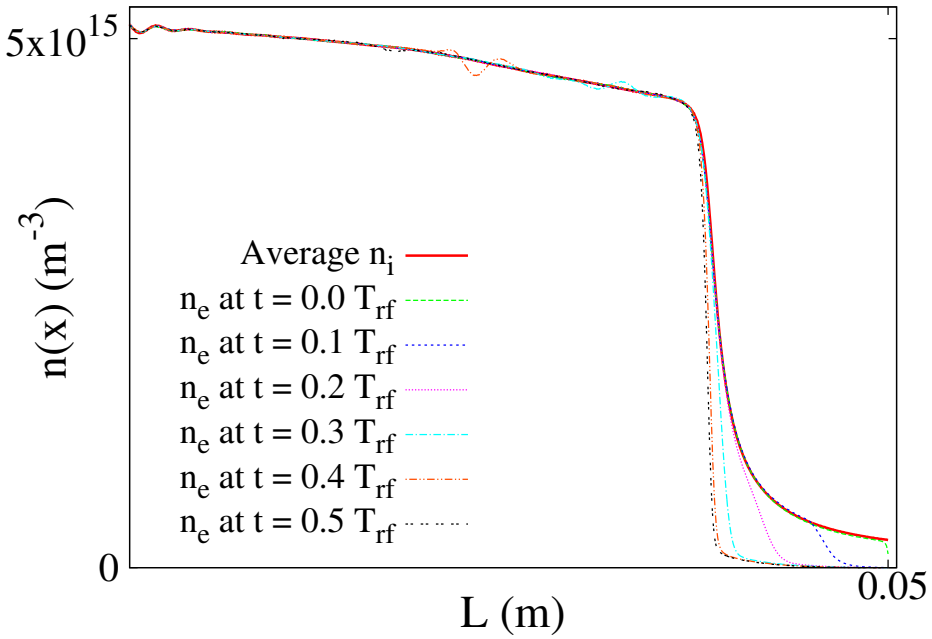

Figure 3.4: *Snapshots of PIC simulation ion and electron density profiles for the collisionless case. The solid line represents the average ion density and the electron density is represented by dashed lines during different times of an RF period i.e.* T_{rf}. *Conditions : argon gas,* $\tilde{J}_0 = 110\ A/m^2$, $f_{rf} = 27.12\ MHz$, $H = 7.57$, $T_e = 2.5\ eV$, $T_i = 0.03\ eV$.

The power deposition calculated by PIC simulation needs to be compared with that predicted by the models of Lieberman [30] and Kaganovich *et al.* [91]. The average power per unit area deposited into the plasma by the oscillating sheath can be calculated directly from PIC simulation by

$$S_{stoc} = \frac{1}{T}\int_0^{s_m}\int_0^{T} J_e\, E\, dt\, dx\,, \tag{3.22}$$

where E is the electric field and J_e is the electron current density.

Figure (3.5) show the time-averaged local heating rate $\langle J_e.E\rangle$ for given values of H between 0.63 to 18.14. Here the results are plotted in two separate graphs, for lower values of H ($H < 5$) *i.e.* case (a) in figure (3.5) and for higher values

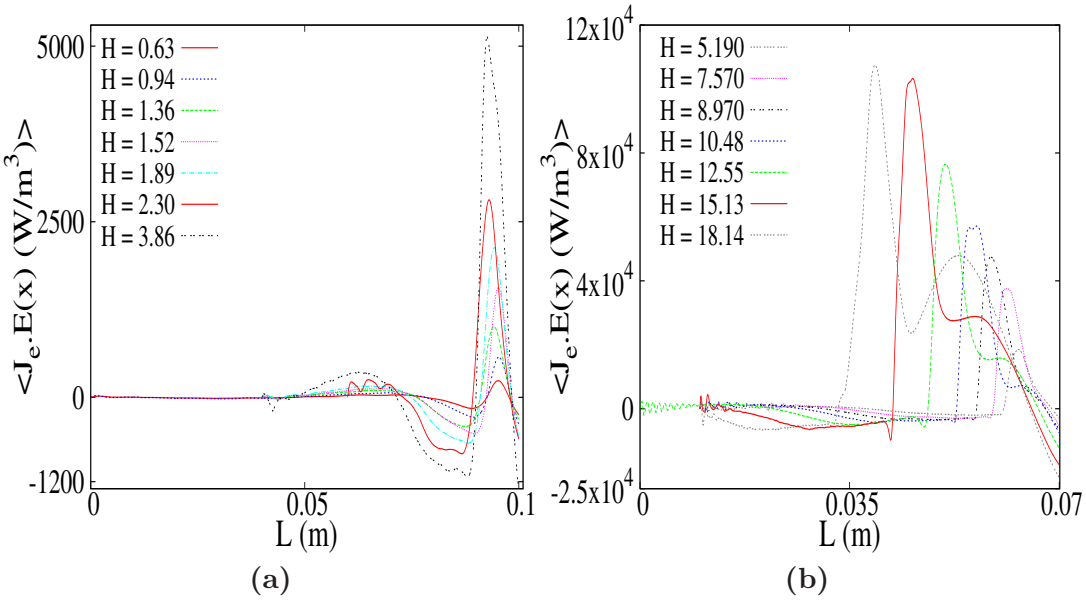

Figure 3.5: *Figure shows the PIC simulation results for* $\langle J_e.E \rangle$ *for the self-consistent mobile-ion argon discharges. (a)* $H = 0.63 - 3.86$ *(b)* $H = 5.19 - 18.14$

of H ($H > 5$) *i.e.* case (b) in figure (3.5), for better visualization. Since H increases by increasing $\tilde{J}_0$, the overall heating increases for the higher values of H.

Analytical models do not account for electron loss at the electrode. In order for the comparison of simulations with analytical models, the contribution to the power per unit area by the electrons which are being lost at the electrode has to be excluded. To implement this idea, in simulation the RF current *i.e.* $J(t)$ is set zero in each case. In steady state, the sheath edge is determined and the stochastic heating upto the sheath edge is calculated in each set of simulation. This is the power per unit area by the electrons which are being lost at the electrode and has been excluded in each case here.

Figure (3.6) shows the variation of normalized stochastic heating $G(H) \equiv S_{stoc}/S_{stocL}$, for the two cases of included and excluded electron loss at an elec-

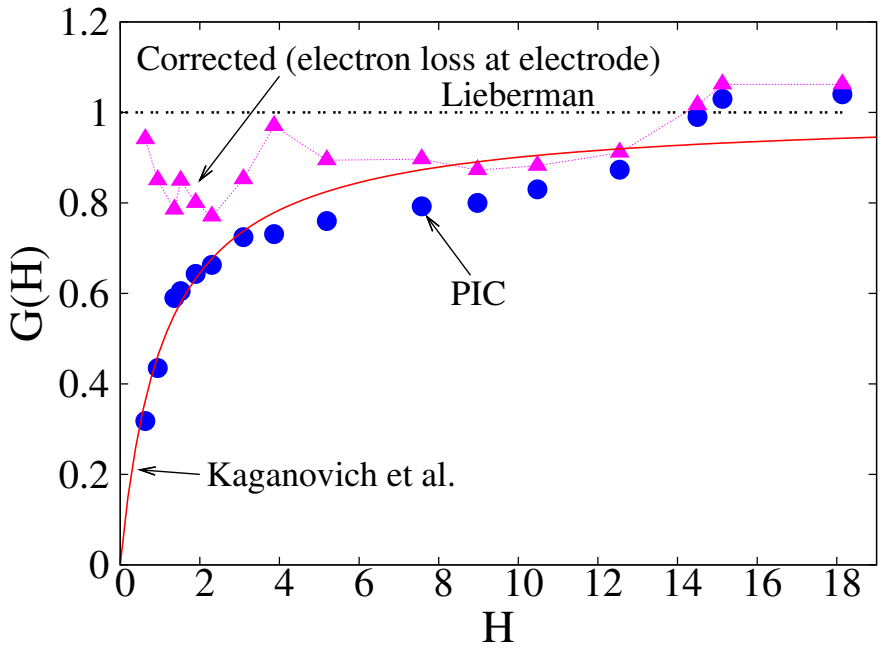

Figure 3.6: *Normalized stochastic heating $G(H) \equiv S_{stoc}/S_{stocL}$ from the PIC simulation without correction (circles), with correction (triangles) and the Kaganovich et al. model (solid line). The Lieberman hard wall limit also shown (dashed line).*

trode, with respect to H. The PIC simulation (circles) is compared with the result from Kaganovich *et al.* [91] $G_K(H)$ given in equation (3.17) and the Lieberman model [30] having $G_L = 1$ (dashed line). It is clear from the figure that the uncorrected PIC data, which includes the electron loss at an electrode, fairly agrees with the Kaganovich *et al.* model for the large range of H. On the other hand the corrected PIC data (dotted line with triangles), which excludes the electron loss at the electrode, more closely agree with the Lieberman model especially for lower values of H. Again for higher values of $H > 10$, the stochastic heating for both cases is not significantly different.

The second approach: In the second approach the stochastic heating is investigated by keeping the density (n_{sm}) constant and varying the current density amplitude $\tilde{J}_0$. Here by keeping T_e, n_{sm} and ω_{rf} constant and varying the

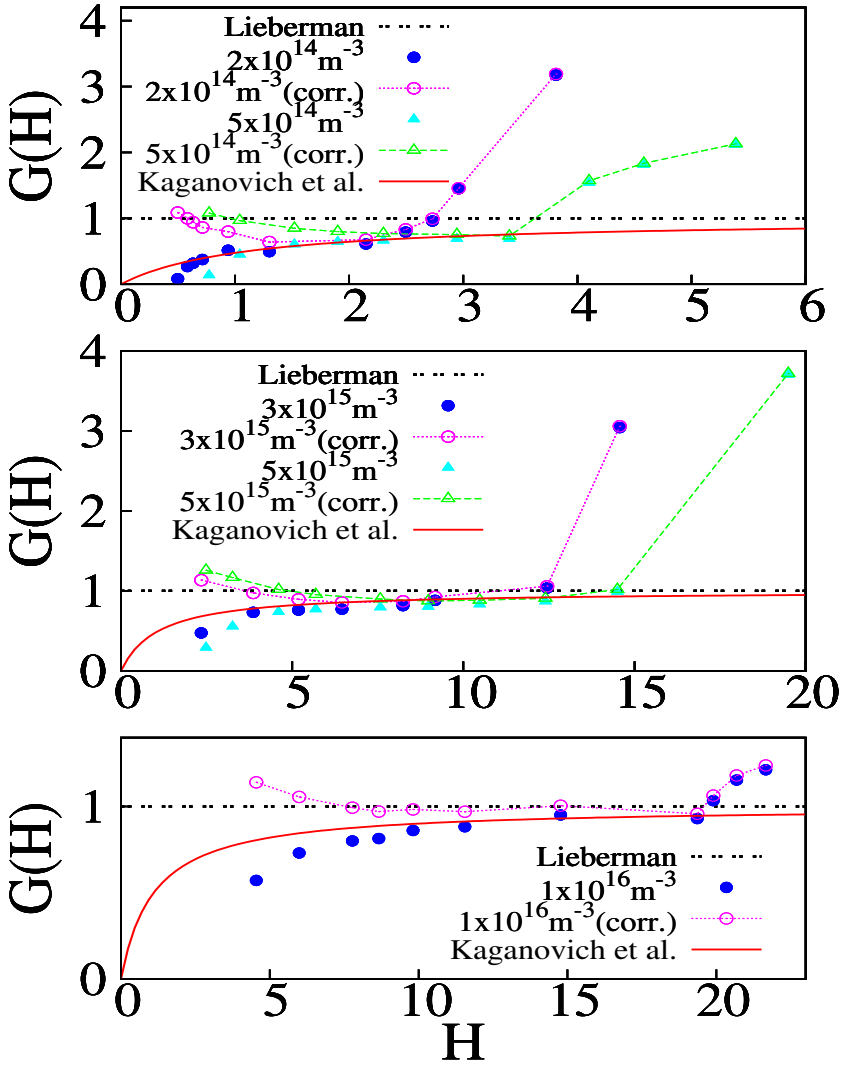

Figure 3.7: *Normalized stochastic heating $G(H) \equiv S_{stoc}/S_{stocL}$ for a range of different densities from 2×10^{14} m^{-3} to 1×10^{16} m^{-3} from the mobile PIC simulations and the Kaganovich et al. model (solid line). The Lieberman hard wall limit is also shown (dashed line).*

current density amplitude $\tilde{J}_0$ changes the stochastic heating. We have investigated this point for a range of different densities from 2×10^{14} m^{-3} to 1×10^{16} m^{-3}. The electron temperature T_e is 2.5 eV and ion temperature is at nearly

room temperature *i.e.* $T_i = 0.03$ eV. The parameter $\bar{v}_e = 1.058 \times 10^6$ m/s did not vary with $\tilde{J}_0$ and stayed approximately constant.

In figure (3.7), the normalized stochastic heating $G(H) \equiv S_{stoc}/S_{stocL}$ from the mobile-ion PIC simulations for a range of different densities from 2×10^{14} m^{-3} to 1×10^{16} m^{-3} is compared to the Kaganovich *et al.* [91] result for $G_K(H)$ given in equation (3.17). The Lieberman [30] hard wall limit, $G_L(H) = 1$, is also shown (dashed line). As we discussed, the analytic models do not account for electron loss at the electrode so in order for the comparison to be made, the contribution to the power per unit area by the electrons which are being lost at the electrode has to be excluded. In figure (3.7), solid circles and solid triangles show the values of stochastic heating calculated by including the value of electron loss at the electrode. Hollow circles and hollow triangles represents the value of stochastic heating calculated when the value of electron loss at an electrode is excluded.

Figure (3.7) is divided into three different density ranges *i.e.* low densities ($n_{sm} < 1 \times 10^{15}$ m^{-3}), intermediate densities ($1 \times 10^{15} < n_{sm} < 1 \times 10^{16}$ m^{-3}) and high densities ($n_{sm} \geq 1 \times 10^{16}$ m^{-3}). In the case of low densities, for 2×10^{14} m^{-3} and 5×10^{14} m^{-3}, the range in which values of H fairly agree with Kaganovich *et al.* [91] is 0.6 - 2.5 and 1.0 - 3.5 respectively. For $H > 2.5$ and 3.5 the stochastic heating increases rapidly. Similarly, for intermediate densities of 3×10^{15} m^{-3} and 5×10^{15} m^{-3}, the range of H which fairly agree with Kaganovich *et al.* [91] is 4 - 9.18 and 4.2 - 15 respectively. In each case after the upper critical limit of H (in which the analytical model agrees with simulation results) the stochastic heating increases rapidly. Finally for the higher density case *i.e.* 1×10^{16} m^{-3} the range of H which fairly agree with Kaganovich *et al.* [91] model is 6 - 20. Again in this case, after the upper critical limit of H, the stochastic heating increases rapidly.

Based on the above observations, the following conclusions can be made:

1. At constant density the simulation results agree with the Kaganovich *et al.* [91] model in a certain range of H.

2. For lower density, the Kaganovich *et al.* [91] model agrees with simulation results for lower values of H. Similarly, for intermediate and higher density, the Kaganovich *et al.* [91] model agrees with simulation results for intermediate and higher values of H respectively.

3. The maximum range of H for which the simulation results fairly agree with the Kaganovich *et al.* [91] model is for densities 5×10^{15} m^{-3} and 1×10^{16} m^{-3}.

4. In each case, for the lower critical limit of H (in which the simulation agrees with the analytical model), the value of stochastic heating calculated by considering the value of electron loss at an electrode is closer to Lieberman's [30] model than to the Kaganovich *et al.* [91] model. It is clear that for values of H near to the lower critical limit of H the correction by electron loss at an electrode is significant, but for values of H near to the higher critical limit of H, this correction is not significant.

Now we will discuss one specific case of 3×10^{15} m^{-3} in detail. Figure (3.8) shows the time-averaged local heating rate $\langle J_e.E \rangle$. For $\tilde{J}_0 = 45 - 102$ A/m^2, values of H vary between 2.34 and 14.57. This figure shows that when the value of H changes from 9.18 to 14.57, stochastic heating increases rapidly. So here 9.18 is the upper critical limit of H.

Figure (3.9) shows the spatiotemporal profile of full $J_e.E$. Here for lower values of H, the stochastic heating phenomenon occurs near the sheath edge. While increasing $\tilde{J}_0$ *i.e.* H, the sheath width increases and the region near the sheath edge which shows stochastic heating broadens. However there is a

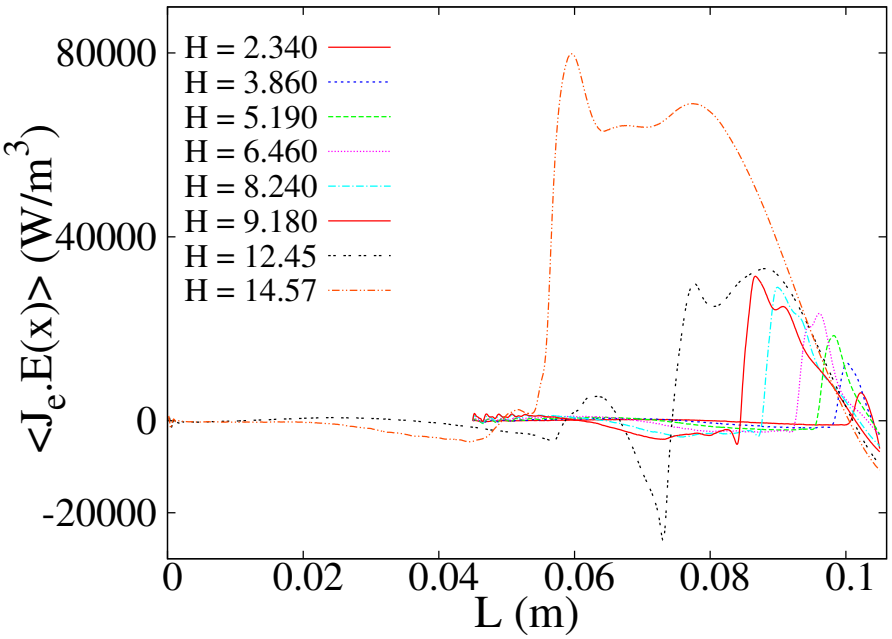

Figure 3.8: *PIC simulation results for* $\langle J_e.E \rangle$ *for the self-consistent mobile-ion argon discharges for density* $3 \times 10^{15}\ m^{-3}$.

transition when H goes from 9.18 to 12.31 and a burst in stochastic heating is observed.

Let us investigate the reason for this rapid increase in stochastic heating above a critical limit of H. Figure (3.10) shows the trajectory of ions in velocity phase space for the case of $\tilde{J}_0 = 98$ A/m^2. Here the positive velocity indicates direction towards the sheath (or electrode) and a negative velocity indicates direction towards the bulk plasma *i.e.* opposite to the sheath. The ion motion is collisionless within the sheath and ions are accelerated by the sheath electric field, a basic assumption of all analytical models. In simulation, the trajectory of a few thousand ions are saved, out of which few ion trajectories show that ions are reflected back to the bulk plasma from near the sheath edge. In figure (3.10), case (a) shows that ion propagate towards the sheath without any deflection in bulk plasma, enter inside the sheath and finally hit the electrode. The majority

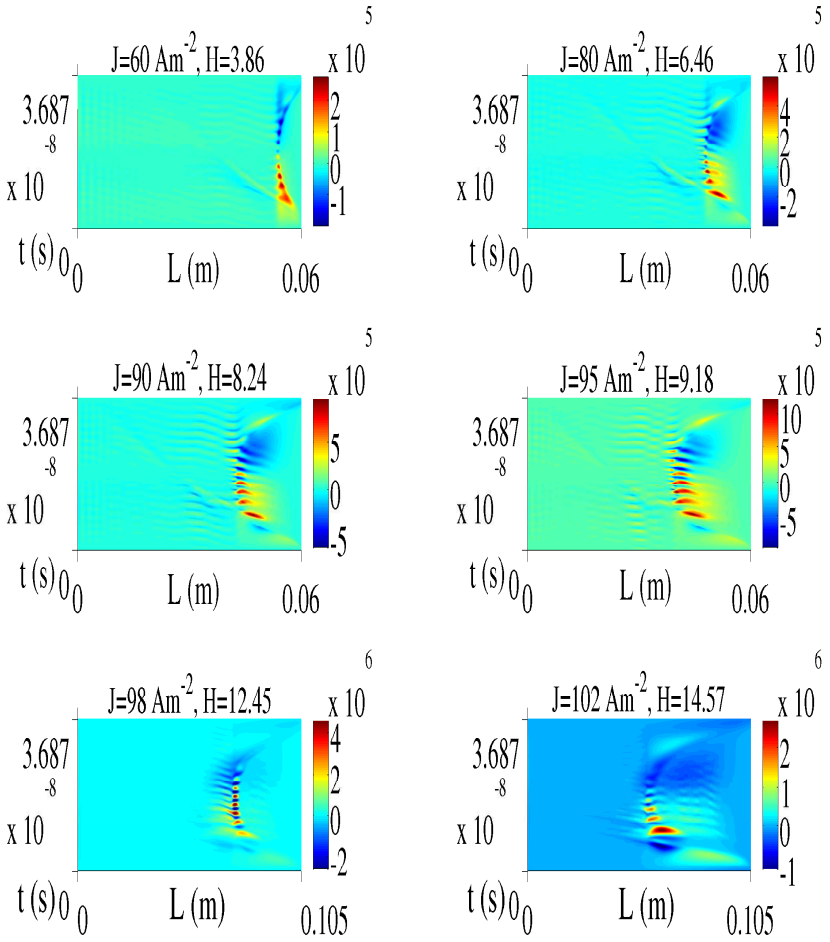

Figure 3.9: *Spatiotemporal profile of $J_e.E$ for density 3×10^{15} m^{-3}.*

of ions in simulation behave like this. Case (b), (e), (g) and (i) show the reflection of ions from near the sheath region. These cases indicate that ions slow down while approaching towards sheath region, stop for a while (trajectory is flat at edge) and finally reflect back towards the bulk plasma. However, case (e) and (i) indicate that ions move outside the simulation region and case (b) and (g) show that ions remain in the simulation region after reflection from the sheath

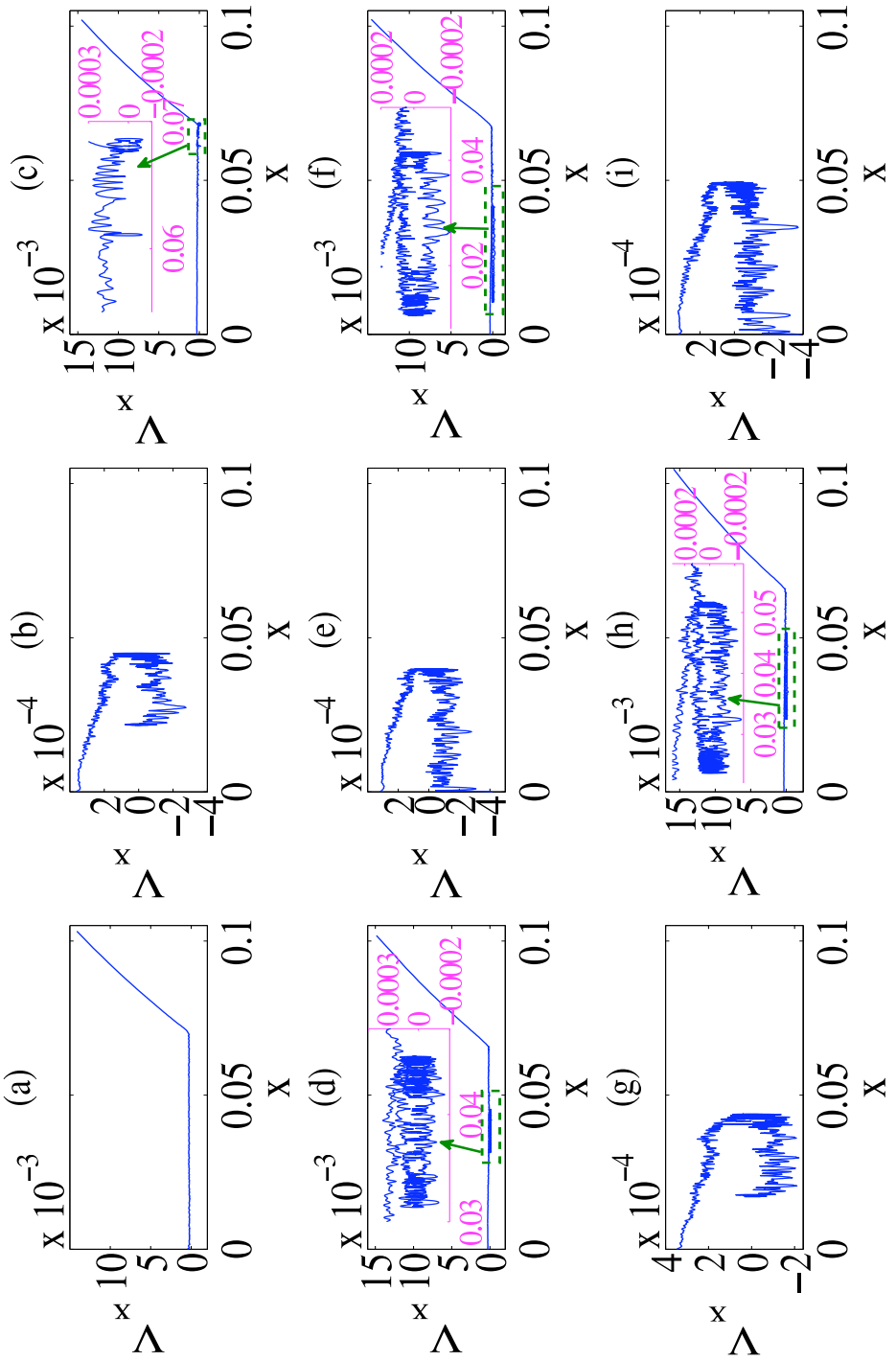

Figure 3.10: *Trajectories of ions in velocity phase space. Conditions: argon gas,* $\tilde{J}_0 = 98\ A/m^2$, $T_e = 2.5\ eV$, $f_{rf} = 27.12\ MHz$.

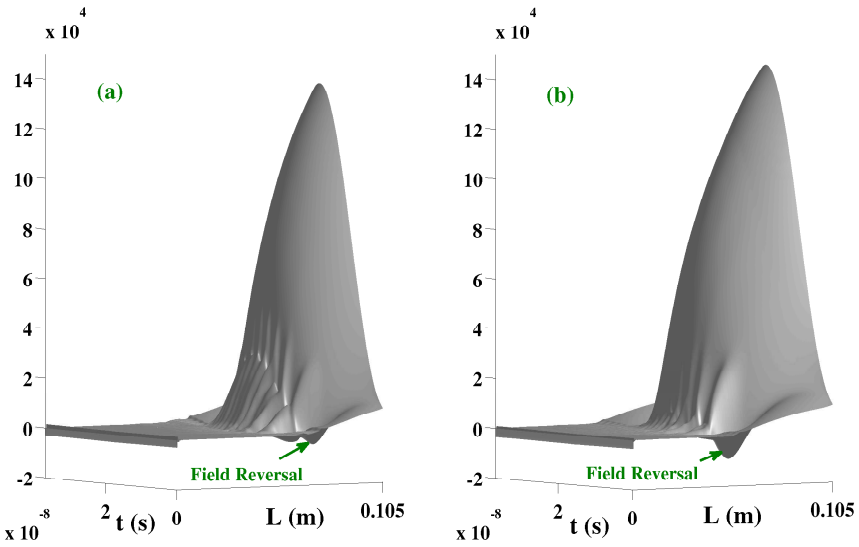

Figure 3.11: *Spatiotemporal profile of electric field. (a) For* $\tilde{J}_0 = 98\ A/m^2$ *(b) For* $\tilde{J}_0 = 102\ A/m^2$. *Conditions: argon gas,* $T_e = 2.5\ eV$, $T_i = 0.03\ eV$, $f_{rf} = 27.12$ *MHz.*

region. Case (c) shows that ion slow down near the sheath region, the velocity is negative for a while and after that it is accelerated inside the sheath and finally hits the electrode. Case (d), (f) and (h) demonstrate that ions reflect back from near the sheath region. After travelling a certain distance inside the bulk plasma (opposite to sheath), the velocity becomes positive and it again moves towards the sheath and finally accelerates and hits the electrode. It is to be noted that the distance travelled inside the bulk plasma after reflection is different in these three cases. The only reason behind the ion reflection from near sheath region is the presence of strong field reversal during the sheath expansion. Figure (3.11) shows the spatiotemporal profile of the electric field for $\tilde{J}_0 = 98$ A/m^2 and $\tilde{J}_0 = 102$ A/m^2. Here because of ion reflection from near sheath region, there is a density jump in bulk plasma from 3×10^{15} m^{-3} to 5.2×10^{15} m^{-3} and 5.7×10^{15} m^{-3} for the case of $\tilde{J}_0 = 98$ A/m^2 and $\tilde{J}_0 = 102$ A/m^2 respectively. Figure (3.12)

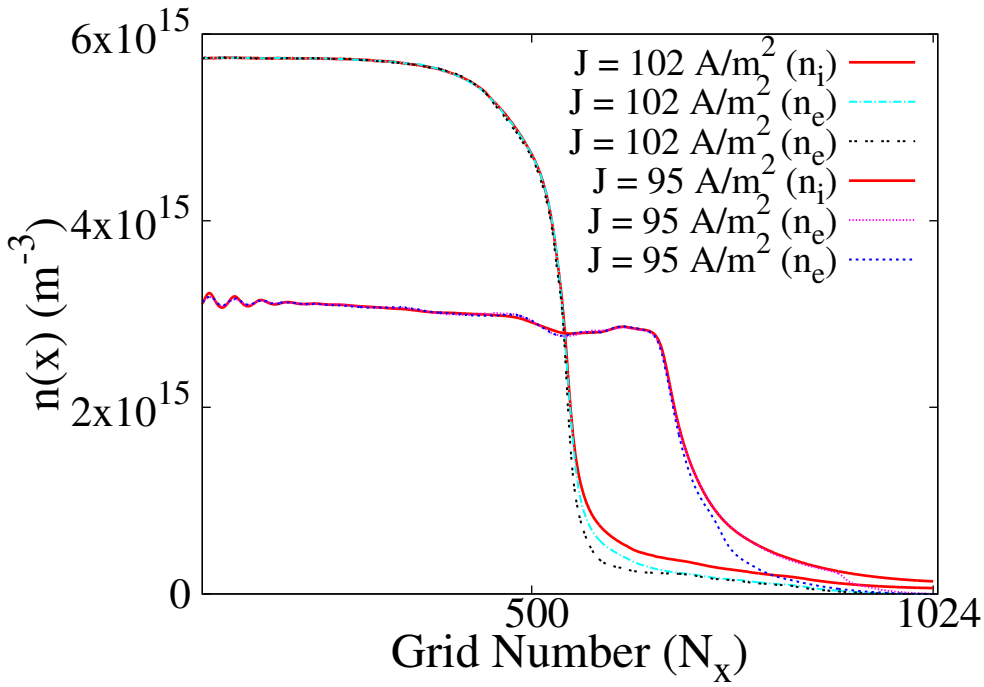

Figure 3.12: *Ion and electron density profile for* $\tilde{J}_0 = 95\ A/m^2$ *and* $\tilde{J}_0 = 102\ A/m^2$ *at density* $3 \times 10^{15}\ m^{-3}$ *. Conditions: argon gas,* $T_e = 2.5\ eV$*,* $T_i = 0.03\ eV$*,* $f_{rf} = 27.12\ MHz$*.*

shows the time average ion and snapshots of electron density profile for $\tilde{J}_0 = 95$ A/m^2 and $\tilde{J}_0 = 102$ A/m^2 at density $3{\times}10^{15}$ m^{-3}. It is clear from this figure that the density jumps from 3×10^{15} m^{-3} to 5.7×10^{15} m^{-3} when $\tilde{J}_0$ varies from 95 A/m^2 to 102 A/m^2. Equation (3.20) shows that stochastic heating depends on density. However this density is either considered as bulk density or density at the ion sheath-plasma boundary. The density distribution inside the simulation region drastically changed for these two cases. Calculating ion density at sheath edge by knowing the n_w (ion density at the electrode) is 2.3844×10^{15} m^{-3} and 2.2077×10^{15} m^{-3} for $\tilde{J}_0 = 98$ A/m^2 and $\tilde{J}_0 = 102$ A/m^2 respectively. For $\tilde{J}_0 = 98$ A/m^2 the analytical and simulation stochastic heating is $S_{stocL} = 554.59$ W/m^2 and $S_{stoc} = 573.78$ W/m^2 respectively. Similarly, for $\tilde{J}_0 = 102$

A/m^2 the analytical and simulation stochastic heating is $S_{stocL} = 759.19$ W/m^2 and $S_{stoc} = 2310.4$ W/m^2 respectively. On the other hand, stochastic heating calculated by considering bulk density, for $\tilde{J}_0 = 98$ A/m^2 and $\tilde{J}_0 = 102$ A/m^2 the analytical stochastic heating is $S_{stocL} = 121.22$ W/m^2 and $S_{stocL} = 115.1$ W/m^2 respectively. These results are tabulated in table (3.1). Here the heating

Table 3.1: *Stochastic heating (both analytical and simulation) for the case of* $\tilde{J}_0 = 98$ A/m^2 *and* 102 A/m^2.

$\tilde{J}_0$	$(S_{stoc})_{analytical}$ (ion sheath edge density)	$(S_{stoc})_{analytical}$ (bulk density)	$(S_{stoc})_{simulation}$
98 A/m^2	554.59 W/m^2	121.22 W/m^2	573.78 W/m^2
102 A/m^2	759.19 W/m^2	115.1 W/m^2	2310.4 W/m^2

predicted by analytical model is significantly less than the heating calculated by PIC simulation because of the density jump inside the bulk plasma. Normally the analytical stochastic heating does not vary much either taking ion density from the bulk plasma or at the ion-sheath edge. Here, due to a density jump inside the bulk plasma the amplitude of the bulk electron oscillation velocity ($u_b = \tilde{J}_0/en_0$) and H drops significantly, as a result analytical heating is much less. This indicates that the electron dynamics of the heating mechanism is different for these cases where strong field reversal region is present and ion reflection phenomenon occurs from near sheath edge. So the existing analytical models are not applicable here.

All analytical models make a basic assumption that ion motion within the sheath is collisionless and ions are accelerated by the sheath electric field. We have observed in simulation cases where the burst in heating is observed, the time averaged ion current at the electrode also drops significantly. Figure (3.13)

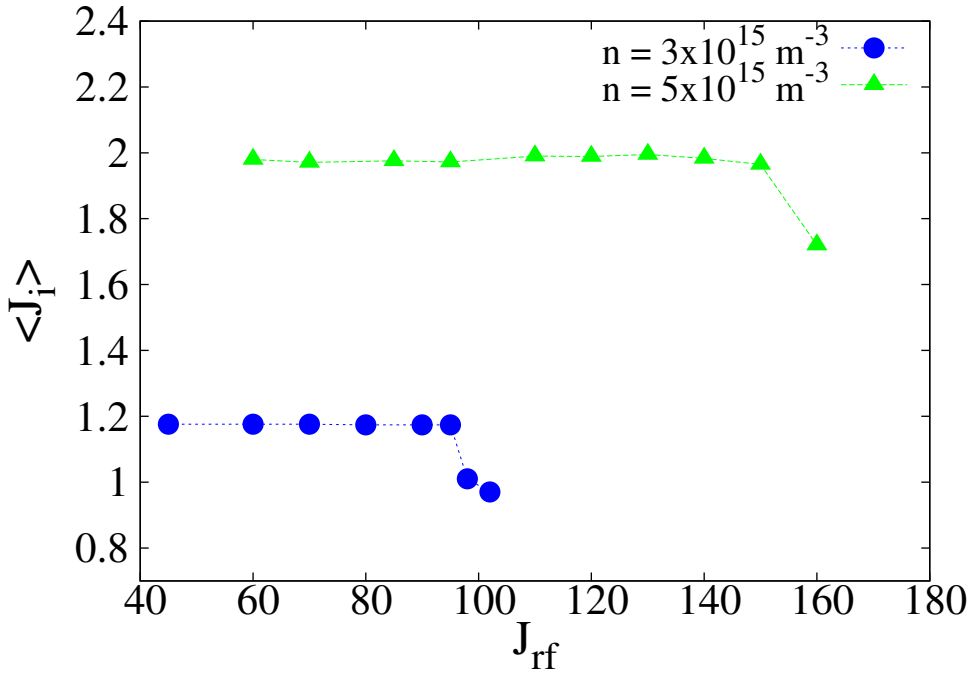

Figure 3.13: *Time average ion current at the electrode for densities* 3×10^{15} m^{-3} *and* 5×10^{15} m^{-3}. *Conditions: argon gas,* $T_e = 2.5$ eV, $T_i = 0.03$ eV, $f_{rf} = 27.12$ MHz.

shows that the average ion current ($< J_i >$) at the electrode for densities 3×10^{15} m^{-3} and 5×10^{15} m^{-3} drops down nearly 20% and 15% respectively for the cases ($\tilde{J}_0 = 98$ and 102 $\mathrm{A/m^2}$ for 3×10^{15} m^{-3} and $\tilde{J}_0 = 160$ $\mathrm{A/m^2}$ for 5×10^{15} m^{-3}) where ion reflection phenomenon from near sheath region is observed. The same trend is also observed for other density cases.

The third approach: In the second approach, it is observed that the maximum range of **H** for which the simulation results follow the Kaganovich *et al.* [91] model is for densities in the range of 5×10^{15} m^{-3} to 1×10^{16} m^{-3}. So in the present approach we studied the effect of electron temperature T_e on stochastic heating at a density of 5×10^{15} m^{-3}. The input parameters are: $\tilde{J}_0 =$ 130 $\mathrm{A/m^2}$, $f_{rf} = 27.12$ MHz and $T_i = 0.03$ eV. The electron temperature varies

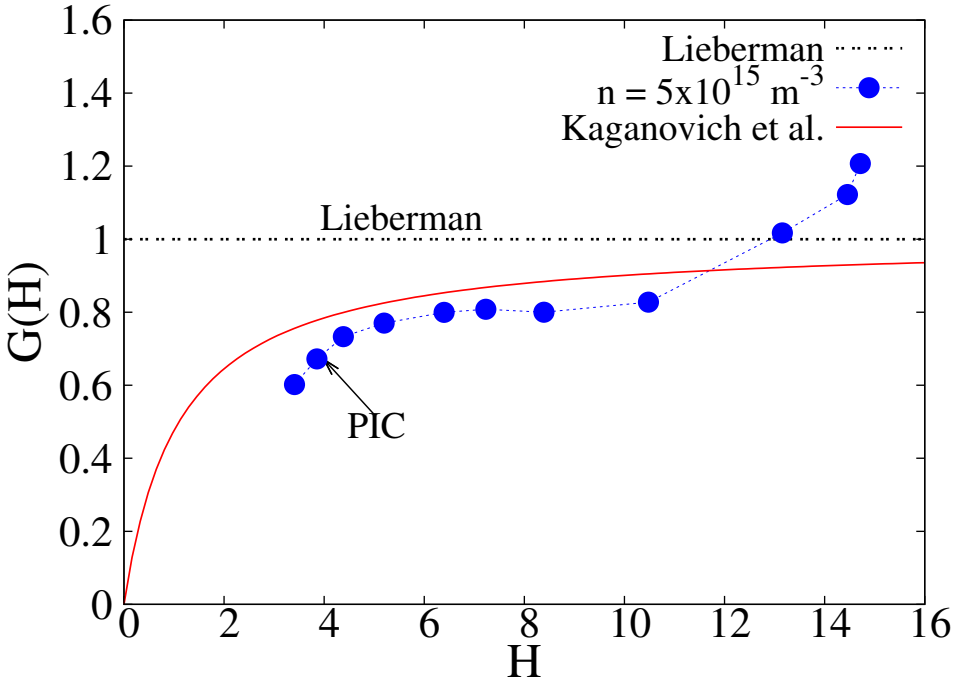

Figure 3.14: *Normalized stochastic heating S_{stoc}/S_{stocL} scaling with electron temperature T_e. Conditions: argon gas, $\tilde{J}_0 = 130\ A/m^2$, $T_e = 1.7 - 10\ eV$, $T_i = 0.03\ eV$, $f_{rf} = 27.12\ MHz$.*

from 1.7 eV to 10 eV. Equation (3.21) shows that H decreases by increasing T_e. The change in T_e signifies the change in electron thermal velocity $\bar{v}_e$. Here for T_e varying from 1.7 eV to 10 eV, the corresponding $\bar{v}_e$ varies from 0.8726×10^6 m/s to 2.116×10^6 m/s.

Figure (3.14) shows the plot of normalized stochastic heating *i.e.* S_{stoc}/S_{stocL} versus H. We can make the following conclusions from this figure:

1. It is clear from the figure that the range of values of H which fairly agree with the Kaganovich *et al.* [91] model is from 4 to 13.5. In the *second approach* the range of H which follows the Kaganovich *et al.* [91] model for the density 5×10^{15} m^{-3} is 4.2 to 15. So the range of H is roughly the same and does not change by varying the electron temperature T_e while

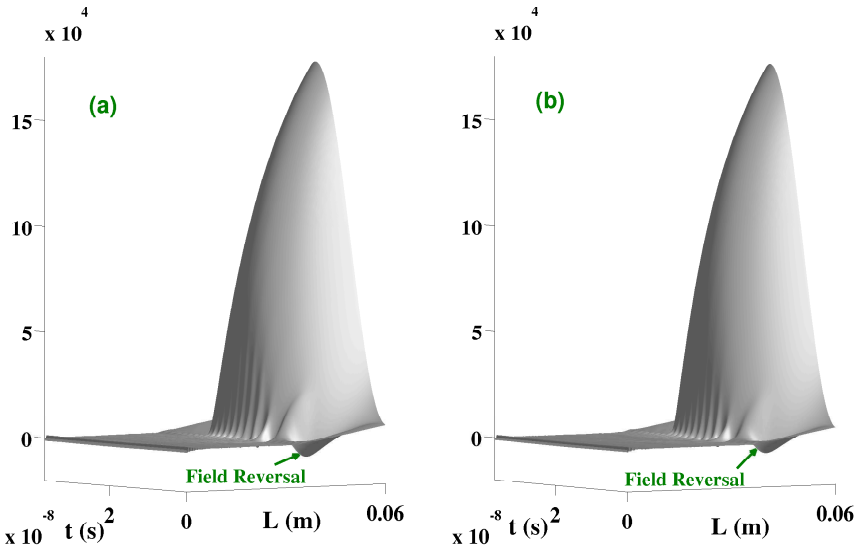

Figure 3.15: *Spatiotemporal profile of electric field (surface plot). (a) For* $T_e = 1.8$ *eV (b) For* $T_e = 2.0$ *eV. Conditions: argon gas,* $\tilde{J}_0 = 130$ A/m^2, *density* $= 5 \times 10^{15}$ m^{-3}, $T_i = 0.03$ eV, $f_{rf} = 27.12$ MHz.

keeping the other parameters constant (*present approach*) or by varying $\tilde{J}_0$ while keeping the other parameters constant (*second approach*).

2. For higher values of **H** ($H > 14$) or lower values of T_e ($T_e < 2$ eV) the stochastic heating increases rapidly.

The reason for this burst of stochastic heating after a critical limit of H is the same as was explained in the *second approach*. Figure (3.15) shows the spatio temporal profile of electric field for $T_e = 1.8$ eV and 2.0 eV which corresponds to $H = 14.46$ and 13.16 respectively. This figure clearly indicates the presence of field reversal at the time of sheath expansion, near the sheath region. The signature of ion reflection from near sheath region is also observed for these cases.

3.6 Frequency Scaling

In a CCP reactor, processes can be optimized simply by varying the frequency [145–147]. A frequency increase improves plasma-generation efficiency (*i.e.* the electron density obtained for a given input power) in CCPs [6, 148–150]. A commonly used frequency is 13.56 MHz for a variety of thin film deposition and etching applications. Typically, high plasma densities (or ion fluxes) are required to increase deposition and etch rates and low ion energies are desired to minimize film damage. Therefore, higher deposition and etch rates with improved anisotropy, uniformity and film quality are needed.

Plasma density and ion flux in a CCP reactor increase with applied *RF* voltage, at a fixed frequency. However, the gain in flux is accompanied by an increase in the plasma potential and ion energy, restricting the usefulness of the 13.56 MHz CCP reactor. The applied *RF* frequency (ω_{rf}) in CCPs is greater than the *ion plasma frequency* (ω_{pi}) and less than the *electron plasma frequency* (ω_{pe}), *i.e.* $\omega_{pi} < \omega_{rf} < \omega_{pe}$. The effect of frequency variation on stochastic heating (in a collisionless plasma) in single frequency capacitively coupled argon discharges is investigated here. It is to be noted that at low *RF* frequencies (when ω_{rf} approach towards ω_{pi}), the ions respond to the time-varying fields within the sheath, rather than to their average value. In this case the existing analytical models for stochastic heating (*e.g.* Lieberman [30] and Kaganovich [34]) are not valid. From equation (3.21), it is clear that H can be kept constant by different methods, two approaches for which are discuss here:

1. by varying the current density amplitude $\tilde{J}_0$ and density n_{sm} simultaneously.

2. by varying only the current density amplitude $\tilde{J}_0$ at constant density n_{sm}.

PIC simulations were conducted for current-driven argon discharges. The plasma

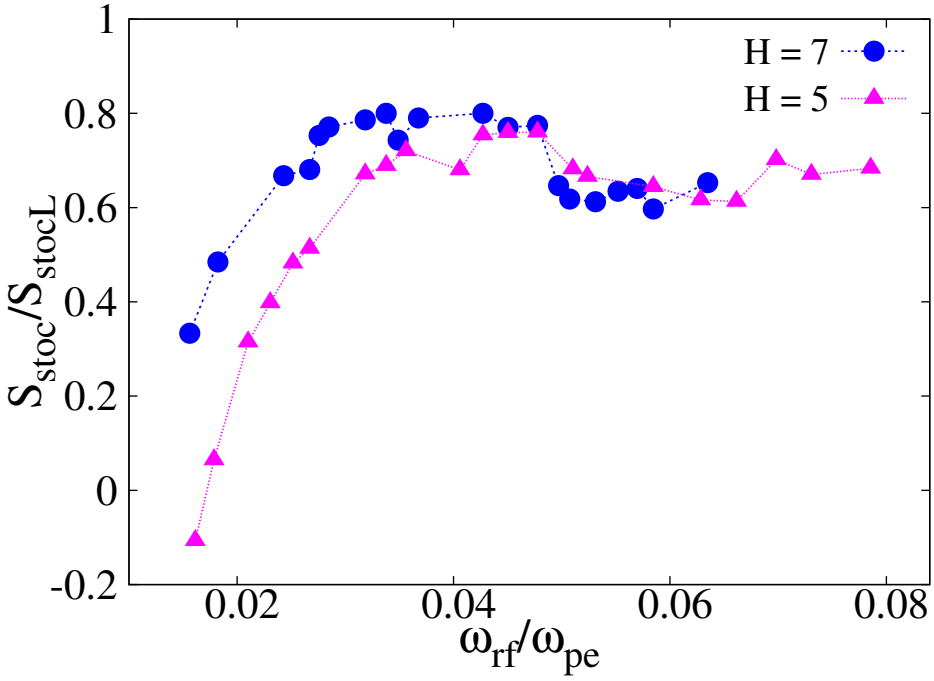

Figure 3.16: *Normalized stochastic heating S_{stoc}/S_{stocL} for two different constant* ***H*** *i.e.* 5 *(solid triangles) and* 7 *(solid circles).*

is considered collisionless here (*i.e.* no electron-neutral and ion-neutral collisions etc.). The ions and electrons are loaded initially and the simulation is run until the steady-state configuration is achieved.

***The first approach*:** Firstly, the average power per unit area scaling with frequency for a constant H, will be discussed. For this case H is kept constant by varying the current density amplitude $\tilde{J}_0$ and density n_{sm} simultaneously.

Figure (3.16) represents the normalized stochastic heating S_{stoc}/S_{stocL} scaling with frequency ω_{rf}/ω_{pe} for two different values of H *i.e.* 5 and 7. For $H = 5$ the density is varied from $\sim 2\times10^{14}$ m^{-3} to 5×10^{16} m^{-3}. The applied frequency is $f_{rf} \approx 2 - 158$ MHz and the corresponding current density amplitude is $\tilde{J}_0 \approx 1.36 - 1653.74$ A/m^2. Higher frequencies are computationally expensive to simulate because of the smaller simulation time-step needed. Here the ion plasma

frequency f_{pi} varies from 0.469 MHz to 7.414 MHz and the electron plasma frequency f_{pe} goes from 0.127 GHz to 2.008 GHz. For $H = 7$ the density is varied from 2×10^{14} m^{-3} to 1×10^{17} m^{-3}. The applied frequency is $f_{rf} \approx 2 - 180$ MHz and the corresponding current density amplitude is $\tilde{J}_0 \approx 1.56 - 3162$ A/m^2. The ion plasma frequency f_{pi} varies from 0.469 MHz to 10.485 MHz and the electron plasma frequency f_{pe} varies from 0.127 GHz to 2.839 GHz. These results are tabulated in table (3.2). From figure (3.16), it is clear that for $H = 5$ the

Table 3.2: *The first approach: Frequency scaling for $H = 5$ and 7.*

H	**n ($\mathbf{m^{-3}}$)**	$\tilde{J}_0$ **(A/m^2)**	$\mathbf{f}_{rf}$ **(MHz)**	$\mathbf{f}_{pi}$ **(MHz)**	$\mathbf{f}_{pe}$ **(GHz)**
5	2×10^{14} - 5×10^{16}	1.36 - 1653.74	2 - 158	0.469-7.414	0.127-2.008
7	2×10^{14} - 1×10^{17}	1.56 - 3162	2 - 180	0.469-10.485	0.127-2.839

normalized stochastic heating is almost constant from $\omega_{rf}/\omega_{pe} \sim 0.032 - 0.079$. Heating decreases rapidly for $\omega_{rf}/\omega_{pe} < 0.032$. So when $f_{rf}/f_{pi} < 7$, stochastic heating rapidly decreases. The negative heating shown at low ω_{rf}/ω_{pe} is due to the large number of electrons being lost to the electrode, this results in a loss of power that is greater than the stochastic heating at the sheath edge. For the case of $H = 7$, normalized stochastic heating is almost constant in the range of $\omega_{rf}/\omega_{pe} \sim 0.024 - 0.065$. It promptly decreases for $\omega_{rf}/\omega_{pe} < 0.024$. In this case when $f_{rf}/f_{pi} < 6$, stochastic heating is rapidly decreased. In these cases the contribution to the power per unit area by the electrons which are being lost at the electrode is not excluded.

***The second approach*:** Now consider the second case in which H is kept constant by varying only the current density amplitude $\tilde{J}_0$ at constant density n_{sm}.

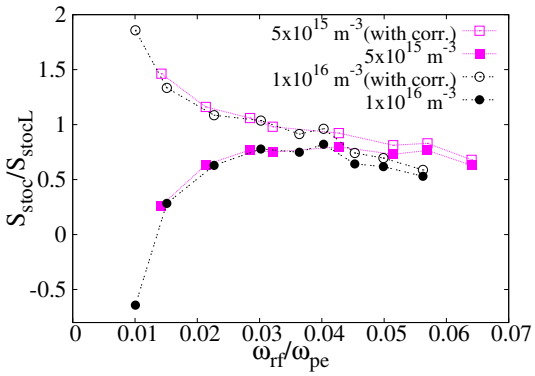

Figure 3.17: *Normalized stochastic heating S_{stoc}/S_{stocL} for $\boldsymbol{H} = 7$ at different densities i.e. 5×10^{15} m^{-3} (solid square) and 1×10^{16} m^{-3} (solid circles). Hollow squares and hollow circles are the corresponding normalized stochastic heating with correction term (electrons that are being lost at an electrode).*

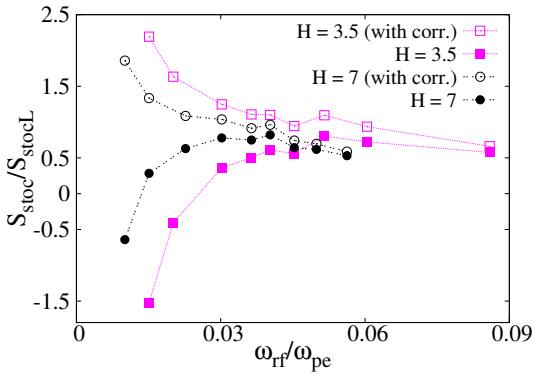

Figure 3.18: *Normalized stochastic heating S_{stoc}/S_{stocL} at density 1×10^{16} m^{-3} for different H i.e. $H = 3.5$ (solid square) and $H = 7$ (solid circles). Hollow squares and hollow circles are the corresponding normalized stochastic heating with a correction term (electrons that are being lost at an electrode).*

It is shown in figure (3.17). In this case the contribution to the power per unit area by the electrons which are being lost at the electrode has been excluded. The applied frequency is $f_{rf} \approx 9 - 40$ MHz and the corresponding current density amplitude is $\tilde{J}_0 \approx 35-160$ A/m^2 at density 5×10^{15} m^{-3} and $f_{rf} \approx 9-51$ MHz and corresponding $\tilde{J}_0 \approx 50-280$ A/m^2 at density 1×10^{16} m^{-3} for $H = 7$. The ion plasma frequency f_{pi} is 2.34455 MHz and the electron plasma frequency f_{pe} is 0.6349 GHz for density 5×10^{15} m^{-3}. For 1×10^{16} m^{-3}, f_{pi} is 3.3157 MHz and f_{pe} is 0.897634 GHz. These results are tabulated in table (3.3). It is clear from figure (3.17) that S_{stoc}/S_{stocL} is almost constant for $\omega_{rf}/\omega_{pe} \approx 0.022-0.065$ at densities of 5×10^{15} m^{-3} (solid square) and $\omega_{rf}/\omega_{pe} \approx 0.023 - 0.058$ at a density of 1×10^{16} m^{-3} (solid circles) for $H = 7$. So density does not greatly affect the range in which the normalized stochastic heating is almost constant.

Table 3.3: *The second approach: Frequency scaling for $H = 7$.*

n ($\mathbf{m^{-3}}$)	$\tilde{J}_0$ ($\mathbf{A/m^2}$)	$\mathbf{f}_{rf}$ (**MHz**)	$\mathbf{f}_{pi}$ (**MHz**)	$\mathbf{f}_{pe}$ (**GHz**)
5×10^{15}	35 - 160	9 - 40	2.34455	0.6349
1×10^{16}	50 - 280	9 - 51	3.3157	0.897634

Similarly for $\omega_{rf}/\omega_{pe} < 0.02$ the normalized stochastic heating decreases rapidly for both cases. Hollow squares (5×10^{15} m^{-3}) and hollow circles (1×10^{15} m^{-3}) show the normalized stochastic heating with a correction term (electrons that are being lost at an electrode). The negative heating (in case of uncorrected data) shown at low ω_{rf}/ω_{pe} is due to the large number of electrons being lost to the electrode, this results in a loss of power that is greater than the stochastic heating at the sheath edge. It is noticeable that the correction term is significant below $\omega_{rf}/\omega_{pe} < 0.03$.

Now look at figure (3.18). Here the normalized stochastic heating S_{stoc}/S_{stocL} varies with ω_{rf}/ω_{pe} for two different values of H *i.e.* 3.5 and 7 at a density of 1×10^{16} m^{-3}. The applied frequency $f_{rf} \approx 13 - 77$ MHz and the corresponding current density amplitude $\tilde{J}_0 \approx 53{-}303$ A/m^2 for $H = 3.5$ and $f_{rf} \sim 9{-}51$ MHz and corresponding $\tilde{J}_0 \sim 50{-}280$ A/m^2 for $H = 7$. These results are tabulated in table (3.4). The figure shows that normalized stochastic heating S_{stoc}/S_{stocL} is nearly constant for $\omega_{rf}/\omega_{pe} \approx 0.035 - 0.086$ for $H = 3.5$. It drops down rapidly for $\omega_{rf}/\omega_{pe} < 0.035$. For $H = 7$ heating S_{stoc}/S_{stocL} is fairly constant in the range of $\omega_{rf}/\omega_{pe} \approx 0.022 - 0.056$. Heating decreases rapidly for $\omega_{rf}/\omega_{pe} < 0.02$. In other words a rough criterion is, normalized stochastic heating decreases rapidly when $f_{rf}/f_{pi} < 8$ for $H = 3.5$ and $f_{rf}/f_{pi} < 6$ for $H = 7$. Hollow squares ($H = 3.5$) and hollow circles ($H = 7$) shows the normalized stochastic

Table 3.4: *The second approach: Frequency scaling for density* 1×10^{16} m^{-3}.

H	$\tilde{J}_0$ **(A/m^2)**	$\mathbf{f}_{rf}$ **(MHz)**	$\mathbf{f}_{pi}$ **(MHz)**	$\mathbf{f}_{pe}$ **(GHz)**
3.5	53 - 303	13 - 77	3.3157	0.897634
7.0	50 - 280	9 - 51	3.3157	0.897634

heating with a correction term (electrons that are being lost at an electrode). Again the negative heating (in case of uncorrected data) shown at low ω_{rf}/ω_{pe} is due to the large number of electrons being lost to the electrode, this results in a loss of power that is greater than the stochastic heating at the sheath edge. It is noticeable that the correction term is significant below $\omega_{rf}/\omega_{pe} < 0.04$ for $H = 3.5$ and $\omega_{rf}/\omega_{pe} < 0.02$ for $H = 7$.

3.7 Summary

Using analytic and self-consistent particle-in-cell models, the electron dynamics inside the sheath region of a single radio frequency capacitive discharge have been investigated in connection with collisionless heating through the Fermi acceleration mechanism. Stochastic heating is controlled mainly by four scaling parameters (*i.e.* $\tilde{J}_0$, T_e, ω_{rf} and n_{sm}). There are different ways of scaling these parameters and three different approaches are discussed here.

In the *first approach* benchmarking of the analytical model is the same as that used by Kawamura *et al.* [1] where H is calculated by varying $\tilde{J}_0$ and n_{sm} simultaneously. However in the simulation of Kawamura *et al.* the number of data points are rather small *i.e.* $H \sim 1.7 - 5.7$. Present simulation results widen the range of H *i.e.* $H \sim 0.6 - 18$ which are in fair agreement with the Kaganovich *et al.* [91] model in this range. Analytical models do not account for

electron loss at the electrode, so in order to compare the simulation results with analytical models, the contribution to the power per unit area by the electrons which are being lost at the electrode is excluded and also plotted in figure (3.6). The results obtained indicate that the simulation data, which excludes the electron loss at an electrode, more closely approach the Lieberman model [30]) especially for lower values of H.

In the *second approach* the stochastic heating is studied by keeping density constant and by varying the current density amplitude $\tilde{J}_0$. The stochastic heating has been investigated for the range of different densities from 2×10^{14} m^{-3} to 1×10^{16} m^{-3}. At constant density the simulation results agree with Kaganovich *et al.* [91] in a certain range of H. In each case after a upper critical limit of H (in which the analytical model agrees with simulation) the stochastic heating increases rapidly. The electron dynamics of the heating mechanism is different for these cases and the existing analytical formulas for stochastic heating calculations need to be improved. Signature of ion reflection from near sheath region is also observed. The presence of strong field reversal (at higher H) near the sheath region at the time of sheath expansion is the reason of ion reflection.

In the *third approach* the effect of electron temperature T_e on stochastic heating for the density 5×10^{15} m^{-3} has been investigated. Here T_e is varied from $1.7-10$ eV. It is observed that H is in fair agreement with the Kaganovich *et al.* [91] model for the range 4 to 13.5, which is roughly the same as that observed for same density in the *second approach*. The presence of field reversal at the time of sheath expansion and signature of ion reflection from near sheath region is also observed above the upper critical limit of H.

The average power per unit area scaling with frequency for a constant H is also investigated here. In the *first approach*, the normalized stochastic heating S_{stoc}/S_{stocL} scaling with frequency ω_{rf}/ω_{pe} for two different values of H *i.e.*

5 and 7 is discussed here. For $H = 5$ the density is varied from $\sim 2 \times 10^{14}$ m^{-3} to 5×10^{16} m^{-3} for the applied frequency $f_{rf} \approx 2 - 158$ MHz and the corresponding current density amplitude is $\tilde{J}_0 \approx 1.36 - 1653.74$ A/m^2. For $H = 7$ the density is varied from 2×10^{14} m^{-3} to 1×10^{17} m^{-3} for the applied frequency $f_{rf} \approx 2 - 180$ MHz and the corresponding current density amplitude is $\tilde{J}_0 \approx 1.56 - 3162$ A/m^2. Results show that the normalized stochastic heating versus ω_{rf}/ω_{pe} is almost constant in the range $\sim 0.032 - 0.079$ for $H = 5$ and $\sim 0.024 - 0.065$ for $H = 7$. So for $H = 5$, when $f_{rf}/f_{pi} < 7$ and for $H = 7$, when $f_{rf}/f_{pi} < 6$ the stochastic heating rapidly decreases. Here the power per unit area by electrons which are being lost at the electrode, is not excluded.

For the *second approach* H is kept constant by varying only $\tilde{J}_0$ at constant density n_{sm}. The normalized stochastic heating S_{stoc}/S_{stocL} is almost constant from $\omega_{rf}/\omega_{pe} \approx 0.022 - 0.065$ for $H = 7$ at a density of 5×10^{15} m^{-3} and $\omega_{rf}/\omega_{pe} \approx 0.023 - 0.058$ at a density of 1×10^{16} m^{-3}. So density change does not affect the result too much. For $\omega_{rf}/\omega_{pe} < 0.02$ the normalized stochastic heating decreases rapidly for both cases. Results for normalized stochastic heating with a correction term (electrons that are being lost at an electrode) are also shown in figure (3.17). On the other hand normalized stochastic heating is nearly constant $\sim 0.035 - 0.086$ for $H = 3.5$ and $\sim 0.022 - 0.056$ for $H = 7$ at density 1×10^{16} m^{-3}. Here $f_{rf} \approx 13 - 77$ MHz for $H = 3.5$ and $f_{rf} \approx 9 - 51$ MHz for $H = 7$. Heating decreases rapidly for $\omega_{rf}/\omega_{pe} < 0.035$ for $H = 3.5$ and $\omega_{rf}/\omega_{pe} < 0.02$ for $H = 7$. So roughly, when $f_{rf}/f_{pi} < 8$ for $H = 3.5$ and $f_{rf}/f_{pi} < 6$ for $H = 7$, the heating decreases rapidly. It is also noticeable that the correction term (electrons that are being lost at electrode) is significant below $\omega_{rf}/\omega_{pe} < 0.04$ for $H = 3.5$ and $\omega_{rf}/\omega_{pe} < 0.02$ for $H = 7$. So the range in which the normalized stochastic heating is almost constant, changes for different **H** at the same density.

Finally, the existence of plasma oscillations near the plasma-sheath interface has been noted. These oscillations occur due to the gradual breaking of quasi-neutrality near the sheath edge, and propagate from the plasma-sheath interface towards the bulk plasma.

CHAPTER 4

Electron Plasma Waves: The Wave Phenomenon in Single Radio Frequency Capacitively Coupled Plasma Discharges

4.1 Introduction

In the previous chapter (figure 3.4) we have discussed evidence of electron plasma wave propagation from the sheath edge towards the bulk plasma. Such oscillations are reported in the literature [58, 59, 151]. However no relevant theory is proposed and detailed analysis of their nature has not yet been given. When the sheath expands quasi-neutrality breaks down due to an overshoot of hot electrons into the bulk plasma. Due to this, electron plasma waves occur in the sheath vicinity. There is a strong interaction between the electrons and the oscillating potential, and on average electrons gain energy through nonlinear wave-particle interactions. Our simulations indicate that these waves might contribute to the heating mechanism. An approach based on quasi-linear the-

ory which attempts to link stochastic heating with collisionless power dissipation through wave-particle interaction has appeared in the literature [152, 153]. There are numerous other attempts found in the literature which link the capacitive collisionless heating effects with acoustic or plasma wave phenomena [42, 55–57], but none of these efforts have yet produced a generally satisfying treatment. However it is possible for the oscillation energy to be transferred to electron thermal energy by Landau damping [39] or a similar mechanism.

In absence of collisions, the wave damp because of Landau damping phenomena [39]. In next section we discuss the concept of Landau damping. We then discuss the wave phenomena in semi-infinite plasma for the collisionless case. Finally, the effect of electron elastic collisions on waves is discussed and the results are summarized.

4.2 Landau Damping

Landau damping may be the most famous mystery of classical plasma physics. This process is the effect of damping (exponential decrease as a function of time) of longitudinal space charge waves in plasma [92, 154]. It occurs because of the energy exchange between particles in the plasma with velocity approximately equal to v_{ph} and a wave with phase velocity $v_{ph} = \omega/k$. Here k is wave vector. There is a strong interaction of electrons with the wave. The wave electric field accelerates the particles having velocities slightly less than v_{ph} to move with the wave phase velocity, while those particles with velocities slightly greater than v_{ph} are decelerated by the wave electric field, losing energy to the wave.

In a collisionless plasma where dissipative mechanisms such as collisions of electrons with heavy particles are absent, the particle velocities are often taken to be close to a Maxwellian distribution. If the distribution function has negative slope, the number of particles having velocities slightly less than v_{ph}

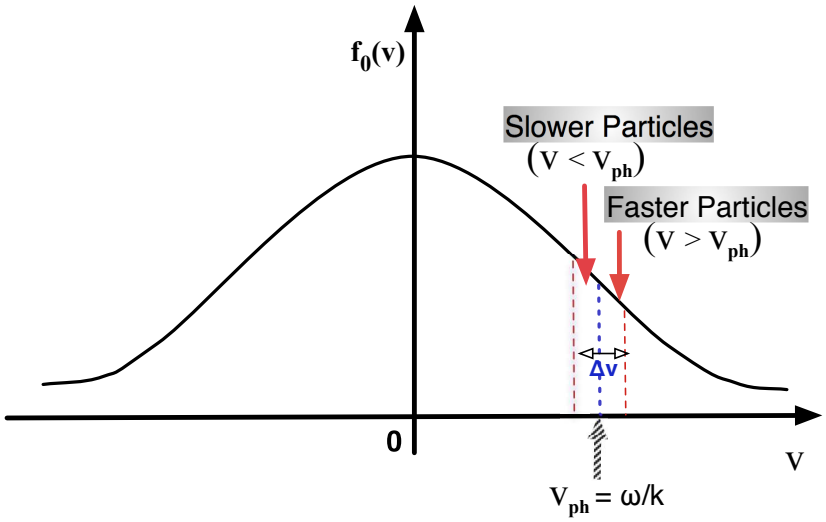

Figure 4.1: *The graph of electron equilibrium distribution function indicating a velocity band Δv around the phase velocity $v_{ph} = \omega/k$. The number of electrons moving faster than v_{ph} are less than the number of electrons moving slower than v_{ph}.*

is greater than the number of particles having velocities slightly greater. As a result the wave is damped, because there are more particles gaining energy from the wave than losing to the wave. On the other hand, if the function has positive slope, the number of particles having velocities slightly less than v_{ph} is smaller than the number of particles having velocities slightly greater. Therefore the wave energy increases, because there are more particles losing energy to the wave than gaining from the wave. In figure (4.1), the damping is negligible for small values of k because the phase velocity v_{ph} lies in the extreme tail of the distribution. However there is a velocity band Δv around $v_{ph} = \omega/k$ when the phase velocity lies close to the maximum slope outside the tail. In this case there are less electrons moving faster than v_{ph} than moving slower than v_{ph}, in Δv. Therefore, a net increase in the electron energy occurs at the cost of wave energy because of the trapping of the electrons in the wave potential troughs. This takes place in the region where $\partial f_0/\partial v_x$ is negative.

The detailed mathematical derivation of Landau damping is available in the literature [92, 154, 155].

4.3 Collisionless Heating - Wave Phenomena

Wave-particle interaction plays an important role in the physics of ionized matter. The nature of this complex interaction in plasmas has predominantly been studied by analytical and simulation methods [156–158]. Recently experimental investigations have also been possible due to advances in optical diagnostics with high temporal resolution [135, 136, 159–162]. As we have discussed in previous chapters, it is very important to understand the mechanism of plasma sustainment in the low pressure regime of capacitively coupled *RF* plasmas (CCPs) for improving the performance and development of many technological applications in the semiconductor industry. It is also clear that electron dynamics govern dissociation, excitation, and ionization processes and is therefore of critical importance in the application and understanding of surface modifications. Present understanding of power deposition in CCPs at low pressure is largely based on theoretical investigation and modelling [30, 34, 42, 43, 60, 163]. Vender and Boswell [59] reported power dissipation through wave-particle interaction in CCPs with the help of particle-in-cell (PIC) simulation. Later Gozadinos *et al.* [58] also reported oscillations near the sheath vicinity in PIC simulation. It is not clear how these oscillations are excited and no relevant theory has yet been put forward. This phenomena is investigated here with the help of self-consistent PIC simulation.

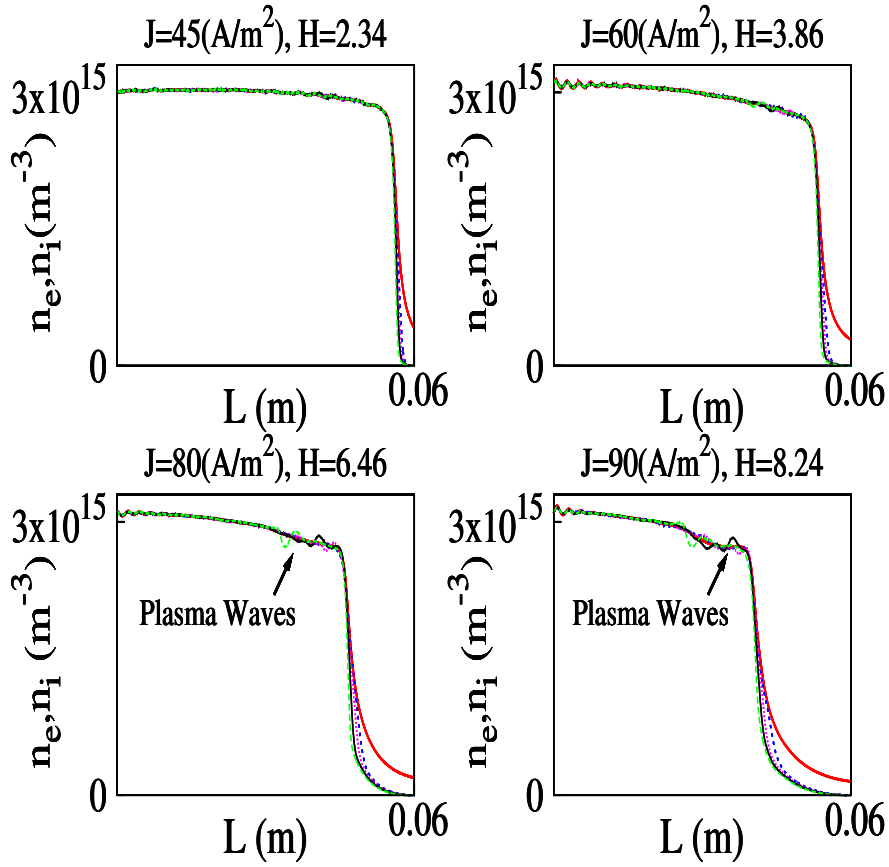

Figure 4.2: *Snapshots of ion and electron density profile in PIC simulation. The solid line (red) represents the average ion density and electron density is represented by lines at different times during an RF period i.e.* $t = 0.244\ T_{rf}$ *(blue),* $t = 0.283\ T_{rf}$ *(magenta),* $t = 0.322\ T_{rf}$ *(black) and* $t = 0.38\ T_{rf}$ *(green). Conditions : argon gas,* $\tilde{J}_0 = 45 - 90\ A/m^2$*,* $f_{rf} = 27.12\ MHz$*,* $H \approx 2.34 - 8.24$*,* $T_e = 2.5\ eV$*,* $T_i = 0.03\ eV$*,* $density = 3.0 \times 10^{15}\ m^{-3}$*.*

4.3.1 Simulation Results of Half-Infinite Plasma

Here we describe PIC simulation results of current-driven argon discharges in which both the electrons and ions were moved by usual PIC methods. These results are for the collisionless case so electron and ion collisions are not included here. The basic input parameters for these PIC simulations are: $f_{rf} = 27.12$

MHz, $l = 0.06 - 0.105$ m, $T_e = 2.5$ eV and T_i is 0.03 eV. The RF current drive amplitude $\tilde{J}_0 = 45 - 90\ A/m^2$ is applied at $density = 3 \times 10^{15}$ m^{-3}.

Figure (4.2) shows the averaged ion and snapshots of electron density profile for $\tilde{J}_0 = 45 - 90$ A/m^2 *i.e.* $H \approx 2.34 - 8.24$, at different times during an RF period. As shown in figure (4.2), the ion density $n_{sh}(x)$ decreases monotonically from maximum density at the ion sheath boundary to a minimum of $n_w = 4.1 \times 10^{14}$ m^{-3}, 2.85×10^{14} m^{-3}, 1.89×10^{14} m^{-3} and 1.488×10^{14} m^{-3} at the wall (electrode) for corresponding $\tilde{J}_0 = 45 - 90$ A/m^2 respectively. Real physical

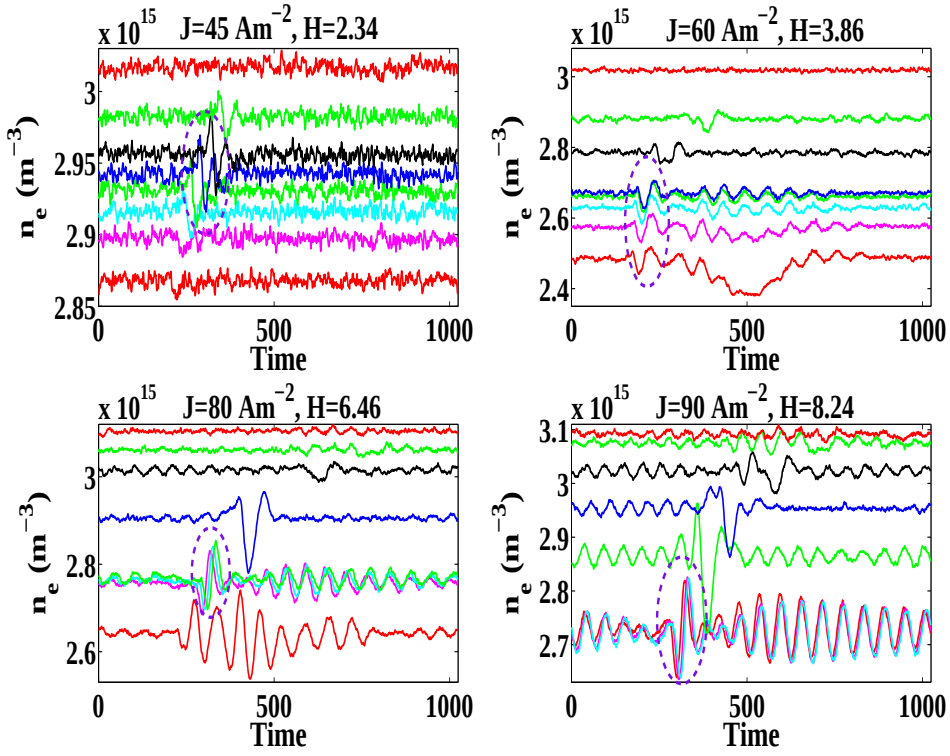

Figure 4.3: *Temporal evolution of electron plasma waves in electron density profile. Conditions : argon gas,* $\tilde{J}_0 = 45 - 90\ A/m^2$, $f_{rf} = 27.12\ MHz$, $H \approx 2.34 - 8.24$, $T_e = 2.5\ eV$, $T_i = 0.03\ eV$ *at density* $= 3.0 \times 10^{15}\ m^{-3}$.

phenomena can be observed on the right side of the figure, when the electron

sheath expands (dashed lines) and some travelling oscillations occur near the sheath edge. These travelling waves propagate towards the bulk plasma. The following conclusions can be made from figure (4.2):

1. Sheath width increases with increasing $\tilde{J}_0$ or H.
2. Electron plasma waves are absent at lower values of $\tilde{J}_0$ or H.
3. Electron plasma waves appear at higher values of $\tilde{J}_0$ or H.

Figure (4.3) shows the temporal evolution of the electron density (n_e), for the same initial conditions as shown in figure (4.2). Here the x-axis can be converted to real time (in seconds) by multiplying numbers at *x-axis* by factor of $\Delta t \sim 3.6009 \times 10^{-11}$. This temporal evolution indicates the following points:

1. Waves are present in each case *i.e.* from $H = 2.34 - 8.24$.
2. For lower values of H, wave amplitude is weak and waves are not visualized in the spatial profile of electron density for smaller values of H.
3. The wave amplitude increases with increasing H and at higher H, wave amplitude is significant and is also clearly observed in the spatial profile of electron density.
4. Electron plasma waves propagate towards bulk plasma and finally disappear.

Figure (4.4) shows the spatiotemporal profile of electron density at the specific positions (in the simulation region) and corresponding temporal evolution of electron density is plotted as indicated in figure (4.3).

It is important to investigate the origin of these waves. Figure (4.5) shows the spatiotemporal profile of electric field. Here H is varying from $3.86 - 14.57$ for the corresponding $\tilde{J}_0$ from $60 - 102$ A/m^2. When the sheath collapses, a

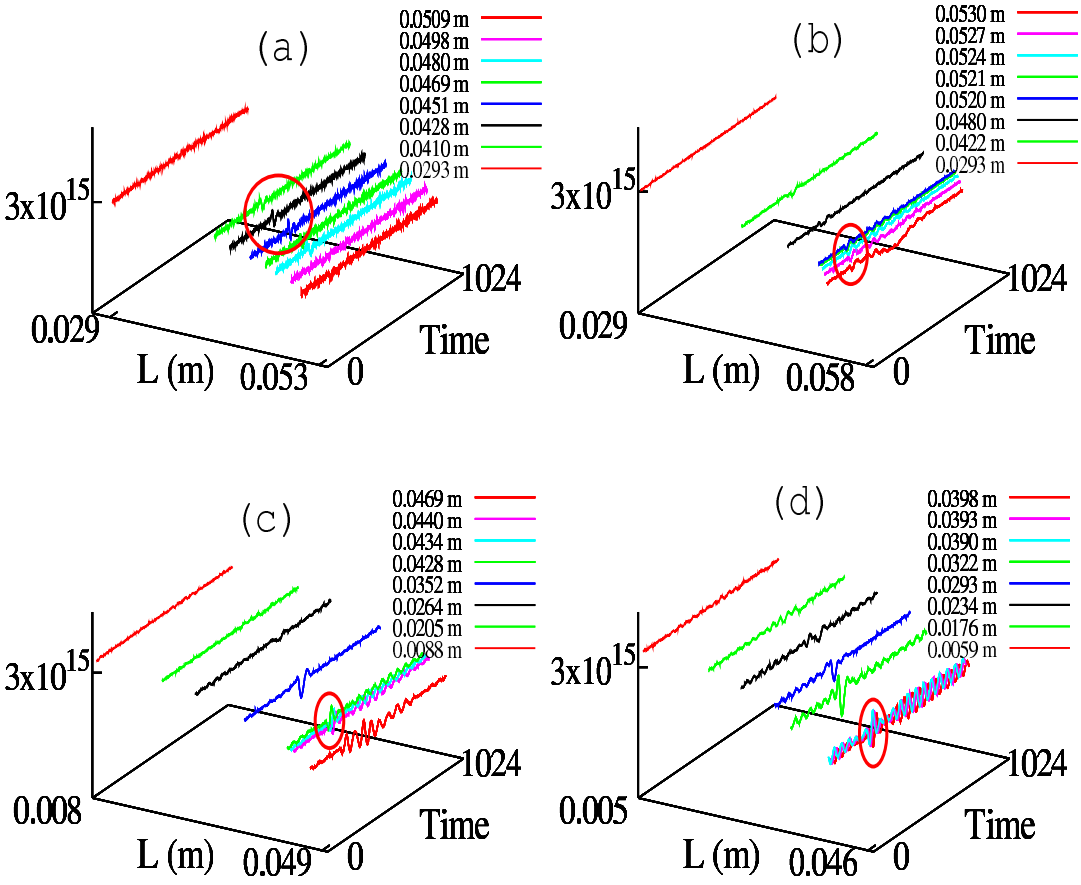

Figure 4.4: *Spatiotemporal profile of n_e which indicates the positions (in the simulation region) where temporal evolution of electron density is plotted as shown in fig (4.3). Here (a) $\tilde{J}_0 = 45\ A/m^2$, $H = 2.34$ (b) $\tilde{J}_0 = 60\ A/m^2$, $H = 3.86$ (c) $\tilde{J}_0 = 80\ A/m^2$, $H = 6.46$ and (d) $\tilde{J}_0 = 90\ A/m^2$, $H = 8.24$. Conditions : argon gas, $f_{rf} = 27.12\ MHz$, $T_e = 2.5\ eV$, $T_i = 0.03\ eV$ at density $= 3 \times 10^{15}\ m^{-3}$.*

field reversal region appears near the sheath edge in each case. For hydrogen and electronegative plasmas, field reversal has been reported in the literature [140, 164–167]. For rare gas discharges (neon) field reversal is reported by [161, 162]. Let us discuss the origin of the field reversal during the collapsing phase of sheath. Electrons are accelerated with the sheath edge as the sheath collapses towards the electrode. However, the thermal velocity of electrons is finite and

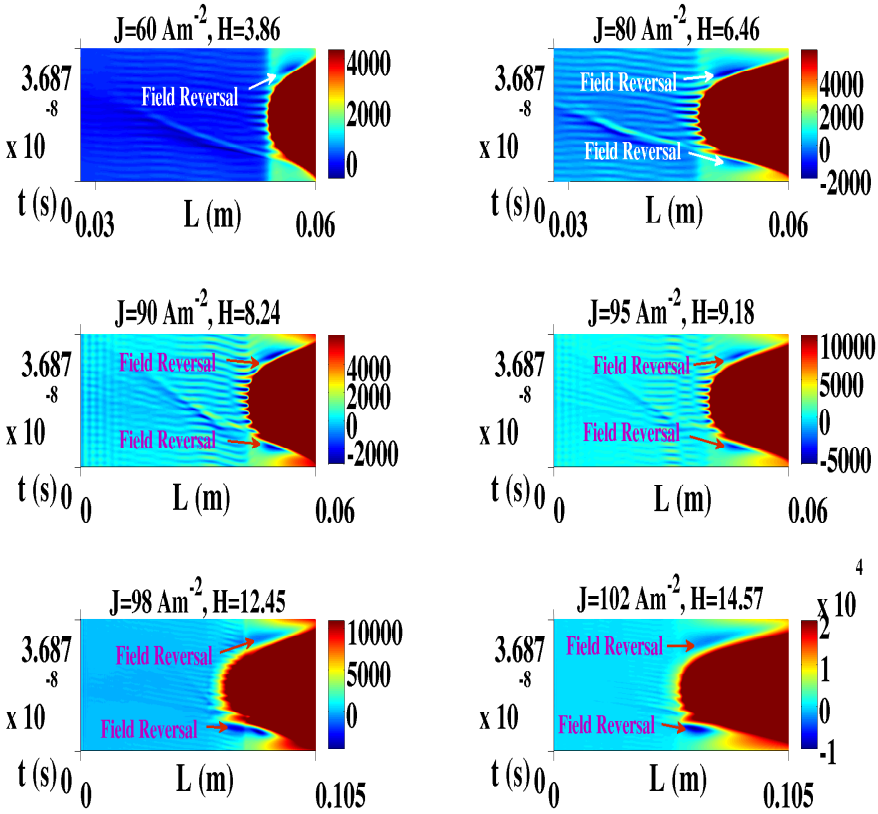

Figure 4.5: *A spatiotemporal profile of electric field. This figure shows the very high electric field inside the sheath and weak field in the bulk plasma. The field reversal region can be observed during the sheath expansion (for higher H) and when the sheath retreats towards electrode (for all H). Conditions : argon gas, $\tilde{J}_0 = 60 - 102\ A/m^2$, $f_{rf} = 27.12\ MHz$, $T_e = 2.5\ eV$, $T_i = 0.03\ eV$ at density $= 3 \times 10^{15}\ m^{-3}$.*

does not allow them to simply diffuse with the collapsing sheath. Because of this a local region of space charge comes into play, called field reversal, which accelerates electrons towards the electrode.

The most interesting part, which is not reported yet in the literature, is

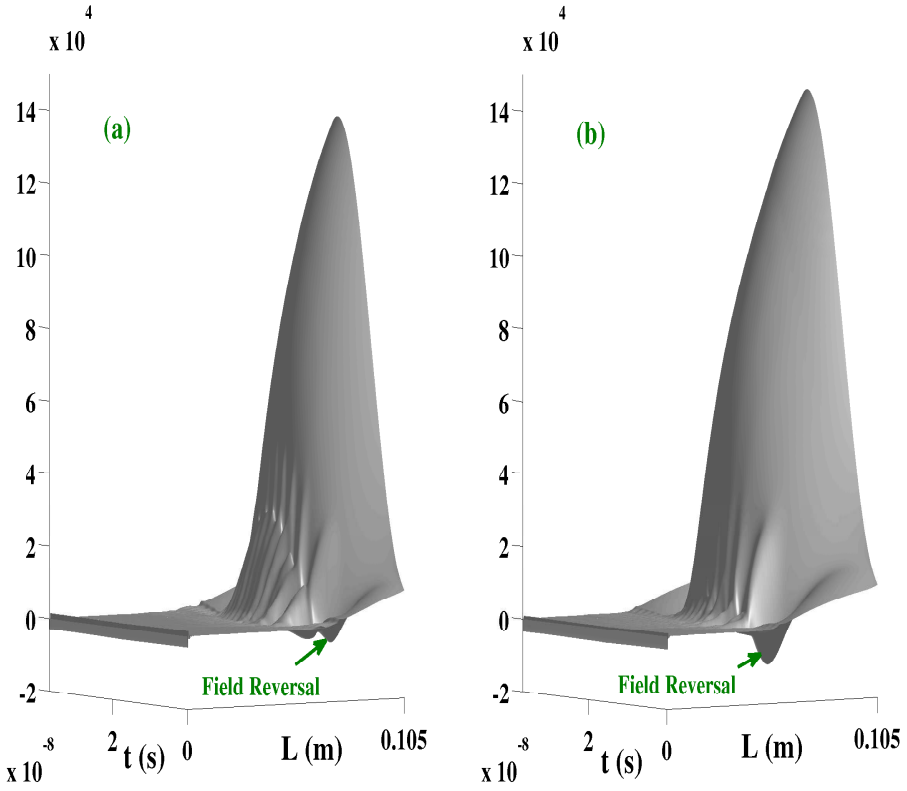

Figure 4.6: *A surface plot of electric field which shows a strong field reversal during the sheath expansion. (a) For* $\tilde{J}_0 = 98\ A/m^2$ *(b) For* $\tilde{J}_0 = 102\ A/m^2$*. Conditions: argon gas,* $T_e = 2.5\ eV$*,* $T_i = 0.03\ eV$*,* $f_{rf} = 27.12\ MHz$ *at density* $= 3 \times 10^{15}\ m^{-3}$*.*

the presence of field reversal during the expanding phase of the sheath. Most researchers work with low values of H and the existence of strong field reversal at the time of sheath expansion is not observed there. It is important to note that at higher values of H (> 9), the field reversal during the expanding phase of the sheath is several times higher than the field reversal during the collapsing phase of the sheath. Figure (4.6) shows the surface plot of electric field for $H = 12.45$ ($\tilde{J}_0 = 98$ A/m^2) and 14.57 ($\tilde{J}_0 = 102$ A/m^2). The most probable reason for this field reversal is electron fluid compression and rarefaction while the sheath expands and collapses. Physically, this phenomena can be understood as follows.

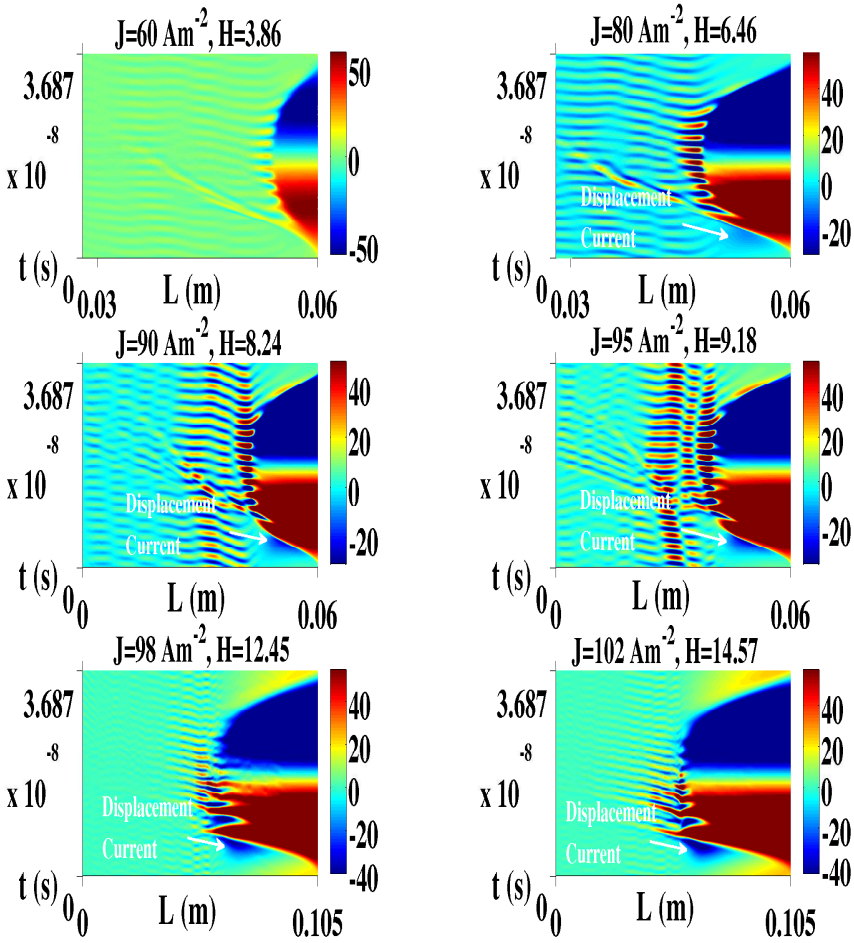

Figure 4.7: *Spatiotemporal profile of displacement current. Conditions : argon gas,* $\tilde{J}_0 = 60 - 102\ A/m^2$, $f_{rf} = 27.12\ MHz$, $H \approx 3.86 - 14.57$, $T_e = 2.5\ eV$, $T_i = 0.03\ eV$ *at density* $= 3.0 \times 10^{15}\ m^{-3}$.

When electrons move from the bulk towards the sheath; high energy electrons are the one who first feel the high sheath potential and bounce back from the expanding sheath towards the bulk plasma. These bounced electrons meet the low energy electrons moving towards the sheath at some point. At this position, the electron fluid is compressed and we observe a field reversal condition.

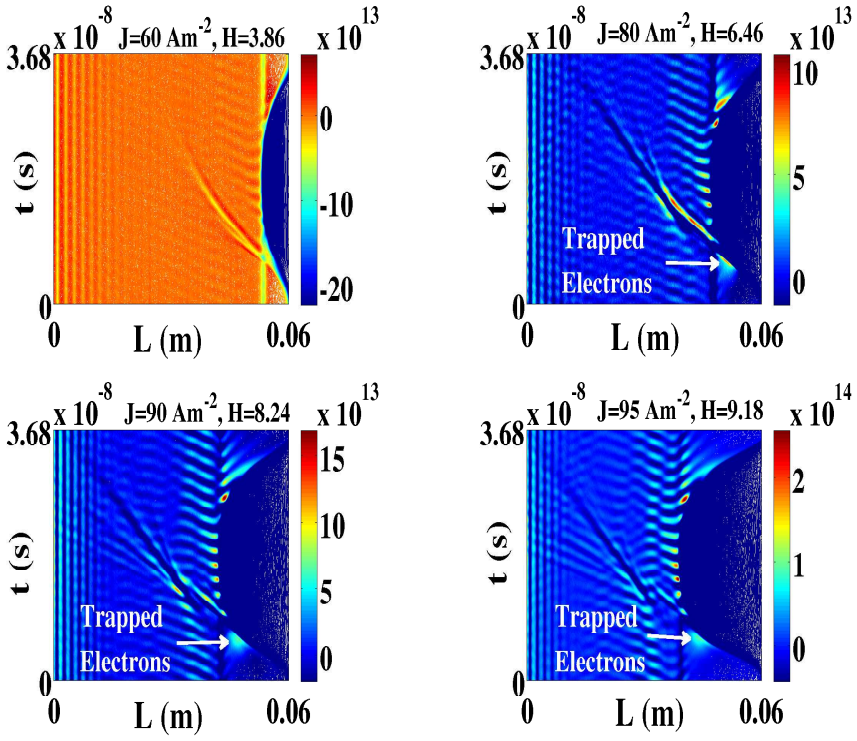

Figure 4.8: *A spatiotemporal profile of charge separation ($n_e - n_i$). Electrons are trapped near the sheath edge during the time of sheath expansion for higher values of* ***H****. Conditions : argon gas, $\tilde{J}_0 = 60 - 95\ A/m^2$, $f_{rf} = 27.12\ MHz$, $H \approx 3.86 - 9.18$, $T_e = 2.5\ eV$, $T_i = 0.03\ eV$ at density $= 3.0 \times 10^{15}\ m^{-3}$.*

Figure (4.7) shows the spatiotemporal profile of the displacement current. It is well known in CCPs that in general a significant displacement current is only inside the sheath region and that outside the sheath, only conduction current plays an important role. However where field reversal is observed a significant displacement current is clearly observed outside the sheath at the same position. For the existence of a displacement current outside the sheath, there must be trapping of electrons in that region. Simulation results show that there is a significant trapping of electrons in this region.

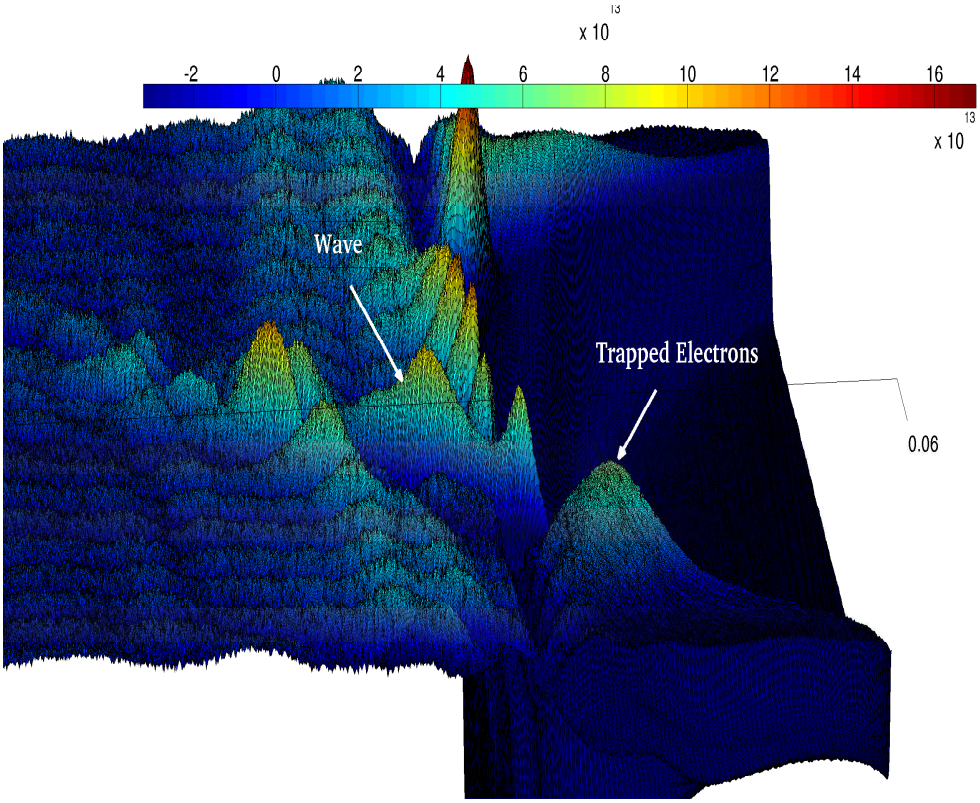

Figure 4.9: *A surface plot of charge separation ($n_e - n_i$). It shows that electrons are trapped near the sheath edge, during the sheath expansion. Conditions:* $\tilde{J}_0 = 90$ A/m^2, $H = 8.24$, $f_{rf} = 27.12$ MHz *at density* $= 3.0 \times 10^{15}$ m^{-3}.

Figure (4.8) shows the spatiotemporal profile of charge separation $(n_e - n_i)$. This figure indicates trapping of electrons near the sheath edge at the time of sheath expansion for higher values of H. This is the same region where field reversal is present. For lower values of H, there is no field reversal and no electron trapping. When electrons move from the bulk plasma towards the sheath they feel a very high sheath potential and bounce back. However when electrons enter the field reversal region they are trapped there. In steady state these trapped electrons are significant, and the trapping and untrapping of electrons at the field reversal position during the sheath expansion causes

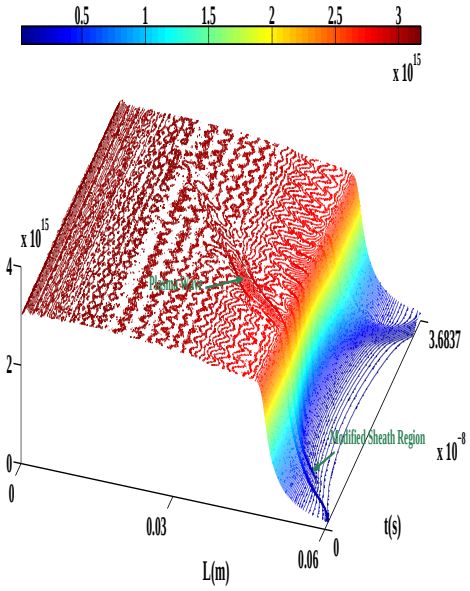

Figure 4.10: *A 3-D spatiotemporal profile of electron density. It shows that the sheath edge is modified and plasma waves are launched from near to this modified region. Conditions:* $\tilde{J}_0 = 80\ A/m^2$, $H = 6.46$ *at density* $= 3 \times 10^{15}\ m^{-3}$.

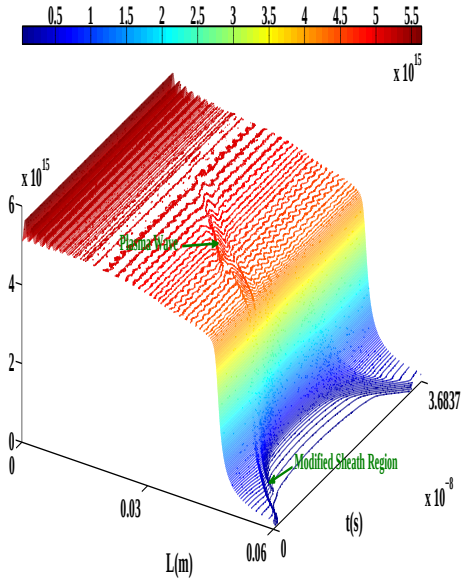

Figure 4.11: *A 3-D spatiotemporal profile of electron density. It shows that the sheath edge is modified and plasma waves are launched from near to this modified region. Conditions:* $\tilde{J}_0 = 120\ A/m^2$, $H = 8.974$ *at density* $= 5 \times 10^{15}\ m^{-3}$.

electron plasma wave formation near the sheath region. Electron trapping can also be observed in the surface plot of charge separation for $H = 8.24$, in figure (4.9).

Another interesting phenomena occurs because of trapping and untrapping of electrons is the modification of the sheath edge. During the sheath expansion, the electrons traps at the field reversal position. When these trapped electrons become untrapped, the sheath edge modifies and waves occur just near to this modified region. The 3-D spatiotemporal figure of electron density are shown for two different cases in figure (4.10) and (4.11). These figures shows one complete

RF cycle for applied frequency 27.12 MHz. The sheath structure modification and wave propagation can be seen in these figures. We have observed this type of phenomena in several other cases for different densities.

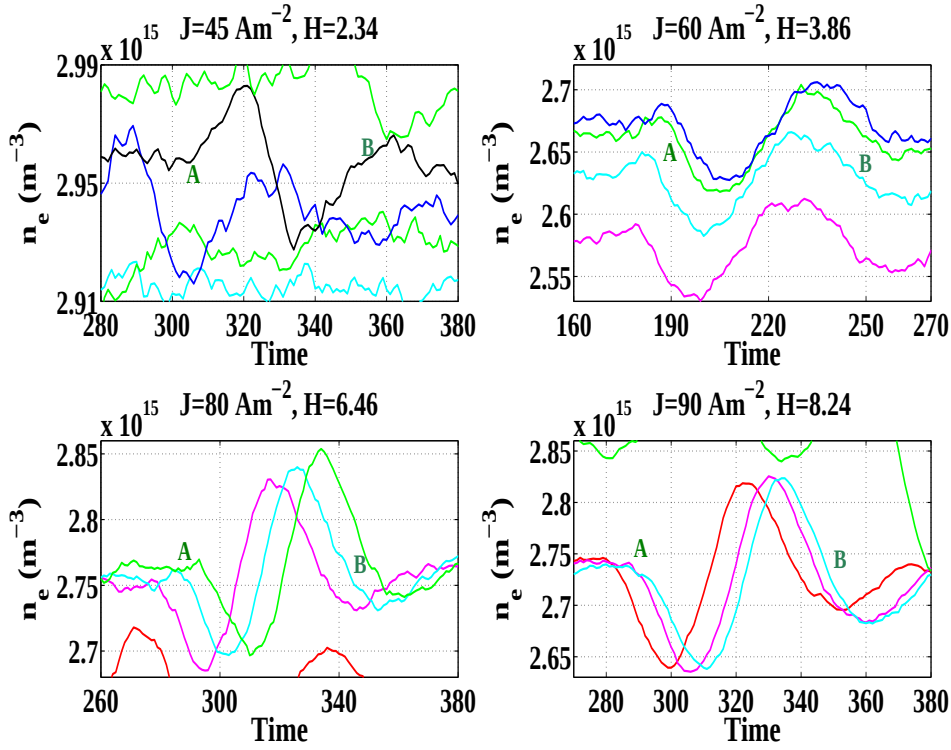

Figure 4.12: *Figure shows temporal evolution of electron density* n_e. *Conditions : argon gas,* $\tilde{J}_0 = 45 - 90\ A/m^2$, $f_{rf} = 27.12\ MHz$, $H \approx 2.34 - 8.24$, $T_e = 2.5\ eV$, $T_i = 0.03\ eV$ *at density* $= 3.0 \times 10^{15}\ m^{-3}$.

4.3.2 Temporal Evolution of Wave: The Evidence of Electron Plasma Wave

In this section we investigate whether these oscillations are either some travelling random oscillations or electron plasma waves. The frequency of these waves

are calculated here by investigation of temporal evolution of electron density. Figure (4.12) shows the zoomed part of figure (4.3) and clearly shows the wave propagation here. The input parameters are : $\tilde{J}_0 = 45 - 90$ A/m^2, $T_e = 2.5$ eV, $T_i = 0.03$ eV, $f_{rf} = 27.12$ MHz, and density is 3×10^{15} m^{-3}. H is varying from $2.34 - 8.24$. In figure (4.12), the x-axis shows time and can be converted to time in seconds by multiplying numbers at *x-axis* by factor of $\Delta t \sim 3.6009 \times 10^{-11}$. The wave frequency can be calculated with help of time period between "A" and "B", as shown in figure (4.12). The frequencies in different cases are :

- $\tilde{J}_0 = 45\ A/m^2$: $\omega_{wave} = 3.56 \times 10^9\ Hz$ and $(\omega_{pe})_{sim} = 3.06 \times 10^9\ Hz$.
- $\tilde{J}_0 = 60\ A/m^2$: $\omega_{wave} = 2.81 \times 10^9\ Hz$ and $(\omega_{pe})_{sim} = 2.96 \times 10^9\ Hz$.
- $\tilde{J}_0 = 80\ A/m^2$: $\omega_{wave} = 3.11 \times 10^9\ Hz$ and $(\omega_{pe})_{sim} = 2.98 \times 10^9\ Hz$.
- $\tilde{J}_0 = 90\ A/m^2$: $\omega_{wave} = 3.17 \times 10^9\ Hz$ and $(\omega_{pe})_{sim} = 2.98 \times 10^9\ Hz$.

Here it is clear that wave frequency ω_{wave} is always either greater than or equal to $(\omega_{pe})_{sim}$ *i.e.* $\omega_{wave} \geq (\omega_{pe})_{sim}$. This is true for other cases also.

Figure (4.13) shows the temporal evolution of electron density n_e. The simulation conditions are: RF current drive amplitude $\tilde{J}_0 = 120$ A/m^2 applied at density 5×10^{15} m^{-3}. The applied frequency is $f_{rf} = 27.12$ MHz, system length is $l = 0.06$ m, electron temperature is $T_e = 2.5$ eV and ion temperature $T_i = 0.03$ eV. This figure shows results for a single RF cycle. It is clear from this figure that a wave starts near $t \sim 260$ and propagates with time, finally disappearing at $t \sim 600$. Now to calculate the frequency of these waves, see case (b) in figure (4.13) which is zoomed part of case (a) in same figure. By calculating the time period between "A" and "B", the frequency can be calculated and it is $\omega_{wave} \approx 3.561 \times 10^9$ Hz. The electron plasma frequency $(\omega_{pe})_{sim}$ is 3.568×10^9 Hz. So $\omega_{wave} \approx (\omega_{pe})_{sim}$ and it shows the signature of electron plasma waves.

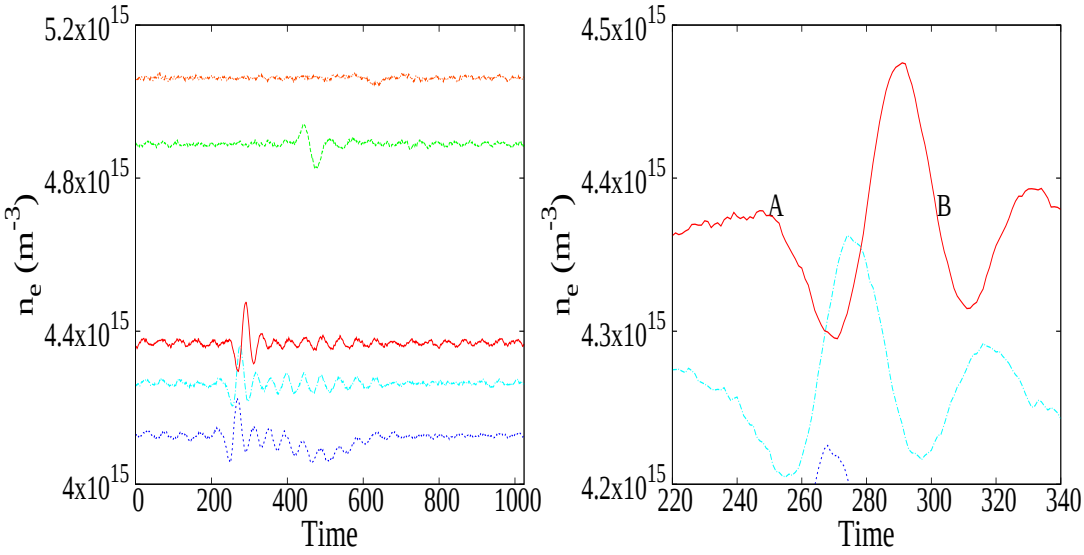

Figure 4.13: *Figure (a) shows temporal evolution of electron density n_e. Figure (b) shows zoomed in figure of temporal evolution of electron density n_e. Conditions: $\tilde{J}_0 = 120\ A/m^2$, $T_e = 2.5\ eV$, $f_{rf} = 27.12\ MHz$ at density $= 5 \times 10^{15}\ m^{-3}$.*

4.3.3 Dependence of wave amplitude on current density amplitude

The study of dependence of the wave amplitude on current density amplitude, $\tilde{J}_0$ or H is very interesting and is investigated here. In the literature [59, 151, 168], it is reported that the wave amplitude is enhanced as the ratio of the drift velocity to the thermal velocity increases. Hence increasing $\tilde{J}_0$ means increasing drift velocity. Thermal velocity is nearly constant here.

Figure (4.14) shows the plot of wave amplitude (A_w) versus $\tilde{J}_0$ for two different densities *i.e.* 3×10^{15} m^{-3} and 5×10^{15} m^{-3}. Case (a) in figure (4.14) shows that the wave amplitude increases for $\tilde{J}_0 \sim 45 - 90$ A/m^2 but drops at $\tilde{J}_0 \sim 95$ A/m^2. Similarly, case (b) in figure (4.14) shows that the wave ampli-

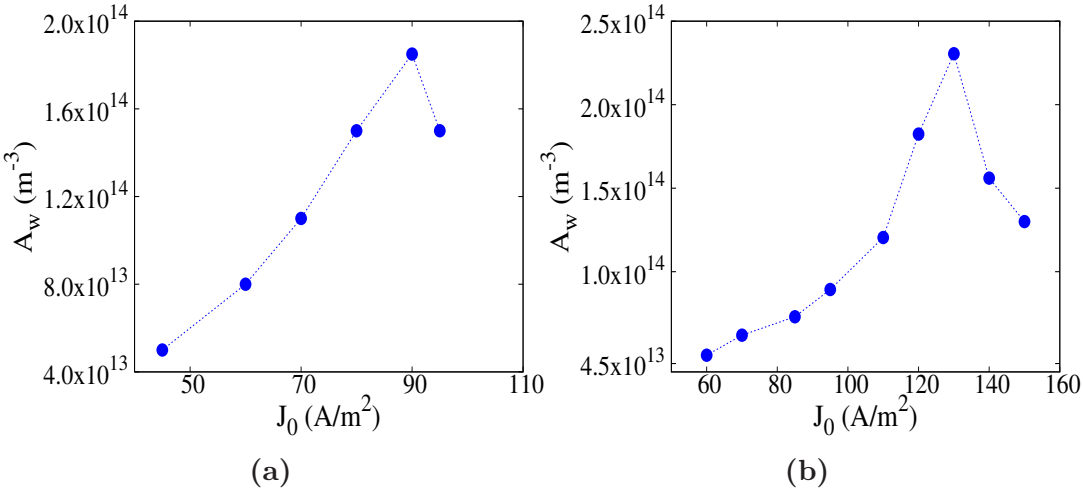

Figure 4.14: *Figure shows variation of wave amplitude with current density amplitude $\tilde{J}_0$. (a) For density 3×10^{15} m^{-3}. (b) For density 5×10^{15} m^{-3}. Conditions : argon gas, $T_e = 2.5$ eV, $f_{rf} = 27.12$ MHz.*

tude increases for $\tilde{J}_0 \sim 60 - 130$ A/m^2 but drops at $\tilde{J}_0 \sim 140 - 150$ A/m^2. So both results indicate that initially the wave amplitude increases as the ratio of drift velocity to thermal velocity increases, confirming the argument reported in the literature. On the other hand present results show that at constant density wave amplitude is a maximum at a particular $\tilde{J}_0$ (*i.e.* 90 A/m^2 for 3×10^{15} m^{-3} and 130 A/m^2 for 5×10^{15} m^{-3}) and after that wave amplitude decreases rapidly however the ratio of drift velocity to the thermal velocity increases.

4.4 Effect of Collisions on Waves

Collisions of particles may create different types of phenomena like ionization of neutral particles, neutralization of ionized particles and excitation of colliding particles. During a collision the energy or momentum of one or both particles may change. In gas discharges, important collisions are between neutral gas

atoms, positive ions and electrons. In the case of *elastic* collisions, the total kinetic energy of the colliding particles remains conserved and only an exchange of momentum occurs between colliding particles . Electrons collide with neutral gas atoms by a process of elastic scattering so electron momentum and kinetic energy are conserved here. Ionization and excitation are *inelastic* processes in which the sum of kinetic energies are not conserved but momentum is conserved (as it is for *elastic* collisions). Here the sum of kinetic energies before a collision is greater than after the collision. Part of the kinetic energy is changed into some other form of energy.

In the case of argon discharges, the electron argon collision processes can be described by the following equations

$$\begin{aligned} &e^- + Ar \longrightarrow Ar^+ + 2e^- \qquad \textbf{(ionization)} \\ &e^- + Ar \longrightarrow e^- + Ar^* \longrightarrow e^- + Ar + h\nu(photon) \quad \textbf{(excitation)} \\ &e^- + Ar \longrightarrow e^- + Ar \qquad \textbf{(elastic scattering)} \end{aligned} \tag{4.1}$$

Quantitative studies of the scattering of electrons by atoms has been done by Ramsauer [169] and Brode [170, 171]. Collisions are described by the most fundamental quantity called the *cross section* $\sigma(v_R)$, where v_R represents the relative velocity of colliding particles before the collision. Trajmar and McKonkey [172] and Zecca *et al.* [173] published a complete set of cross section data till the year 1994. In present research work, we consider only elastic scattering cross sections for electrons in particle-in-cell simulations of argon discharges, ionization and excitation are not taken into account here. A Monte-Carlo scheme is implemented in the PIC simulation to handle the collisions in which the particles carry information about their collision probability. So a collision probability is calculated for each of the reactant particles depending on their velocity from a known cross-section. After that a random number is generated. A reaction happens, if the generated random number is smaller than the collision proba-

bility.

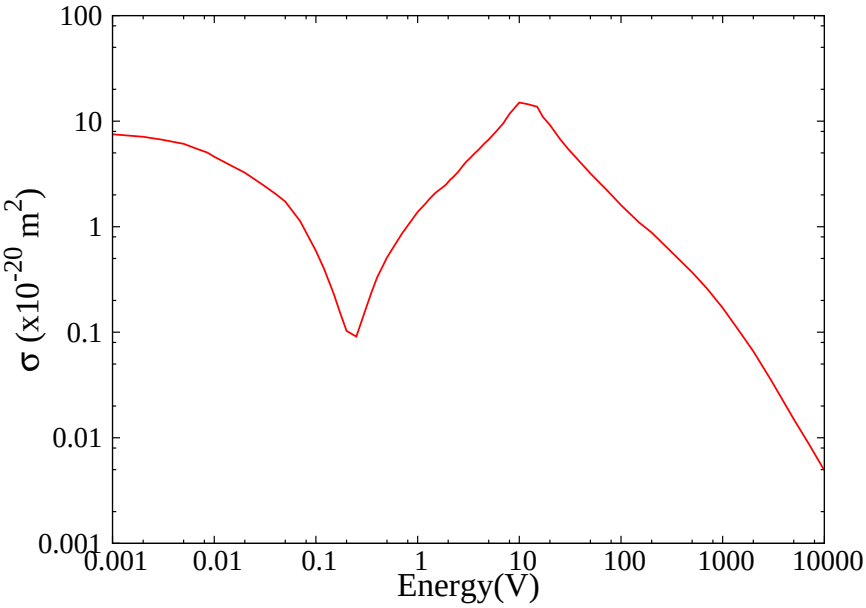

Figure 4.15: *The elastic scattering cross sections for electrons in argon gas.*

Maxwellian electrons collide with argon atoms elastically, the *mean free path* between collisions is defined as

$$\lambda_e = \frac{1}{n_g \sigma} \,. \tag{4.2}$$

The mean time between collision (τ) is defined as

$$\tau = \frac{\lambda_e}{v}, \tag{4.3}$$

and inverse of this mean time is defined as the collision frequency

$$\nu_m \equiv \tau^{-1} = n_g \sigma v \,, \tag{4.4}$$

where σ is the energy dependent cross-section, v is the relative velocity of the colliding species, and n_g is the neutral gas density. *Rate constant* $K(T_e)$ is defined as the collision frequency per unit density

$$K = \langle \sigma v \rangle \,, \tag{4.5}$$

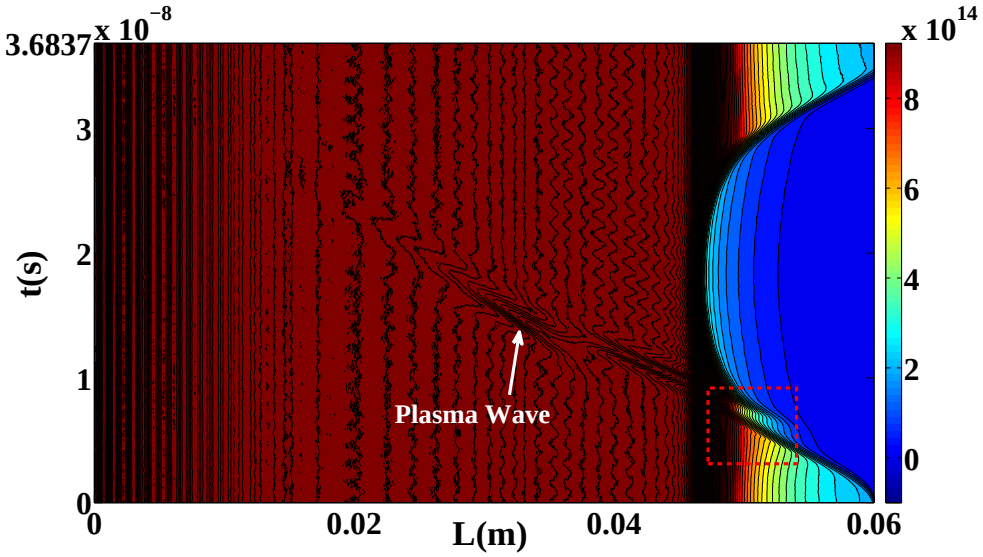

Figure 4.16: *Spatiotemporal profile of electron density (n_e) for collisionless case. The modified sheath region is enclosed by rectangle box shown in figure. Conditions : argon gas, $\tilde{J}_0 = 120\ A/m^2$, $T_e = 2.5\ eV$, $f_{rf} = 27.12\ MHz$ and density is $5 \times 10^{15}\ m^{-3}$.*

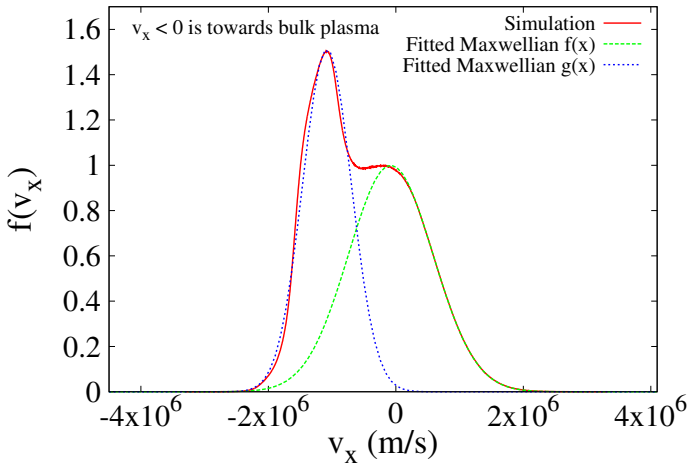

Figure 4.17: *Figure shows the electron velocity distribution function in modified sheath region (area enclosed by rectangle box) in figure (4.16). Electrons propagate towards bulk plasma for $v_x < 0$.*

which is averaged over Maxwellian distribution of cross section σ and relative velocity v. Using (4.4) and (4.5), the collision frequency can also be defined as

$$\nu_m = K n_g \, . \tag{4.6}$$

Elastic momentum transfer cross section for electrons in argon discharges is shown in figure (4.15). This data is originally from Yamabe, Buckman and Phelps [174].

As discussed in previous sections, the Landau damping phenomenon is the dominant process in a collisionless plasma. In this section, we will investigate the effect of electron elastic collisions on electron plasma waves. Simulation results show that in the collisionless case electron plasma waves occur near the sheath edge and propagate towards the bulk plasma. The amplitude of these waves damp and finally the waves disappear. This happens because of the Landau damping phenomena. Here the collisionless case results are compared with results at different pressures, 20 mTorr and 100 mTorr. All simulation runs are for argon discharges. Input parameters are, $\tilde{J}_0 = 120$ A/m^2, $f_{rf} = 27.12$ MHz, $T_e = 2.5$ eV, $T_i = 0.03$ eV and the density is 5×10^{15} m^{-3}.

Figure (4.16) shows the spatiotemporal profile of electron density for the collisionless case where the modified sheath region is enclosed by a rectangular box. During the sheath expansion, the area near the sheath edge distorts significantly and wave starts near this region. Figure (4.17) represents the electron velocity distribution function in the modified sheath region (area enclosed in rectangular box). It is clear from the figure that two Maxwellian curves are well fitted with simulation results. Here $v_x < 0$ represents the electrons moving towards bulk plasma (opposite to the sheath region) and $v_x > 0$ represents electrons travelling towards the sheath region. Here the y-axis has arbitrary units.

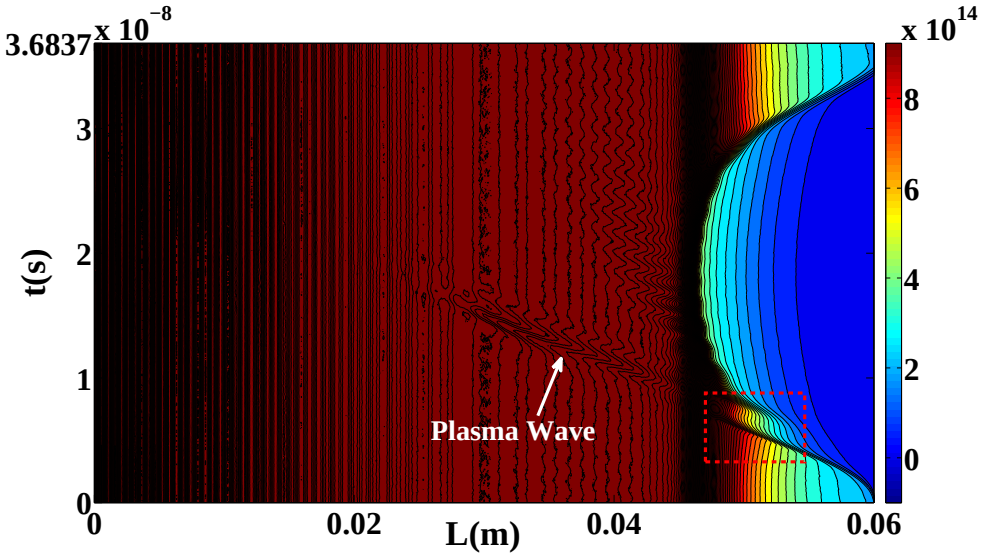

Figure 4.18: *Spatiotemporal profile of electron density (n_e) at pressure 20 $mTorr$. The modified sheath region is enclosed by a rectangle box as shown. Conditions : argon gas, $\tilde{J}_0 = 120\ A/m^2$, $T_e = 2.5\ eV$, $f_{rf} = 27.12\ MHz$ and density is $5 \times 10^{15}\ m^{-3}$.*

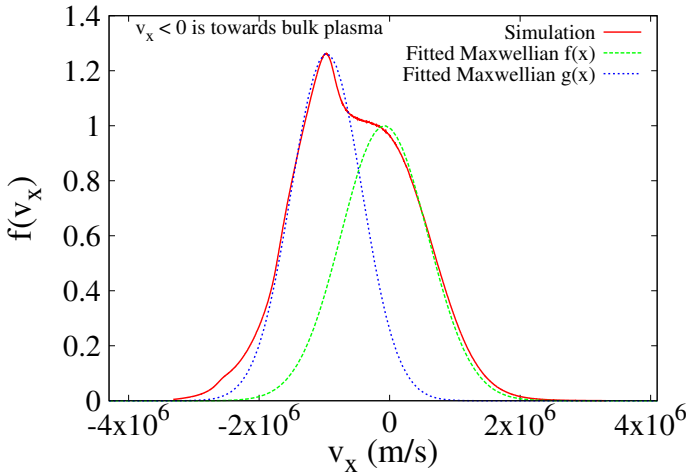

Figure 4.19: *Figure shows the electron velocity distribution function in the modified sheath region (area enclosed by rectangle box) in figure (4.18) at pressure 20 $mTorr$. Electrons propagate towards bulk plasma for $v_x < 0$.*

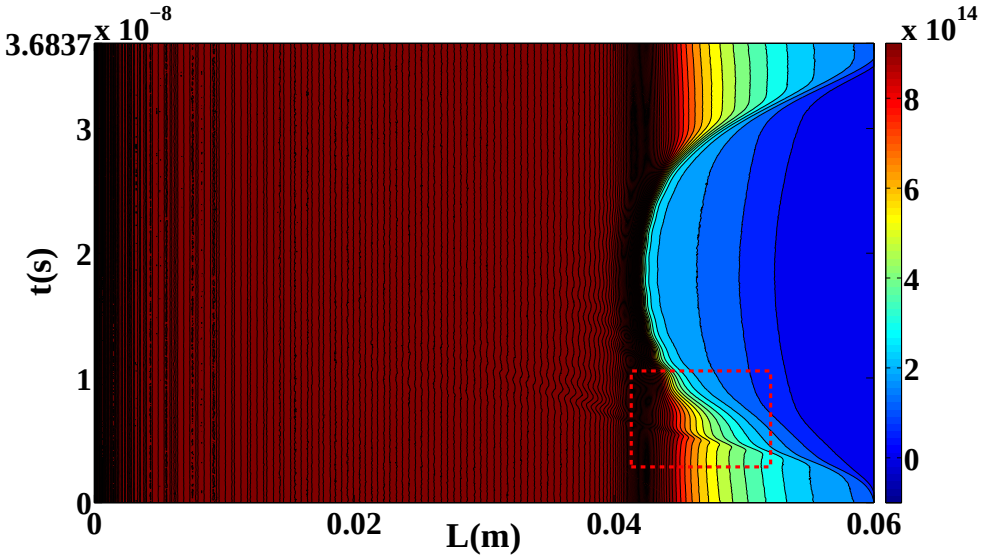

Figure 4.20: *Spatiotemporal profile of electron density (n_e) at pressure 100 $mTorr$. The modified sheath region is enclosed by a rectangle box as shown. Conditions : argon gas, $\tilde{J}_0 = 120\ A/m^2$, $T_e = 2.5\ eV$, $f_{rf} = 27.12\ MHz$ and density is 5×10^{15} m^{-3}.*

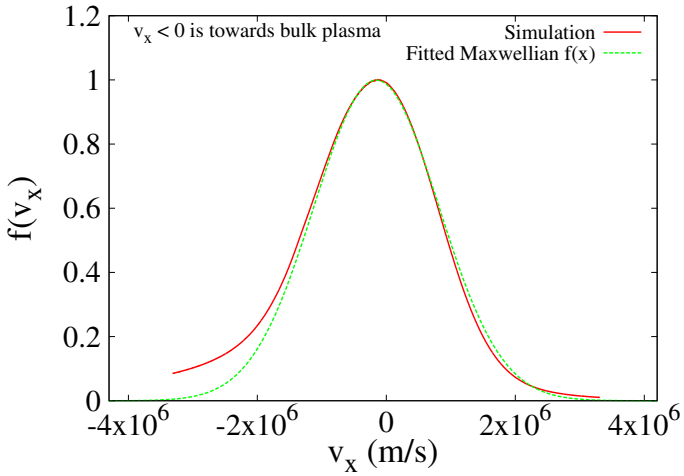

Figure 4.21: *Figure shows the electron velocity distribution function in the modified sheath region (area enclosed by rectangle box) in figure (4.20) at pressure 100 $mTorr$. Electrons propagate towards bulk plasma for $v_x < 0$.*

The fitted Maxwellian functions are given by

$$\begin{aligned} f(x) &= Aexp(B(x-x_0)^2)\,, \\ g(x) &= A'exp(3B(x-x_0')^2)\,, \end{aligned} \tag{4.7}$$

where A and A' shows the amplitudes of the Maxwellian functions and B represents $-m_e/2k_BT_e$. However it is clear from function $g(x)$ that a beam of high velocity electrons comes out from the modified sheath region and penetrates into the bulk plasma. Electron plasma waves starts near the sheath region and finally damps at a distance of approx 0.025 m.

Figure (4.18) represents the spatiotemporal profile of the electron density at 20 mTorr. Here also the modified sheath region is clearly seen in the rectangular box. Figure (4.19) shows the electron velocity distribution function in the modified sheath region. Two Maxwellian curves are fitted with simulation data and the curve has a peak at 1×10^6 m/s, which is not much less compared to the collisionless case. Plasma waves which starts near the sheath edge finally damp at a distance of approx 0.032 m. At high pressures *i.e.* 100 mTorr the modified sheath region almost disappears (see figure (4.20)) inside rectangular box. The electron velocity distribution function shown by figure (4.21) is almost Maxwellian and well fitted by analytical expression of Maxwellian distribution. The wave phenomenon also disappears here.

The results above indicate that in the presence of high pressure, the modified sheath region disappears and wave effects diminish very quickly.

4.5 Summary

The existence of electron plasma waves near the plasma-sheath interface has been observed and investigated. The quasi-neutrality breaks down due to the overshoot of high velocity electrons into the bulk plasma at the time of sheath

expansion, and as a result electron plasma waves occur in the sheath vicinity. The possibility for the oscillating energy to be transferred to electron thermal energy by the Landau damping mechanism is discussed.

The spatiotemporal profile of electron density shows that electron plasma waves start from the sheath edge and propagate towards the bulk and finally disappear. It is also observed that the sheath structure is modified during the sheath expansion. The spatiotemporal profile of electric field indicates the presence of strong field reversal near the modified sheath region for higher values of H. The possible reason for the field reversal is the compression and rarefaction of electron fluid when the sheath expands and collapses. The profile of charge separation shows the evidence of electron trapping near the reverse field region. The trapping and untrapping of electrons during the expansion and collapse of the sheath causes the launching of waves from near the sheath region. The evidence of significant displacement current in this region is also observed.

The temporal evolution of electron plasma waves is discussed. The frequency of the waves ω_{wave} is calculated and it is either greater than or equal to ω_{pe}. It indicates that these waves are electron plasma waves. The effect of electron elastic collisions on waves are also studied. The modified sheath region near the sheath edge disappears at high collision rates *i.e.* at high pressure.

CHAPTER 5

Study of Stochastic Heating and Wave Phenomena in Dual Frequency Capacitively Coupled Plasma Discharges

5.1 Introduction

Wide plasma uniformity, fast processing rates and damage-free characteristics are the main requirements for modern plasma etching industry. Anisotropy is a critical process parameter in integrated circuit manufacturing and is accomplished by radio-frequency (RF) plasma etching. Ions need sufficient energy and significant flux to weaken the chemical bonds at the surface and to make the process worthwhile respectively in the etching process. Many plasma processing necessities are fulfilled by conventional capacitively coupled plasma (CCP) reactors powered by a single RF (13.56 MHz) source. The high voltage sheath of CCP produces ions having high energies. One must increase the RF power to increase the ion flux; but increase in RF power also increases the sheath volt-

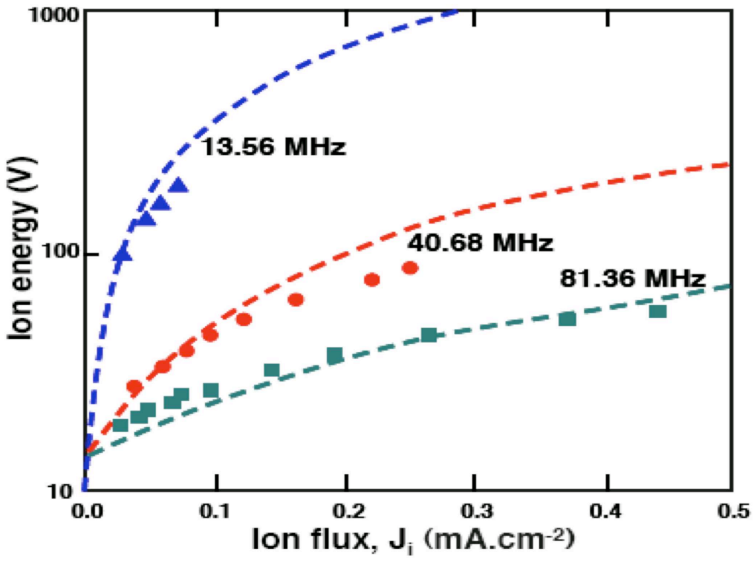

Figure 5.1: *Graph of ion flux vs ion energy for argon plasma discharges at 15 mTorr. It shows the variation of ion flux and ion energy at three different frequencies in single frequency capacitive discharges. The data points are from experiments and dashed lines shows the results from a global model with equivalent electrical circuit. (Perret et al. [175])*

age. As a consequence, highly energetic ions can damage the fragile surfaces; on the other hand, low RF power limits the ion flux and one has to compromise with etch rate. However, semiconductor industries need minimum damage on the substrate with more accurate transfer patterns on semiconductor devices by the precise control of both the ion flux and the ion bombardment energy. Single frequency reactors have limitations and failed to provide an independent control of ion energy and ion flux. Ion flux and the ion energy relationship in the case of various single frequency capacitive discharges is shown in figure (5.1) by Perret et al. [175]. This graph indicates that at high frequencies, high density (*i.e.* high ion flux) CCP plasmas can be produced, but sacrifices the option

of high energy ion source. Hence dual-frequency capacitively coupled plasmas (DF-CCPs) systems operated with two distinct power sources have been developed and studied to solve this puzzle [149, 176–178]. In the last couple of years DF-CCPs have also been studied experimentally by Booth et al. [179], Gans et al.[136], Worsley et al. [180], Karkari et al. [181] and Curley et al. [182].

5.2 Principle Mechanism of Dual-Frequency Capacitively Coupled Plasma Discharges

As discussed earlier, independent control of ion energy and ion flux is the motivation of dual-frequency capacitively coupled discharges. The physical mechanism of high frequency source (f_{hf}) and low frequency source (f_{lf}) can be explained as follows:

- the high frequency source (f_{hf}) can sustain the plasma *i.e.* control the ion flux.
- the low frequency source (f_{lf}) can control the sheath voltage *i.e.* the mean ion bombarding energy.

Figure (5.2) shows the schematic diagram of a dual frequency capacitively coupled plasma source. In the ideal case, the sheath is electron free and works like a capacitor between the conducting plasma and the electrode, so only displacement current can pass through the sheath. The conduction current flows in the bulk plasma (electron rich). Because of collisions between electrons and neutral gas molecules, the resistive component (R_p) also plays an important role in the bulk plasma equivalent circuit. The relation between current density and electric field is given by

$$\vec{J} = \sigma_p \vec{E}. \tag{5.1}$$

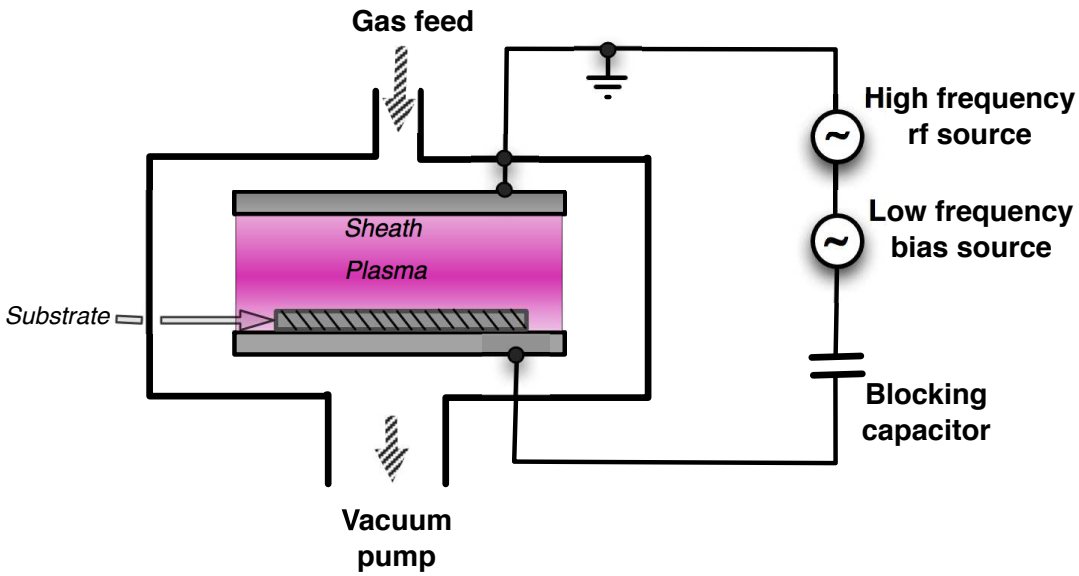

Figure 5.2: *Schematic diagram of a dual-frequency capacitive plasma source.*

Here σ_p is complex conductivity given by [6]

$$\sigma_p = \frac{n_e e^2}{m_e(\nu_{me} + i\omega_{rf})}. \tag{5.2}$$

In the bulk plasma, the phase shift between the electric field and electron current is due to electron inertia. The phase shift depends on the number of collisions (that cause a deflection of the electrons) and on the applied RF frequency (ω_{rf}). In the plasma region a complex conductivity includes the phase shift caused by an elastic electron-neutral collision rate ν_{me}.

The modelling of phase shift can be done as being equivalent to the phenomena of the reactance of an inductor, L_p. Here a parallel combination of resistor and inductor represents the bulk plasma in equivalent circuit. The impedance of the capacitive sheath is given by

$$Z_{sh} = \frac{1}{j\omega_{rf} C_{sh}}, \tag{5.3}$$

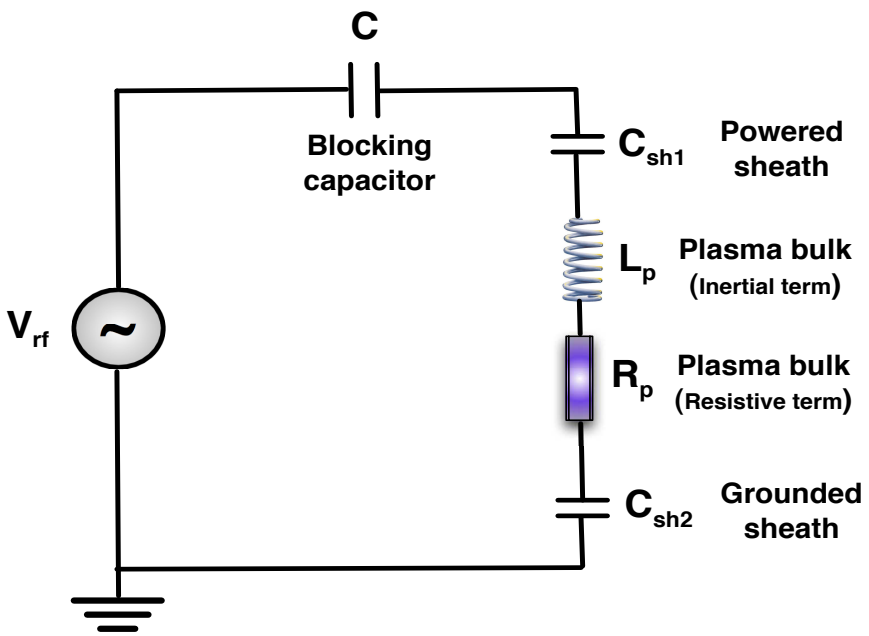

Figure 5.3: *Schematic diagram of equivalent circuit model of a capacitively coupled plasma source.*

where ω_{rf} is the applied RF source frequency. Similarly the impedance of the inductive bulk plasma can be represented as

$$Z_p = j\omega_{rf} L_p + R_p. \tag{5.4}$$

Here L_p is the inductance and R_p is the resistance of the bulk plasma. In the low pressure case, electron-neutral gas collisions are rare so $j\omega_{rf} L_p > R_p$. The independent control of ion flux and ion energy can be explained by using the equivalent circuit model of a CCP as shown in figure (5.3). The applied RF voltage (of the lower and upper frequency sources) mainly drops across the sheaths because $Z_{sh} \gg Z_p$. Equation (5.3) indicates that $Z_{sh} \propto \omega_{rf}^{-1}$, so the voltage of the lower frequency source mainly drops across the sheath. On the other hand, equation (5.4) shows $Z_p \propto \omega_{rf}$, so the voltage of the high frequency source predominantly drops across the bulk plasma. In the ideal case, the low

frequency (ω_{lf}) controls the sheath voltage *i.e.* ion bombarding energy while the high frequency (ω_{hf}) can control the plasma density *i.e.* the ion flux.

In low pressure RF discharges, stochastic heating dominates and the power absorbed by electrons is given by

$$\bar{S}_{stoc} \propto \omega_{rf}^2 V_{rf}. \tag{5.5}$$

The plasma density is also directly proportional to the stochastic heating [6] *i.e.*

$$n \propto \bar{S}_{stoc}. \tag{5.6}$$

This has also been seen experimentally by Perret *et al.* [175] (figure(5.1)) and by Jolly *et al.* [183]. Let us assume that the voltage amplitudes of the low and high driving frequencies are V_{lf} and V_{hf} respectively. Now if one can satisfy the following condition

$$\omega_{hf}^2 V_{hf} \gg \omega_{lf}^2 V_{lf}, \tag{5.7}$$

then the plasma density *i.e.* the ion flux is controlled by ω_{hf}, the high frequency source [184].

The mean ion bombarding energy ξ_i is equivalent to the total DC bias voltage across the collisionless sheath. The sheath voltage is approximately equal to the applied RF voltage. For the dual-frequency case

$$\xi_i \propto |V_{hf} + V_{lf}|. \tag{5.8}$$

For the case of

$$V_{lf} \gg V_{hf}, \tag{5.9}$$

the DC sheath voltage (*i.e.* mean ion bombarding energy) can be controlled by V_{lf}. From equation (5.7) and (5.9), the condition for independent control of ion energy and ion flux is the following [6]:

$$\frac{\omega_{hf}^2}{\omega_{lf}^2} \gg \frac{V_{lf}}{V_{hf}} \gg 1. \tag{5.10}$$

Lieberman *et al.* [6] showed that $J_{rf} \propto \omega_{rf} V_{rf}^{3/4}$. So if J_{rf} is the controlling parameter, equation (5.10) can be inverted by substitution of V_{rf}. Thus, equation (5.10) indicates that $J_{hf} \gg J_{lf}$, where J_{lf} and J_{hf} are the low and high frequency current density amplitudes respectively. Again equation (5.10) shows that even in the case when the first inequality is true, the collisionless heating and in consequence of that the ion density and ion flux are not completely independent of the applied low frequency, ω_{lf}. In DF-CCP, the higher frequency is superimposed on the lower frequency. However, for the case of stochastic heating some form of coupling is assumed between the low and high frequency components. In the dual-frequency case, the total stochastic heating effect is a collective effect due to the presence of a high frequency sheath oscillating across a low frequency sheath. The characteristic ratio of high frequency (f_{hf}) to low frequency (f_{lf}) is greater than 10. Typically, the high frequencies and low frequencies are chosen to be $f_{hf} \sim 27.12 - 160$ MHz and $f_{lf} \sim 2 - 13.56$ MHz respectively.

Ohmic heating and stochastic heating are the two main electron heating mechanisms in such discharges. Ohmic heating occurs in the bulk and sheath regions because of electron-neutral collisions and stochastic (or collisionless) heating takes place at the sheath edge because of the momentum transfer from high voltage moving sheath to electrons. While ohmic heating dominates at relatively high pressures, stochastic heating is the dominant heating mechanism at low pressures (in the mTorr range) and is expected to sustain the plasmas. In the last few decades, the industrial application of RF discharges at low pressures has increased, due to this it is very important to understand the physical mechanism of stochastic heating. Stochastic heating in the case of low pressure dual frequency capacitive discharges has been studied by different analytical models [1, 177, 184–190]. Lieberman *et al.* [191], Kim *et al.* [185] and Boyle

et al. [184] showed that independent control of ion energy and ion flux can be achieved by the application of low and high frequency drives at the electrode. Robiche *et al.* [178] and Franklin [192] indicated that sheath motion in dual-frequency discharges is quite complicated. As discussed earlier (chapter 3), physical models to understand stochastic heating given by Godyak [28] and Lieberman [30] in which electrons gain energy by the oscillatory sheath edge, fail to conserve current through the sheath region. When current conservation is imposed by modifying these models, the stochastic heating effect vanishes. This controversy was addressed by Gozadinos *et al.* [43]. They developed a fluid model where the electron fluid in the sheath region is described by moment equations with a simple kinetic closure. Current conservation is precisely handled by this model. Later Turner *et al.* [187, 188] developed a fluid model for collisionless heating in the dual frequency sheath, which is an extension of the fluid equations of Gozadinos *et al.* [43]. A kinetic treatment in which the current is conserved has been developed by Kaganovich [34]. He introduced ion density as a step function inside the sheath. The two-step ion density model is a useful tool for the investigation of stochastic heating in single frequency RF discharges, even though it is not realistic. Kawamura *et al.* [1] has extended the Kaganovich [34] model for the case of dual-frequency CCP. We will briefly discuss this model in the next section.

5.3 Analytical Model for Dual-Frequency CCP

Schematic representation of DF-CCP, illustrating the mechanism of low frequency sheath motion and high frequency sheath motion has been displayed in figure (5.4). The analytical model for the calculation of stochastic heating in a dual-frequency CCP has been developed by Kawamura *et al.* [1]. This model is an extension of the Kaganovich [34] model for stochastic heating calculation for

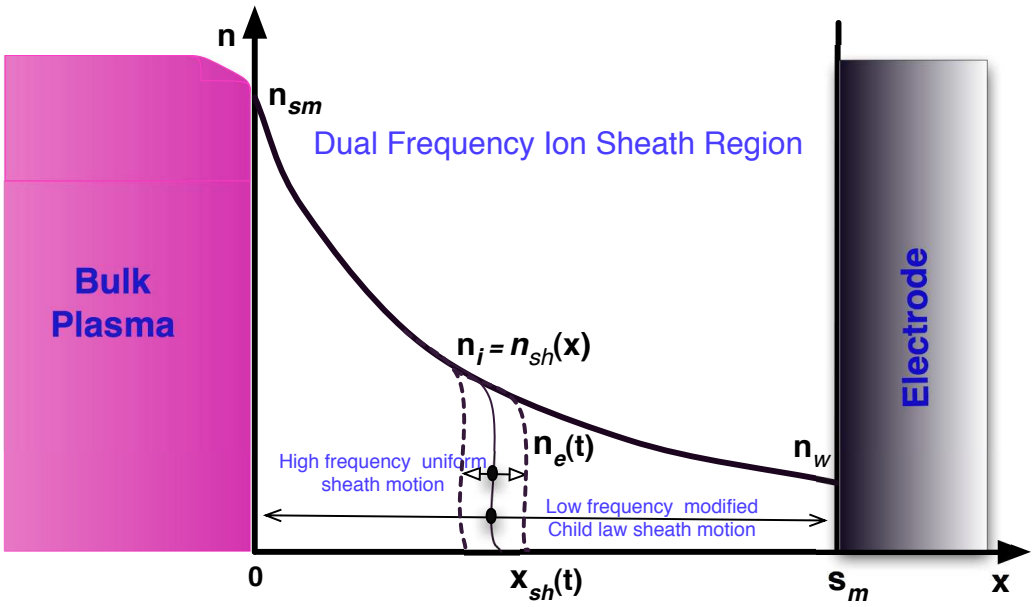

Figure 5.4: *Schematic diagram of dual-frequency capacitive sheath.*

the single-frequency CCP case. In the dual-frequency model, a high frequency (f_{hf}) uniform sheath motion is superimposed on a low-frequency (f_{lf}) "modified Child law" sheath motion. Here the ion density is nearly constant for high frequency sheath motion, hence the stochastic heating expression calculated from the *uniform ion density* model given by Godyak [28], can be used here. For one sheath,

$$S_{stoc} = \frac{1}{2} m_e \bar{v}_e n u_{sh}^2 \tag{5.11}$$

where $\bar{v}_e$ is the mean electron thermal velocity and u_{sh} is the velocity amplitude of the plasma sheath boundary. For the two-step ion density model, replacing u_{sh} in equation (5.11) by $u_{sh} - u_{bh}$ and $n = n_{sh}$, we get

$$\begin{aligned} S_{stocDF} &= \frac{1}{2} m_e \bar{v}_e n_{sh} (u_{sh} - u_{bh})^2 \\ &= \frac{1}{2} m_e \bar{v}_e n_{sh} u_{sh}^2 \left(1 - \frac{n_{sh}}{n_{bh}}\right)^2 . \end{aligned} \tag{5.12}$$

Here we used the current continuity condition $n_{bh}u_{bh} = n_{sh}u_{sh}$. For the case of the low frequency cycle, at each phase $\phi_{lf} = \omega_{lf}\,t$, the high frequency electron oscillation occurs at the ion sheath density $n_{sh}(\phi_{lf})$ which is the modified Child law sheath density (detailed derivation in Lieberman [30]), given by equation (3.12). Thus

$$S_{stocDF} = \frac{1}{2} m_e \bar{v}_e \left\langle n_{sh}(\phi_{lf})(u_{sh}(\phi_{lf}) - u_{bh})^2 \right\rangle \tag{5.13}$$

Here, $u_{bh} = J_{hf}/(e\,n_{sm})$ and $u_{sh}(\phi_{lf}) = J_{hf}/[e\,n_{sh}(\phi_{lf})]$ are the velocity amplitudes of the high frequency bulk and sheath motion, respectively. Now we know from the current continuity condition

$$\frac{n_{sm}}{n_{sh}} = \frac{u_{sh}}{u_{bh}} \tag{5.14}$$

Putting equation (5.14) in equation (5.13), we obtain

$$S_{stocDF} = \frac{1}{2} m_e \bar{v}_e n_{sm} u_{bh}^2 \left(\left\langle \frac{n_{sm}}{n_{sh}} \right\rangle + \left\langle \frac{n_{sh}}{n_{sm}} \right\rangle - 2 \right). \tag{5.15}$$

Using equation (3.12), we get

$$\left\langle \frac{n_{sm}}{n_{sh}(\phi_{lf})} \right\rangle = \langle 1 - H_{lf} N(\phi_{lf}) \rangle = 1 + \frac{\pi H_{lf}}{4}. \tag{5.16}$$

Here

$$H_{lf} = \frac{J_{lf}^2}{\pi \varepsilon_0 k_B T_e n_{sm} \omega_{lf}^2} \tag{5.17}$$

and $N(\phi_{lf})$ is give by equation (3.13). The velocity amplitude of the low frequency bulk motion is defined by $u_{bl} = J_{lf}/(e\,n_{sm})$. Inserting equation (5.16) in (5.15), we obtain

$$S_{stocDF} = \frac{1}{2} m_e \bar{v}_e n_{sm} u_{bh}^2 F(H_{lf}) \tag{5.18}$$

where

$$F(H_{lf}) = \frac{\pi H_{lf}}{4} - 1 + \frac{1}{\pi} \int_0^{\pi} \frac{d\phi}{1 - H_{lf} N(\phi_{lf})}. \tag{5.19}$$

In the above equation (5.19), the last integral can be solved numerically. A good parametric fit is

$$F(H_{lf}) \approx \frac{H_{lf}(1+\pi H_{lf}/4)}{H_{lf}+2.2} \tag{5.20}$$

So equation (5.18) can be re-written in terms of high frequency and low frequency contribution, as follows

$$S_{stocDF} = \underbrace{\frac{1}{2}m_e\bar{v}_e\frac{J_{hf}^2}{e^2 n_{sm}}}_{\textbf{High Frequency Portion}} \times \underbrace{\left(1+\frac{\pi}{4}H_{lf}\right)\left(\frac{H_{lf}}{H_{lf}+2.2}\right)}_{\textbf{Low Frequency Portion}} \tag{5.21}$$

The above expression makes clear that in DF-CCP, the stochastic heating is the product of both high and low frequency processes rather than the additive effect of two single frequency processes individually. Again, neglecting the bulk oscillation by setting $u_{bh} = 0$ in equation (5.13), which gives the upper limit of stochastic heating, S_{stocUL}, we get

$$S_{stocUL} = \frac{1}{2}m_e\bar{v}_e\left\langle n_{sh}(\phi_{lf})u_{sh}^2(\phi_{lf})\right\rangle \tag{5.22}$$

By putting the value of u_{sh} from equation (5.14) into equation (5.22), we obtain

$$S_{stocUL} = \frac{1}{2}m_e\bar{v}_e n_{sm}u_{bh}^2\left\langle\frac{n_{sm}}{n_{sh}}\right\rangle \tag{5.23}$$

Now put equation (5.16) in the above equation (5.23), the final expression for the upper limit of stochastic heating in the dual-frequency case is

$$S_{stocUL} = \frac{1}{2}m_e\bar{v}_e n_{sm}u_{bh}^2\left(1+\frac{\pi H_{lf}}{4}\right) \tag{5.24}$$

Finally, normalized stochastic heating for dual frequency CCP, $\zeta(H_{lf})$ can be obtained by dividing equation (5.18) by equation (5.24), is following

$$\zeta(H_{lf}) \equiv \frac{S_{stocDF}}{S_{stocUL}} = \frac{F(H_{lf})}{1+\pi H_{lf}/4} \approx \frac{H_{lf}}{H_{lf}+2.2} \tag{5.25}$$

It is important to note that equation (5.25) looks like equation (3.17), since the dual-frequency stochastic heating model developed by Kawamura *et al.*[1]

is an extension of the single frequency stochastic heating model developed by Kaganovich *et al.* [91].

Another model based on fluid equations was developed by Turner *et al.* [187] to calculate stochastic heating for DF-CCP. In this article, it is shown that the stochastic heating yielded by the superposition of two currents with low and high frequencies is much larger than the effect of either acting alone[187]. These results are in contradiction with Kim *et al.* [185] which predicts an additive affect. Heating yielded by fluid model in the dual-frequency case is given by

$$S_{stocT} = \frac{\pi}{16} m_e n_{sm} \bar{\nu}_e (u_{bl}^2 + 1.1 u_{bh}^2) F_T(H_{lf}) \tag{5.26}$$

Neglecting the contribution of the velocity amplitude of the low frequency bulk motion, u_{bl}, we get

$$S_{stocT} \approx \frac{1.1\pi}{16} m_e n_{sm} \bar{\nu}_e u_{bh}^2 F_T(H_{lf}) \tag{5.27}$$

where the function F_T is estimated by a parametric fit, shown below

$$F_T(H_{lf}) = \frac{36 H_{lf}}{55 + H_{lf}} \tag{5.28}$$

Finally the normalized stochastic heating can be written by dividing equation (5.27) by (5.24)

$$\zeta_T(H_{lf}) \equiv \frac{S_{stocT}}{S_{stocUL}} \approx \frac{4.95\pi H_{lf}}{(55 + H_{lf})(1 + \pi H_{lf}/4)} \tag{5.29}$$

5.4 Simulation Results

Kawamura *et al.* [1] used a mobile ion particle-in-cell simulation in an argon plasma to benchmark the dual-frequency analytical model (discussed in the previous section) for stochastic heating. Here dual-frequency discharges were driven by current

$$J_{rf}(t) = J_{hf}\, sin\, \omega_{hf} t + J_{lf}\, sin\, \omega_{lf} t \tag{5.30}$$

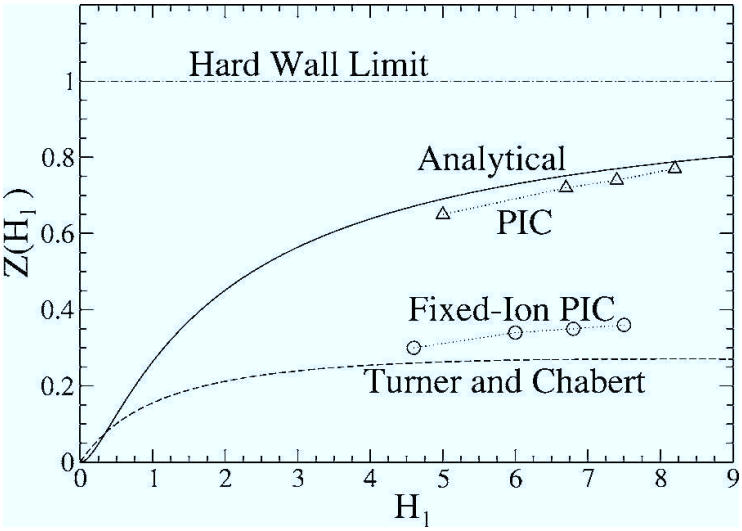

Figure 5.5: *This figure shows the variation of normalized stochastic heating* $\zeta(H_{lf})$ $\equiv Z(H_l) \equiv S_{stocDF}/S_{stocUL}$ *versus* H_{lf} *as described in Kawamura et al. [1]. Mobile ion dual-frequency PIC data are shown as triangles here and analytical model given by equation (5.25) is indicated as a solid line. The upper hard wall limit is also shown as a dashed-dotted line at* $\zeta(H_{lf}) = 1$. *Turner and Chabert [187] fluid model and fixed-ion dual frequency PIC simulation (circles) results are also shown in this figure.*

where J_{hf}, J_{lf} are high and low current density amplitudes and ω_{lf}, ω_{hf} are applied low and high angular frequencies respectively. Controlling parameters for the dual-frequency case are J_{lf}, J_{hf}, ω_{lf}, ω_{hf}, T_e and n_{sm}. Parameters used by Kawamura *et al.* [1] for their PIC simulations are, $p = 15$ mTorr, $f_{hf} = 32$ MHz and $f_{lf} = 2$ MHz. The high and low current density amplitudes are varied from $J_{hf} = 8 - 16$ A/m^2 and $J_{lf} = 2 - 4$ A/m^2 respectively, so the ratio of $J_{hf}/J_{lf} = 4$ in each set of simulations. Electron temperature, $T_e = 2$ eV here. Equation (5.17) indicates that H_{lf} depends on J_{lf} and n_{sm}, so as J_{lf} increases from $2 - 4$ A/m^2 and n_{sm} varied from 5×10^{14} m^{-3} to 1.4×10^{15} m^{-3} simultaneously, H_{lf} varied from 5.0 to 8.2 . Kawamura *et al.* [1] results are reproduced here in figure (5.5). This figure describes the dependence of

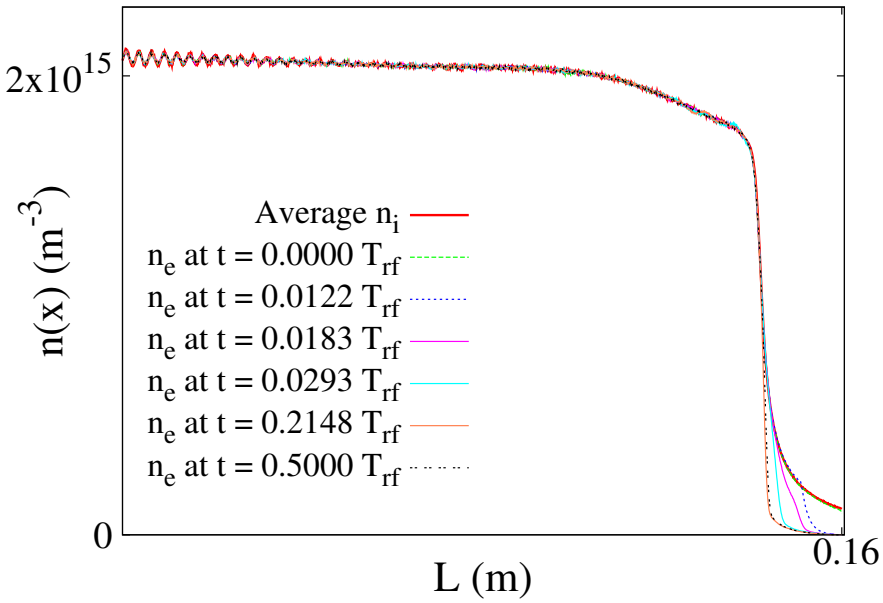

Figure 5.6: *Figure shows the averaged ion and snapshots of electron density profiles for the collisionless case in a dual-frequency PIC simulation. The solid line represents the average ion density and the electron density is represented by dashed lines during different times of an RF period i.e.* T_{rf}. *Conditions : argon gas,* $J_{lf} = 4\ A/m^2$, $J_{hf} = 32\ A/m^2$, $f_{lf} = 1.695\ MHz$, $f_{hf} = 27.12\ MHz$, $H = 6.77$, $T_e = 2.5\ eV$, $T_i = 0.03\ eV$ *at density* $2 \times 10^{15}\ m^{-3}$.

normalized stochastic heating $\zeta(H_{lf}) \equiv Z(H_l) \equiv S_{stocDF}/S_{stocUL}$ on H_{lf}. Here triangles show the mobile-ion dual frequency PIC data and the solid line represents the dual-frequency analytical model given by equation (5.25). Kawamura *et al.* concluded that simulation data (PIC results) are in good agreement with the analytical model given by equation (5.25). Here it is to be noted that the number of data points are rather small and a large simulation database needs to be generated, that might give improved formula for stochastic heating.

It is clear from the above discussion that there are six scaling parameters (*i.e.* J_{lf}, J_{hf}, ω_{lf}, ω_{hf}, T_e and n_{sm}) which control the stochastic heating. There are different ways to scale these parameters. We will discuss a few of them for

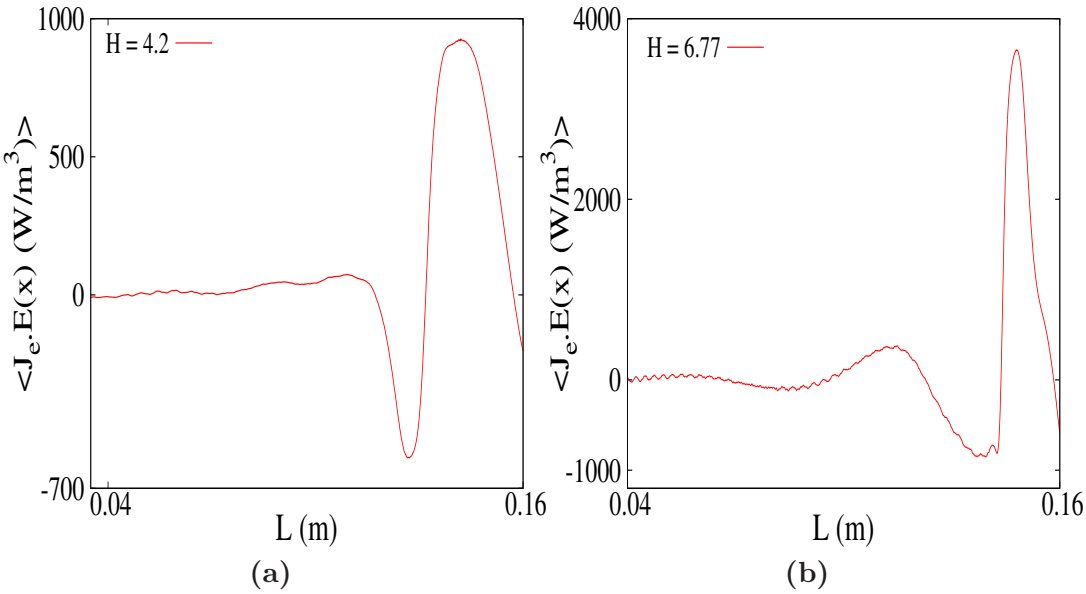

Figure 5.7: *Figure shows the self-consistent mobile-ion dual-frequency PIC simulation results for* $\langle J_e.E \rangle$ *in the collisionless case. (a) Conditions : argon gas,* $J_{lf} = 1.1$ A/m^2, $J_{hf} = 8.8$ A/m^2, $f_{lf} = 1.695$ MHz, $f_{hf} = 27.12$ MHz, $H_{lf} = 4.2$, $T_e = 2.5$ eV, $T_i = 0.03$ eV *at density* 3×10^{14} m^{-3}. *(b) Conditions : argon gas,* $J_{lf} = 4$ A/m^2, $J_{hf} = 32$ A/m^2, $f_{lf} = 1.695$ MHz, $f_{hf} = 27.12$ MHz, $H_{lf} = 6.77$, $T_e = 2.5$ eV, $T_i = 0.03$ eV *at density* 2×10^{15} m^{-3}.

the given applied *low* and *high RF* frequency, $f_{lf} = 1.695$ MHz and $f_{hf} = 27.12$ MHz, in our simulations and investigate the validation of analytical models. Here the PIC simulation is conducted for current-driven argon discharges in which both electrons and ions were moved by the usual PIC method. Plasma is considered collisionless here so there are no electron-neutral and ion-neutral collisions etc. The ions and electrons are loaded initially and evolve with time until the self-consistent steady-state configuration is achieved.

The first approach : In the first approach benchmarking of the analytical model is the same as that used by Kawamura *et al.* [1] where H_{lf} is calculated

by varying J_{lf} and n_{sm} simultaneously. The ratio of $J_{hf}/J_{lf} = 8$ here for each set of simulations. The parameter $\bar{v}_e$ did not vary much with J_{lf} and stayed nearly constant *i.e.* 1.058×10^6 m/s.

Figure (5.6) shows the averaged ion and the snapshots of electron density profile in the collisionless case. The ion sheath density $n_{sh}(x)$ decreases monotonically from a maximum density at the ion sheath boundary to a minimum of $n_w = 1.103 \times 10^{14}$ m^{-3} at the wall. This is for argon gas at $J_{lf} = 4$ A/m^2,

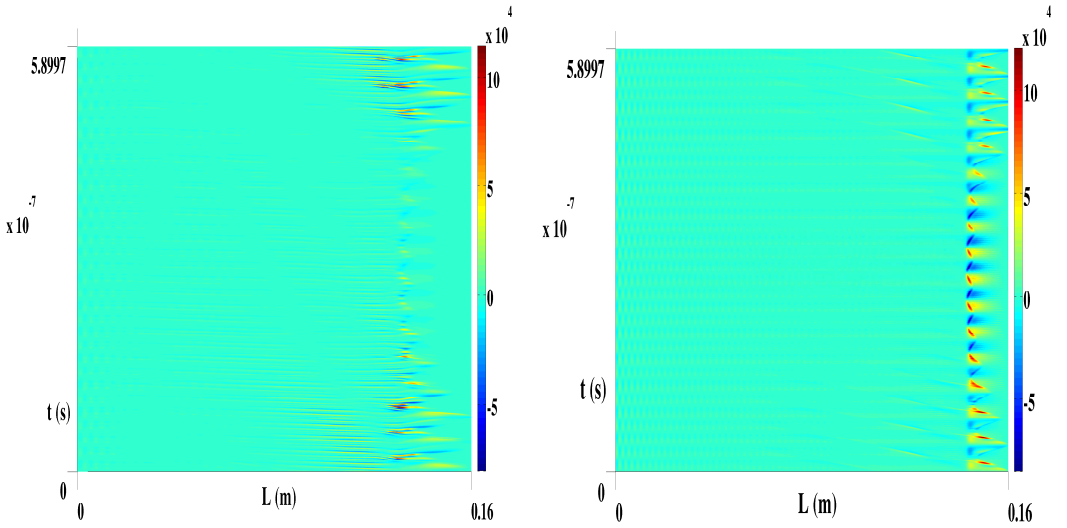

Figure 5.8: *Spatiotemporal profile of $J_e.E$ for density 3×10^{14} m^{-3} and 2×10^{15} m^{-3} in the collisionless case. (a) Conditions : argon gas, $J_{lf} = 1.1$ A/m^2, $J_{hf} = 8.8$ A/m^2, $f_{lf} = 1.695$ MHz, $f_{hf} = 27.12$ MHz, $H_{lf} = 4.2$, $T_e = 2.5$ eV, $T_i = 0.03$ eV at density 3×10^{14} m^{-3}. (b) Conditions : argon gas, $J_{lf} = 4$ A/m^2, $J_{hf} = 32$ A/m^2, $f_{lf} = 1.695$ MHz, $f_{hf} = 27.12$ MHz, $H_{lf} = 6.77$, $T_e = 2.5$ eV, $T_i = 0.03$ eV at density 2×10^{15} m^{-3}.*

$J_{hf} = 32$ A/m^2, $f_{lf} = 1.695$ MHz, $f_{hf} = 27.12$ MHz, $H_{lf} = 6.77$, $T_e = 2.5$ eV, $T_i = 0.03$ eV at the density 2×10^{15} m^{-3}. In this figure, a very weak *plasma*

wave propagation can also be observed at the sheath edge. These waves are the result of the progressive failure of quasi-neutrality at the electron sheath edge. This phenomena will be discussed later.

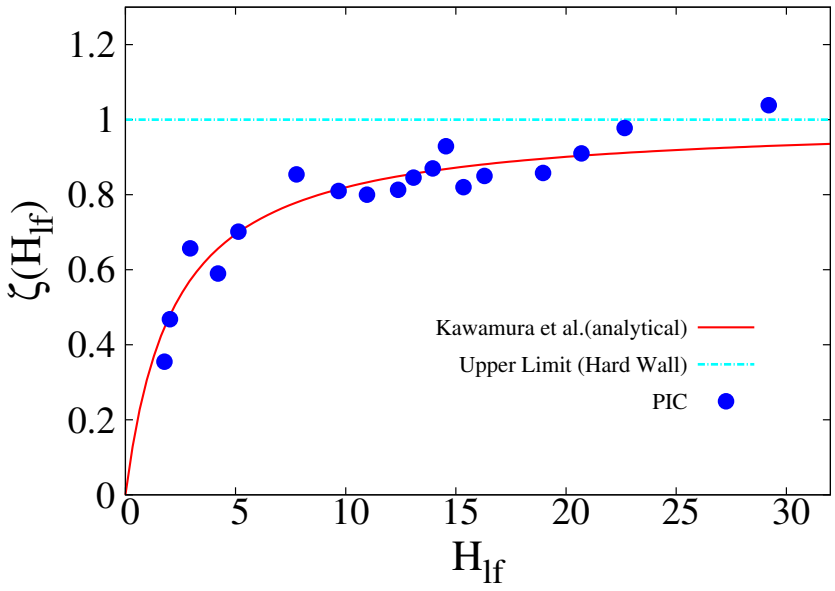

Figure 5.9: *Normalized stochastic heating* $\zeta(H_{lf}) \equiv S_{stocDF}/S_{stocUL}$ *from the PIC simulation (circles), and the dual-frequency analytical model given by Kawamura et al. [1] (solid line). The hard wall upper limit is also indicated (dashed line). Conditions : argon gas,* $f_{lf} = 1.695$ *MHz,* $f_{hf} = 27.12$ *MHz,* $T_e = 2.5$ *eV*, $T_i = 0.03$ *eV*.

The power deposition calculated by PIC simulation needs to be compared with that predicted by the dual-frequency analytical model given by Kawamura *et al.* [1]. Figure (5.7) shows the time-averaged local heating rate $\langle J_e.E \rangle$ for $H_{lf} \approx 4.2$ and 6.77 for the *density* of 3×10^{14} m^{-3} and 2×10^{15} m^{-3} respectively. Figure (5.8) shows the spatiotemporal profile of full $J_e.E$ for the same cases. The stochastic heating phenomenon occurs near the sheath edge.

Figure (5.9) shows the variation of normalized stochastic heating $\zeta(H_{lf}) \equiv S_{stocDF}/S_{stocUL}$ with respect to H_{lf}. The PIC simulation (circles) results are

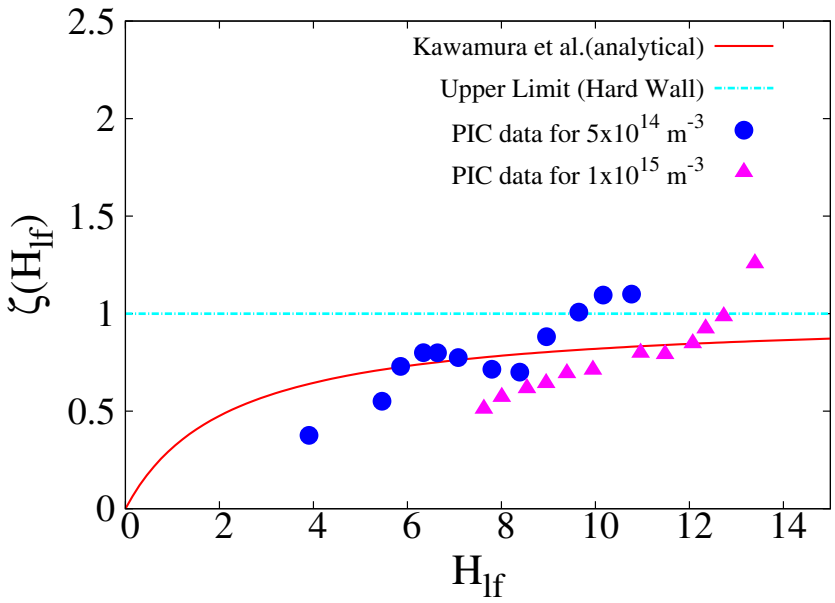

Figure 5.10: *Normalized stochastic heating* $\zeta(H_{lf}) \equiv S_{stocDF}/S_{stocUL}$ *from the PIC simulation for two different densities i.e.* $5 \times 10^{14}\ m^{-3}$ *and* $1 \times 10^{15}\ m^{-3}$. *The dual-frequency analytical model given by Kawamura et al. [1] is represented by solid line. The hard wall upper limit is also shown in graph (dashed line). Conditions : argon gas,* $f_{lf} = 1.695\ MHz$, $f_{hf} = 27.12\ MHz$, $T_e = 2.5\ eV$, $T_i = 0.03\ eV$.

compared with the dual-frequency analytical model given by Kawamura *et al.* [1] which is the extension of the single-frequency model given by Kaganovich *et al.* [91]. Here $\zeta(H_{lf})$ is given by equation (5.25) and the hard wall upper limit having $\zeta(H_{lf}) = 1$ (dashed line) is also indicated. Here the current drive amplitudes are varied from $J_{lf} = 0.5 - 11.12$ A/m^2 and $J_{hf} = 4.0 - 88.96$ A/m^2 at the corresponding densities of $n_{sm} \approx 1.1 \times 10^{14} - 4 \times 10^{15}$ m^{-3}. So the ratio of $J_{hf}/J_{lf} = 8$ here. It is clear from the figure that the PIC data fairly agrees with the dual-frequency analytical model given by Kawamura *et al.* [1] for a large range of H_{lf} *i.e.* $H_{lf} \approx 1.77 - 29.2$.

The second approach : In the second approach the stochastic heating is

investigated by keeping the density constant and varying the ratio of J_{hf}/J_{lf}, by changing the lower current density amplitude J_{lf}. We have investigated this point for two different densities *i.e.* 5×10^{14} m^{-3} and 1×10^{15} m^{-3}. The electron temperature T_e is 2.5 eV and the ion temperature is at nearly room temperature *i.e.* $T_i = 0.03$ eV. The parameter $\bar{v}_e = 1.058 \times 10^6$ m/s stayed approximately constant. The applied lower and upper frequencies are 1.695 MHz and 27.12 MHz respectively.

In figure (5.10), the normalized stochastic heating $\zeta(H_{lf}) \equiv S_{stocDF}/S_{stocUL}$ from the mobile-ion PIC simulations for two different densities, 5×10^{14} m^{-3} and 1×10^{15} m^{-3} is compared to the dual-frequency analytical model given by Kawamura *et al.* [1] which is the extension of the single-frequency model given by Kaganovich *et al.* [91]. Here $\zeta(H_{lf})$ is given by equation (5.25) and the hard wall upper limit having $\zeta(H_{lf}) = 1$ (dashed line) is also indicated. In figure (5.10), circles and triangles show the normalized stochastic heating calculated at densities 5×10^{14} m^{-3} and 1×10^{15} m^{-3} respectively. This graph indicates that the range of H_{lf} which fairly agree with the dual-frequency analytical model given by Kawamura *et al.* [1] is 5.8 - 9.0 and 9.4 - 12.35 for densities of 5×10^{14} m^{-3} and 1×10^{15} m^{-3} respectively. In each case after the upper critical limit of H_{lf} (in which the analytical model agrees with simulation) the stochastic heating increases rapidly. The following conclusions can be made from the above discussion:

1. At constant density the simulation results agree with the dual-frequency analytical model given by Kawamura *et al.* [1] for a certain range of H_{lf}.

2. For lower density, the dual-frequency analytical model given by Kawamura *et al.* [1] agrees with simulation results for lower values of H_{lf}. Similarly, for higher density, the dual-frequency analytical model agrees with simulation results for higher values of H_{lf} respectively.

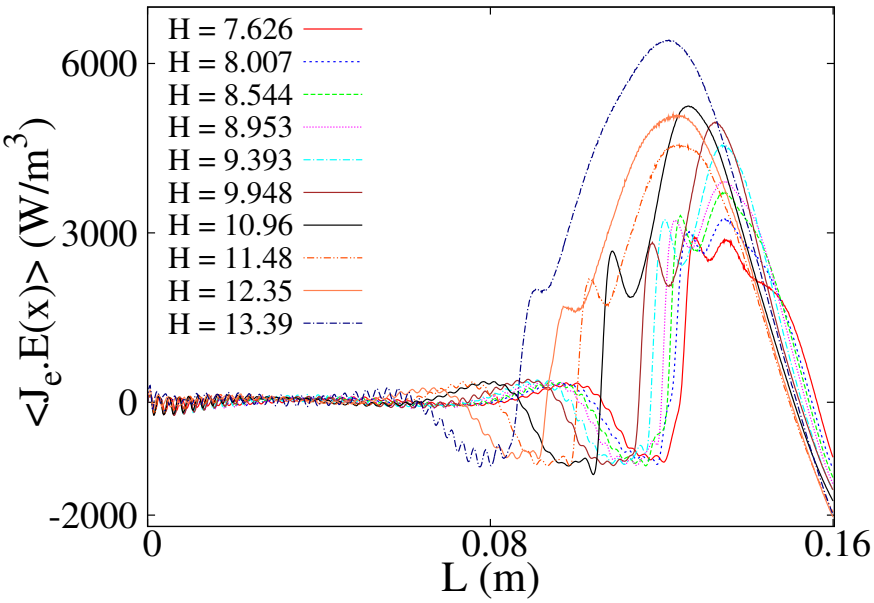

Figure 5.11: *Figure shows the self-consistent mobile-ion dual-frequency PIC simulation results for* $\langle J_e.E \rangle$ *in the collisionless case. Conditions : argon gas,* $J_{lf} = 2.7-3.6$ A/m^2, $J_{hf} = 26.4$ A/m^2, $f_{lf} = 1.695$ MHz, $f_{hf} = 27.12$ MHz, $H_{lf} = 7.6 - 13.4$, $T_e = 2.5$ eV, $T_i = 0.03$ eV *at density* 1×10^{15} m^{-3}.

Now we will study the specific case of 1×10^{15} m^{-3} in detail. Figure (5.11) shows the time-averaged local heating rate $\langle J_e.E \rangle$. Here by varying J_{lf} from 2.7 A/m^2 to 3.6 A/m^2, H_{lf} changes from 7.6 to 13.4. The current density amplitude for higher frequency (J_{hf}) is constant here *i.e.* 26.4 A/m^2. This figure shows that for the value of $H_{lf} > 12.35$, stochastic heating increases rapidly. Here 12.35 is the upper critical limit of H_{lf}.

We have studied carefully the case $H_{lf} = 13.39$ and observed the signature of ion reflection here, as we encountered in the single-frequency case. The rapid increase in heating is related to this ion reflection phenomena. Figure (5.12) shows the trajectory of ions in velocity phase space for the case of $J_{lf} = 3.6$ A/m^2 and $J_{hf} = 26.4$ A/m^2. Here the positive velocity indicates direction towards

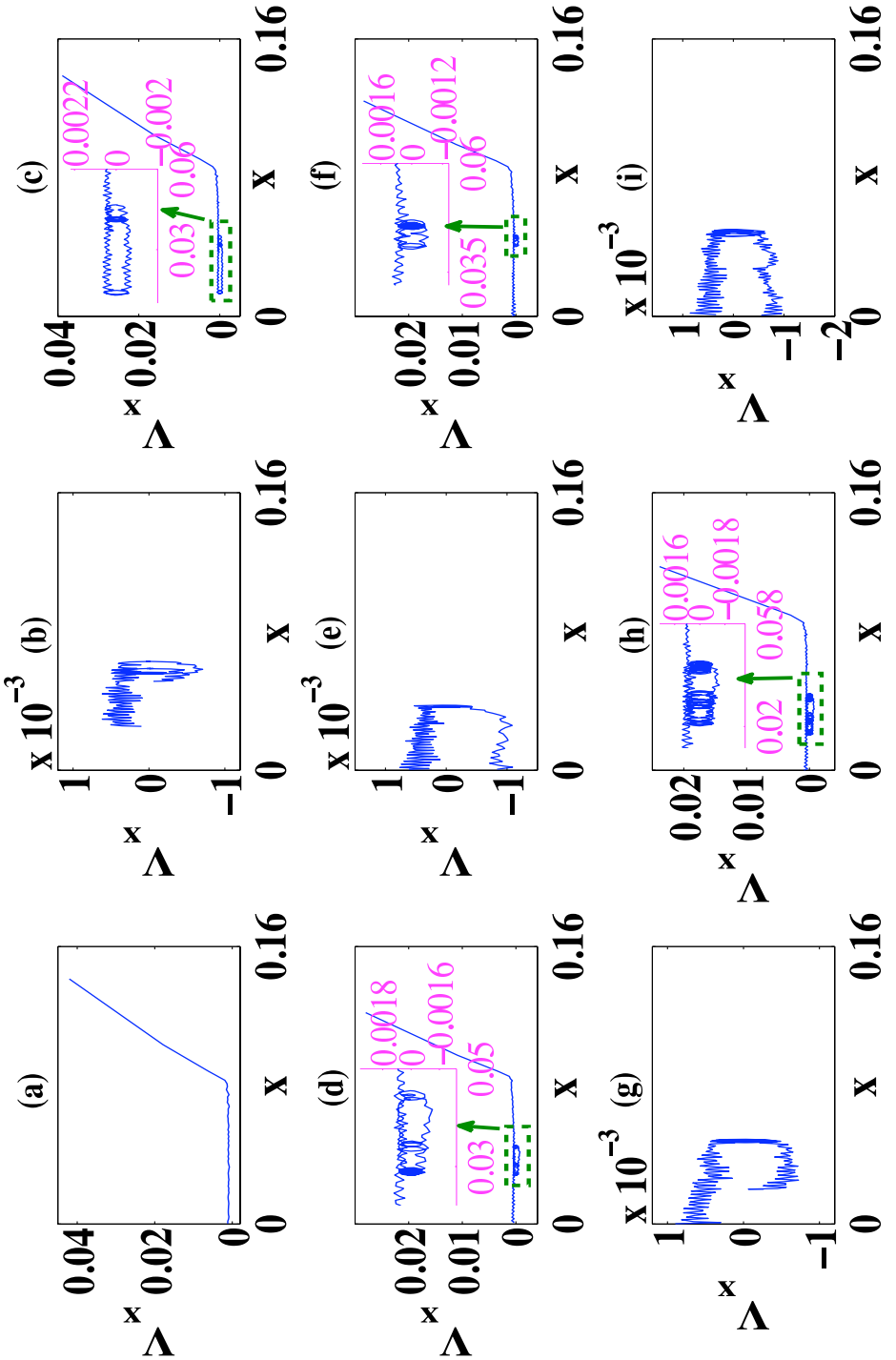

Figure 5.12: *Trajectories of ions in velocity phase space. Conditions: argon gas,* $J_{lf} = 3.6\ A/m^2$, $J_{hf} = 26.4\ A/m^2$, $T_e = 2.5\ eV$, $T_i = 0.03\ eV$, $f_{lf} = 1.695\ MHz$, $f_{hf} = 27.12\ MHz$.

the sheath (or electrode) and a negative velocity indicates direction towards the bulk plasma *i.e.* opposite to the sheath. The ion motion is collisionless within the sheath and ions are accelerated by the sheath electric field is a basic assumption of the dual-frequency analytical model. In the dual-frequency PIC simulation, the trajectory of a few thousand ions are saved, out of which few ion trajectories show the signature of the reflection of ions.

In figure (5.12), case (a) shows that ions propagate towards the sheath without any deflection in bulk plasma, enter inside the sheath and finally hit the electrode. The majority of ions in the PIC simulation show this type of behaviour. Case (b), (e), (g) and (i) show that the ions travel towards the sheath and reflect back at some point. These cases indicate that ions slow down while approaching the sheath region, stop for a while (trajectory is flat at edge) and finally reflect back towards the bulk plasma. However, case (e) and (i) indicate that ions move outside the simulation region and case (b) and (g) show that ions remain in the simulation region after reflection. Case (c), (d), (f) and (h) demonstrate that ions move towards the sheath and reflect back at some point. After travelling a certain distance inside the bulk (opposite to sheath), the velocity becomes positive and it again moves towards the sheath and finally accelerates and hits the electrode. It is to be noted that the distance travelled inside the bulk after reflection is different in these cases. The only reason behind this ion reflection is the presence of field reversals at the time of low frequency sheath expansion and collapse.

Figure (5.13) shows the spatiotemporal profile of the electric field for $J_{lf} = 3.6$ A/m^2 and $J_{hf} = 26.4$ A/m^2. In this figure, the field reversal regions are clearly observed at multiple times near to the sheath region. The most probable reason for this field reversal is electron fluid compression and rarefaction while the high frequency sheath expands and collapses. Here because of ion reflection

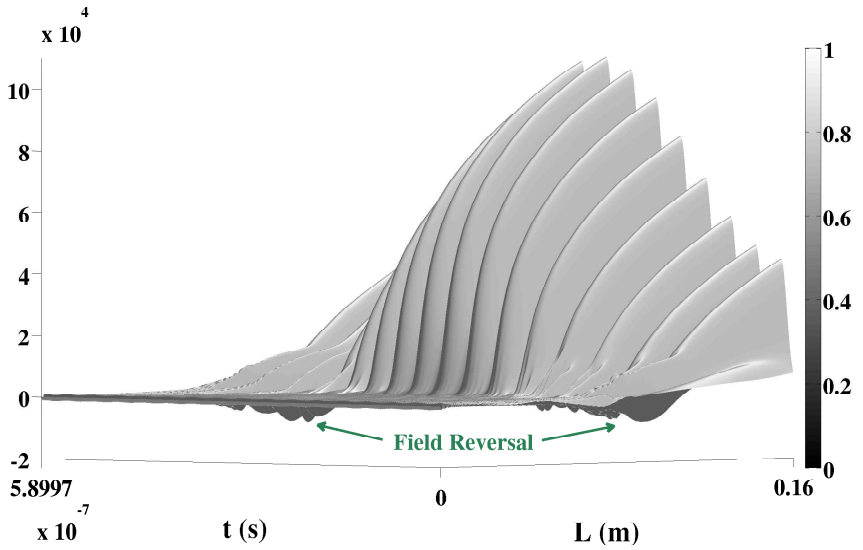

Figure 5.13: *Spatiotemporal profile (surface plot) of electric field. Conditions: argon gas,* $J_{lf} = 3.6\ A/m^2$, $J_{hf} = 26.4\ A/m^2$, $T_e = 2.5\ eV$, $T_i = 0.03\ eV$, $f_{lf} = 1.695\ MHz$, $f_{hf} = 27.12\ MHz$ *at the density of* $1 \times 10^{15}\ m^{-3}$.

phenomena, there is a density jump in bulk plasma from 1×10^{15} m^{-3} to 1.27×10^{15} m^{-3}. Figure (5.14) shows the time average ion and snapshots of electron density profile for $J_{lf} = 3.3$ A/m^2 and $J_{lf} = 3.6$ A/m^2 at density 1×10^{15} m^{-3}. It is clear from figure (5.14), the density jumps from 1×10^{15} m^{-3} to 1.27×10^{15} m^{-3} when J_{lf} is varied from 3.3 A/m^2 to 3.6 A/m^2 at a constant J_{hf} *i.e.* 26.4 A/m^2.

Equation (5.24) shows that the stochastic heating is a function of density. However this density is either considered as bulk density or density at the ion sheath-plasma boundary. The density distribution inside the simulation region significantly changed for these two cases. The calculated ion density at the sheath edge by knowing the n_w (ion density at the electrode) is 7.657×10^{14} m^{-3} for $J_{lf} = 3.6$ A/m^2. For $J_{lf} = 3.6$ A/m^2 the analytical and simulation stochastic heating is $S_{stocUL} = 196.835$ W/m^2 and $S_{stocDF} = 247.3466$ W/m^2

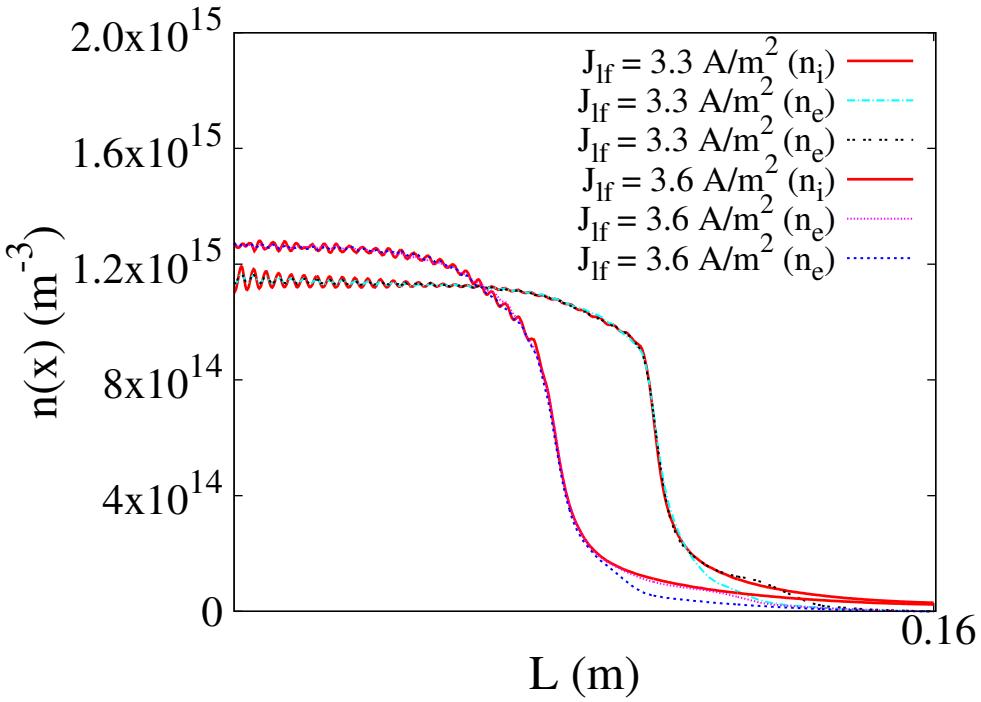

Figure 5.14: *Averaged ion and snapshots of electron density profile for* $J_{lf} = 3.3$ A/m^2 *and* $J_{lf} = 3.6$ A/m^2 *at density* 1×10^{15} m^{-3}. *The value of* $J_{hf} = 26.4$ A/m^2 *is the same in both cases. Conditions: argon gas,* $T_e = 2.5$ eV, $T_i = 0.03$ eV, $f_{lf} = 1.695$ MHz, $f_{hf} = 27.12$ MHz.

respectively. On the other hand, analytical stochastic heating calculated by considering bulk density is $S_{stocUL} = 75.6478\ \mathrm{W/m^2}$. These results are tabulated in table (5.1). Here the heating predicted by the dual-frequency analytical

Table 5.1: *Stochastic heating (both analytical and simulation) for the case of* $J_{lf} = 3.6$ A/m^2 *and* $J_{hf} = 26.4$ A/m^2 *at density* 1×10^{15} m^{-3}.

J_{lf}	$(S_{stocUL})_{theory}$ (ion sheath edge density)	$(S_{stocUL})_{theory}$ (bulk density)	$(S_{stocDF})_{simulation}$
3.6 A/m^2	196.835 W/m^2	75.6478 W/m^2	247.3466 W/m^2

model is significantly less than the heating calculated by PIC simulation because of the density jump inside the bulk plasma. Normally the analytical stochastic heating does not vary much either taking ion density from the bulk plasma or at the ion-sheath edge. Here, due to a density jump inside the bulk plasma the velocity amplitude of the bulk motion $u_{bh} = J_{hf}/en_0$ and H_{lf} drops significantly and as a result the analytical heating prediction is significantly reduced. Here n_0 is bulk density.

This indicates that the electron dynamics of the heating mechanism is different for these cases where a strong field reversal region is present and ion reflection phenomenon comes into the picture. So the existing dual-frequency analytical model is not applicable here.

5.5 Heating in Dual-Frequency is Much Higher than the Frequencies Acting Alone

In the literature, Turner and Chabert [187] reported that the stochastic heating yielded by the superposition of low and high frequency currents (*i.e.* J_{lf} and J_{hf}) with different frequencies (*i.e.* f_{lf} and f_{hf}) can be much higher than the heating produced by either low current (J_{lf}) with low frequency (f_{lf}) or high current (J_{hf}) with high frequency (f_{hf}) acting alone. However these results are contrary to the additive effect reported by Kim *et al.* [185]. The physical parameters used here are $T_e = 2.5$ eV, $T_i = 0.003$ eV, $f_{lf} = 1.695 \times 10^6$ Hz, $f_{lf} = 27.16 \times 10^6$ Hz and the density is 6×10^{14} m^{-3}. The low and high current density amplitudes are $J_{lf} = 2.1$ A/m^2 and $J_{hf} = 16.8$ A/m^2 respectively. Our PIC simulation indicates that the stochastic heating may be significantly enhanced when two frequencies act together.

Figure (5.15) shows the PIC simulation results which represents the stochas-

tic heating produced by the combined frequencies compared to the heating produced by each frequency effect separately. For the cases when only lower

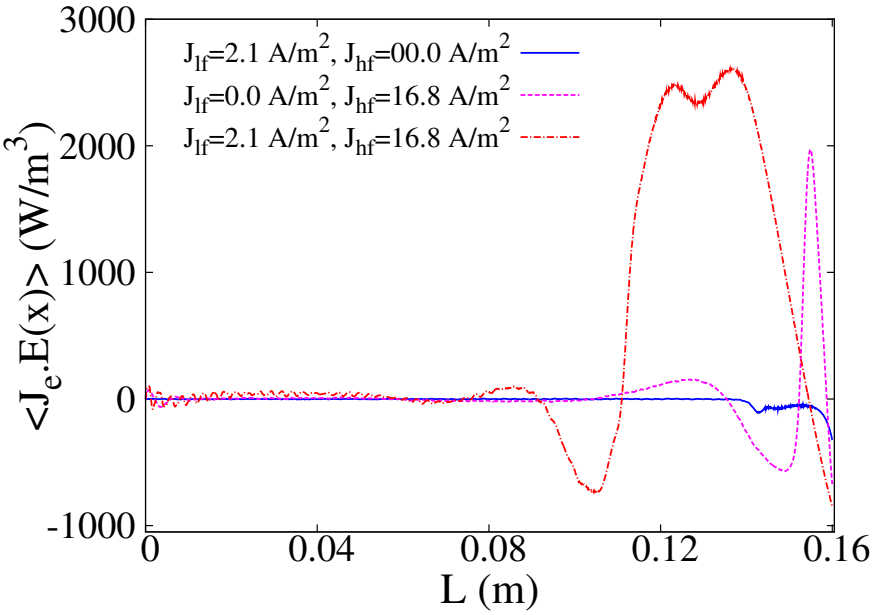

Figure 5.15: *Time averaged stochastic heating* $< J_e.E >$ *for three different cases i.e. the two frequencies acting separately and both acting together. Conditions : argon gas,* $J_{lf} = 2.1\ A/m^2$, $J_{hf} = 16.8\ A/m^2$ $f_{lf} = 1.695\ MHz$, $f_{hf} = 27.12\ MHz$, $T_e = 2.5\ eV$, $T_i = 0.03\ eV$ *at density* $6 \times 10^{14}\ m^{-3}$.

frequency and higher frequency are applied separately, the stochastic heating is $S_{lf} = -1.5963$ W/m^2 and $S_{hf} = 5.4698$ W/m^2 respectively. The negative heating (in case of low frequency) shown is due to the large number of electrons being lost to the electrode, this results in a loss of power that is greater than the stochastic heating at the sheath edge. When both frequencies act together, the stochastic heating produced is $S_{stocDF} = 71.457$ W/m^2. It is clear here that the heating produced in the case when both frequencies act together is much higher (nearly 10 times) than the frequencies acting separately.

Turner and Chabert [187] reported this effect for the case of fixed ions and

the numerical results are also compared with the heating predicted by the analytical fluid model.

5.6 Wave Phenomena in DF-CCPs

In chapter 4, we discussed the evidence of electron plasma wave phenomena in single frequency capacitive discharges. The evidence of strong plasma waves is also observed in the simulation of dual-frequency capacitive discharges. However we did not find any published literature related to the wave phenomena in the dual-frequency capacitive discharges. Here we describe PIC simulation results of current-driven argon discharges in which both the electrons and the ions were moved by usual PIC methods. These results are for the collisionless case so electron and ion collisions are not included here. These PIC simulations are for the case where the applied lower and higher frequency is $f_{lf} = 1.695$ MHz and $f_{hf} = 27.12$ MHz respectively. So the ratio of $f_{hf}/f_{lf} = 16$ here. The electron temperature T_e is 2.5 eV and the ion temperature T_i is 0.03 eV.

Figure (5.16) shows the spatiotemporal profile of electron density for 2×10^{15} m^{-3}. It is clear that high frequency is overlapped 16 times on the lower frequency. Here the RF current drive amplitudes are $J_{lf} = 4$ A/m^2 and $J_{hf} = 32$ A/m^2, so the ratio of $J_{hf}/J_{lf} = 8$. Figure (5.17) shows the averaged ion and snapshots of electron density profiles at the positions (a) to (p) as indicated in figure (5.16). Very weak plasma waves are present at the time of the low frequency sheath expansion (*i.e.* from (a)-(d)) and the time of low frequency sheath collapse (*i.e.* from (m)-(p)). There are no waves from (e) to (l) cases. From figure (5.16), it is simple to explain : For the cases from (a)-(d) and (m)-(p), the overlapping of high frequency on low frequency is significant and the quasi-neutrality breaks down at the time of high frequency sheath expansion that causes the launching of waves near to the sheath edge. The following

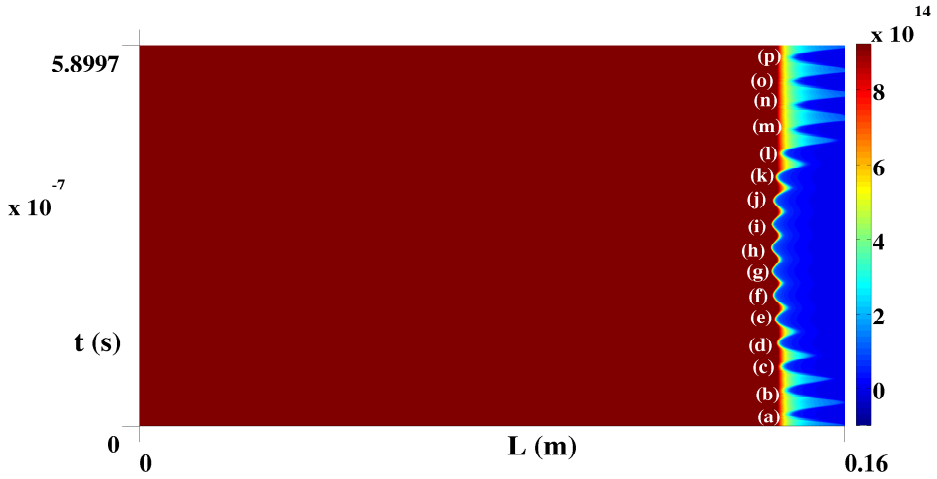

Figure 5.16: *A spatiotemporal profile of electron density. Conditions : argon gas,* $J_{lf} = 4\ A/m^2$, $J_{hf} = 32\ A/m^2$ $f_{lf} = 1.695\ MHz$, $f_{hf} = 27.12\ MHz$, $T_e = 2.5\ eV$, $T_i = 0.03\ eV$ *at the density of* $2 \times 10^{15}\ m^{-3}$.

conclusions can be made from figure (5.17):

1. The waves launch from near the sheath edge at multiple times during an *RF* period. On the other hand, in the single frequency case, wave launch from near the sheath edge at one particular time only during the *RF* cycle.

2. The waves are clear when the modulation of high frequency on low frequency is strong *i.e.* from (a)-(d) and (m)-(p).

3. The amplitude of these waves are weak.

4. No waves occur during the full expansion of the low frequency sheath *i.e.* from (e)-(l).

High amplitude plasma waves are also observed in dual-frequency capacitively coupled plasma discharges. Figure (5.18) shows the spatiotemporal profile of

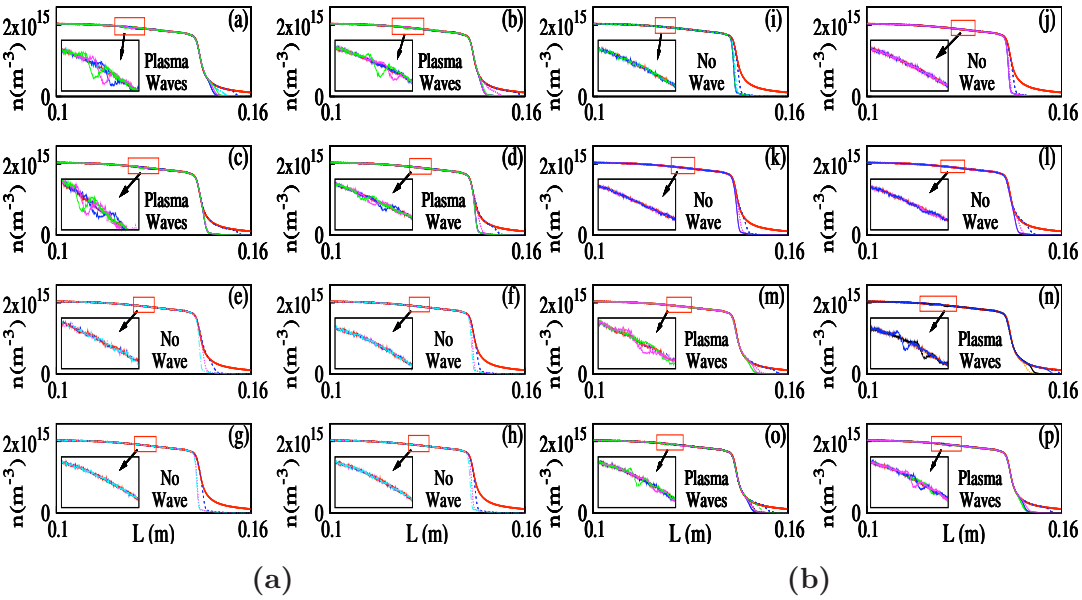

Figure 5.17: *The averaged ion and snapshots of electron density profiles at the positions (a) to (p) as indicated in figure (5.16). (a) From the positions of 'a-h' (b) From the positions of 'i-p'.*

electron density for 3×10^{14} m^{-3}. The higher frequency (27.12 MHz) is overlapped 16 times on the lower frequency (1.695 MHz) here. The *RF* current density amplitudes of lower frequency and higher frequency are $J_{lf} = 1.1$ A/m^2 and $J_{hf} = 8.8$ A/m^2, so the ratio of $J_{hf}/J_{lf} = 8$ here.

Figure (5.19) shows the snapshots of electron density profiles and time averaged ion density profile near to the positions (a) to (p) as indicated in figure (5.18). Very high amplitude plasma waves are present at the time of low frequency sheath expansion *i.e.* from (a)-(c). From position (d) onwards the wave amplitude damps down and there are no waves from (e) to (l). The wave again appear at position '(m)' and the wave amplitude is significant from (n) to (p) at the time of low frequency sheath collapse. From figure (5.18), it is clear that for the cases from (a)-(d) and (m)-(p), the overlapping of high frequency on

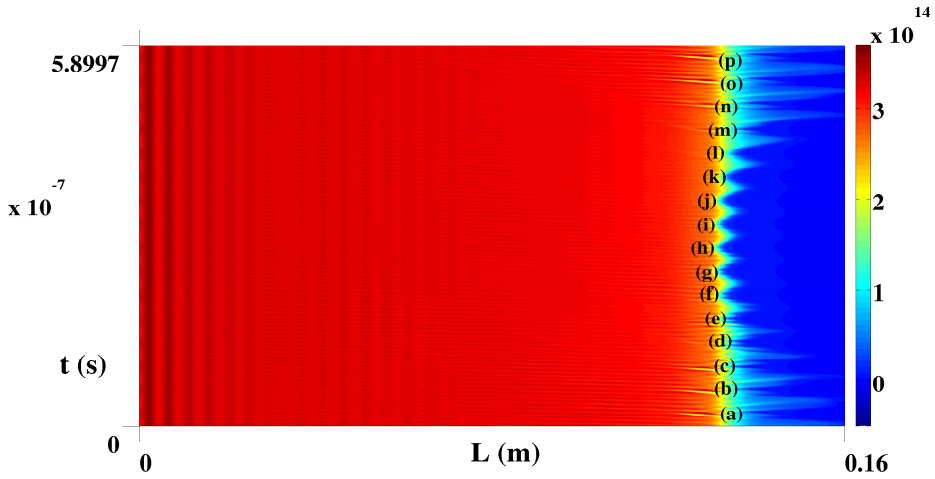

Figure 5.18: *A spatiotemporal profile of electron density. Conditions : argon gas,* $J_{lf} = 1.1\ A/m^2$, $J_{hf} = 8.8\ A/m^2$ $f_{lf} = 1.695\ MHz$, $f_{hf} = 27.12\ MHz$, $T_e = 2.5\ eV$, $T_i = 0.03\ eV$ *at the density of* $3 \times 10^{14}\ m^{-3}$.

low frequency is significant and the quasi-neutrality breaks down at the time of high frequency sheath expansion that causes the launching of waves near the sheath edge. The following conclusions can be made from figure (5.19):

1. The high amplitude waves launch from near to the sheath edge at multiple times during an RF period.

2. The waves have high amplitude when the modulation of high frequency on low frequency is strong *i.e.* from (a)-(c) and (n)-(p).

3. No waves occur during the full expansion of the low frequency sheath *i.e.* from (e)-(l).

4. The waves do not penetrate deep inside the bulk plasma.

In the single-frequency case (chapter 4), we have discussed the presence of a field reversal region near to the sheath edge and the trapping of the electrons near to this field reversal region at the time of sheath expansion. It is also discussed

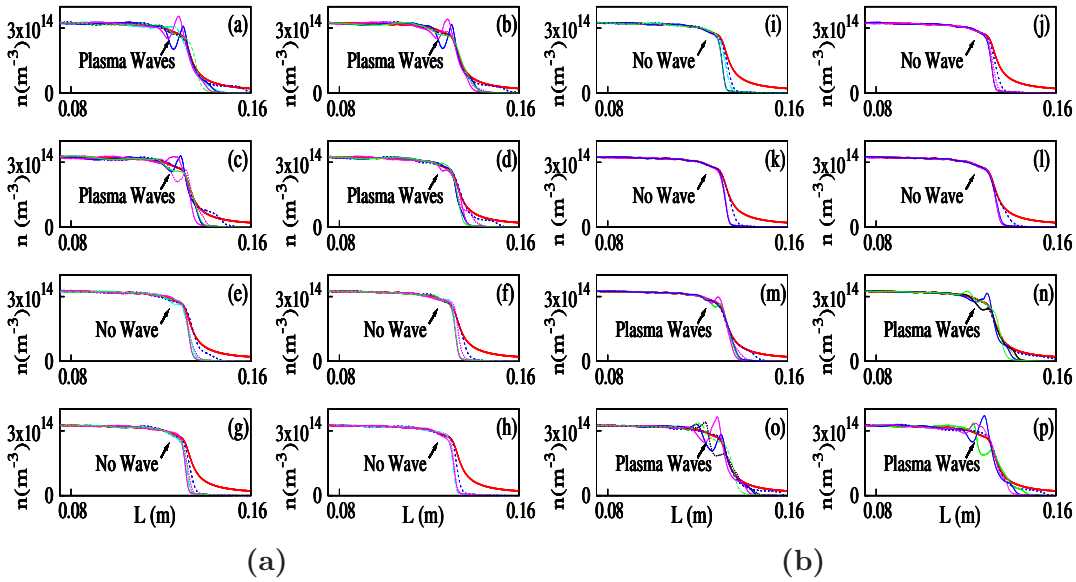

Figure 5.19: *The averaged ion and snapshots of electron density profiles at the positions (a) to (p) as indicated in figure (5.18). (a) From the positions of 'a-h' (b) From the positions of 'i-p'.*

that because of this trapping and untrapping of electrons, wave phenomena occur near to the sheath region. In the dual-frequency case, we will investigate the reason of the waves launching at multiple times during an RF period near to the sheath edge.

Figure (5.20) shows the spatiotemporal profile of the electric field. Here H_{lf} is 4.2 for the corresponding $J_{lf} = 1.1$ A/m^2 and $J_{hf} = 8.8$ A/m^2. The field reversal regions are present when the high frequency sheath expands and collapses during the low frequency sheath expansion and retreats towards the electrode. In the dual-frequency case the field reversal is present at multiple times near to the sheath edge. Figure (5.21) shows the surface plot of electric field. In this figure, the field reversal regions are clearly observed at multiple times near to the sheath region. The most probable reason for this field reversal

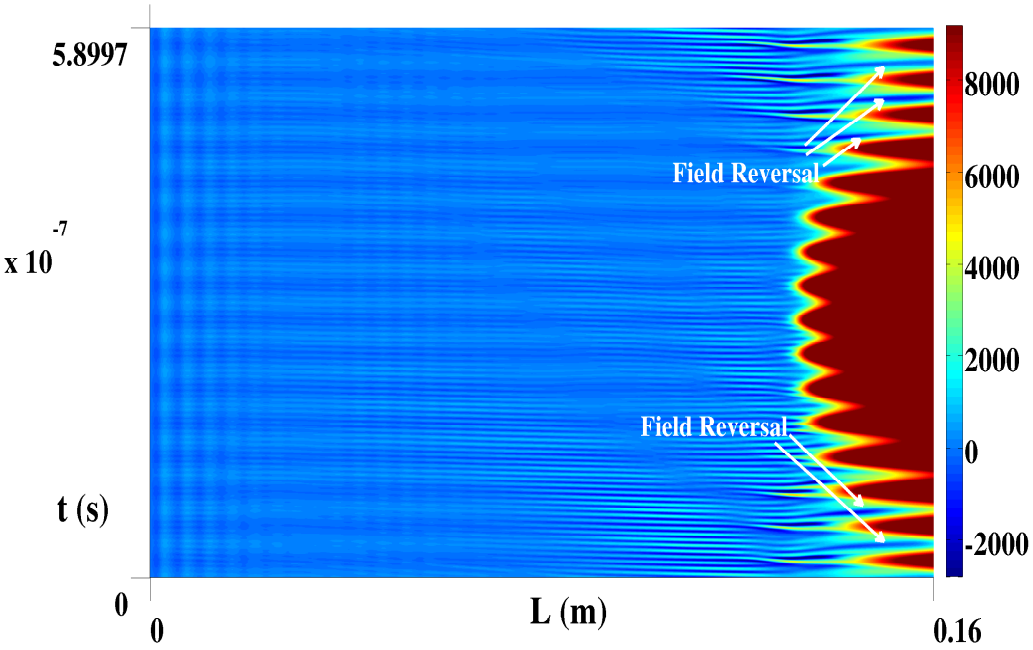

Figure 5.20: *A spatiotemporal profile of electric field. This figure demonstrate very high electric field inside the sheath and a weak field in the bulk plasma. The field reversal regions can be observed during the low frequency sheath expansion and when the low frequency sheath retreats towards the electrode. Conditions : argon gas,* $J_{lf} = 1.1\ A/m^2$, $J_{hf} = 8.8\ A/m^2$, $f_{lf} = 1.695\ MHz$, $f_{hf} = 27.12\ MHz$, $T_e = 2.5\ eV$, $T_i = 0.03\ eV$ *at the density of* $3 \times 10^{14}\ m^{-3}$.

is electron fluid compression and rarefaction while the high frequency sheath expands and collapses.

Our simulation indicates the trapping of electrons near to the field reversal regions. Figure (5.22) shows the spatiotemporal profile of charge separation $(n_e - n_i)$. It indicates the trapping of electrons near to the sheath edge when the higher frequency sheath expands and collapses at the time when the low frequency sheath expands and retreats towards the electrode. These are the same regions where field reversals are present. In steady state these trapped electrons

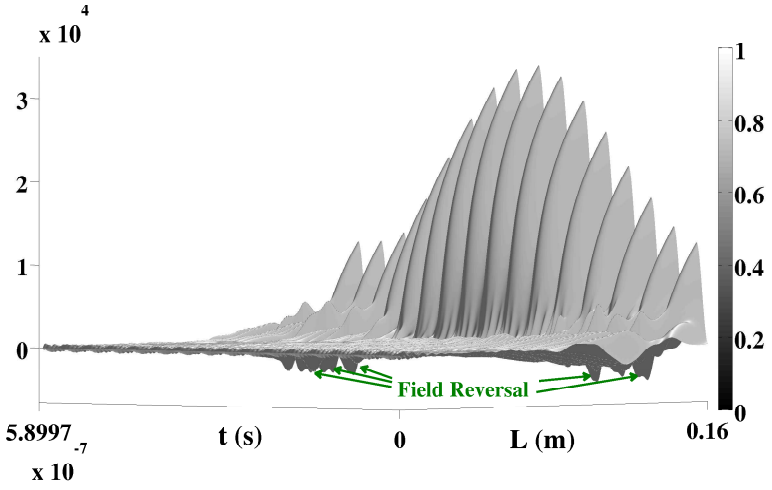

Figure 5.21: *A surface plot of electric field which indicates a strong field reversal region. The field reversal regions can be observed during the high frequency sheath expansion at multiple times during an RF period of low frequency. Conditions : argon gas,* $J_{lf} = 1.1\ A/m^2$, $J_{hf} = 8.8\ A/m^2$, $f_{lf} = 1.695\ MHz$, $f_{hf} = 27.12\ MHz$, $T_e = 2.5\ eV$, $T_i = 0.03\ eV$ *at the density of* $3 \times 10^{14}\ m^{-3}$.

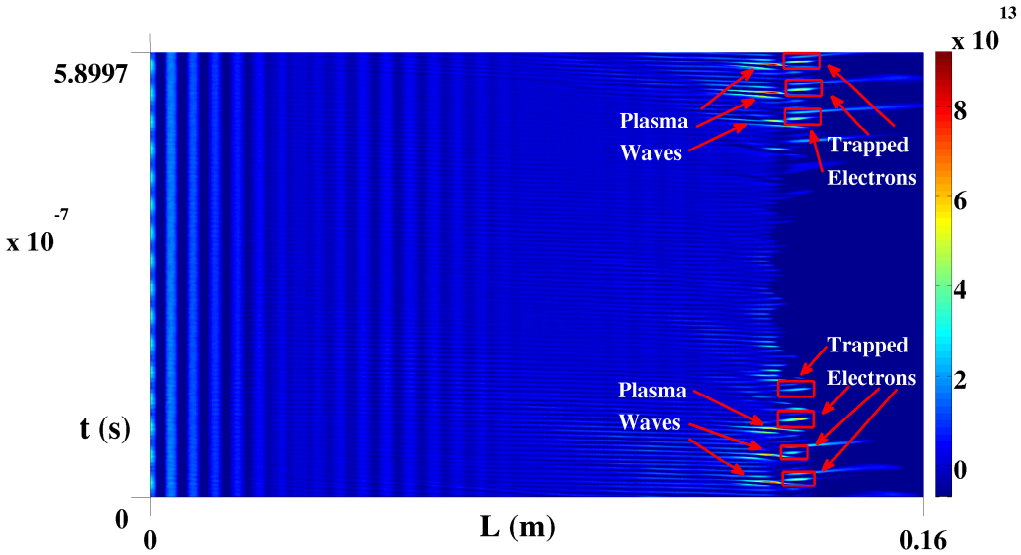

Figure 5.22: *A spatiotemporal profile of charge separation* $(n_e - n_i)$. *The electrons are trapped near to the field reversal regions at multiple times of low frequency RF period. Conditions : argon gas,* $J_{lf} = 1.1\ A/m^2$, $J_{hf} = 8.8\ A/m^2$, $f_{lf} = 1.695\ MHz$, $f_{hf} = 27.12\ MHz$, $T_e = 2.5\ eV$, $T_i = 0.03\ eV$ *at the density of* $3 \times 10^{14}\ m^{-3}$.

are significant in number, and the trapping and untrapping of these electrons at these field reversal positions during the high frequency sheath expansion causes electron plasma wave formation near to the sheath region. Electron plasma waves are clearly visible at multiple times near to the sheath edge in figure (5.22).

5.7 Temporal Evolution of Wave: Evidence of Electron Plasma Wave

In this section we will investigate the oscillations which appear at the sheath edge. These oscillations are either some travelling random oscillations or electron plasma waves, and need to be identified. The frequency of these waves are calculated here by investigation of the temporal evolution of electron density. Two different cases *i.e.* weak amplitude plasma waves and strong amplitude plasma waves, will be discussed here.

Figure (5.23) shows the temporal evolution of electron density at the different positions inside the simulation region, for the same initial conditions as shown in figure (5.16) and (5.17). Figure (5.23) clearly shows the propagation of waves in the electron density profile. The input parameters are : argon gas, $J_{lf} = 4$ A/m^2, $J_{hf} = 32$ A/m^2 $f_{lf} = 1.695$ MHz, $f_{hf} = 27.12$ MHz, $T_e = 2.5\ eV$, $T_i = 0.03$ eV, and the density is 2×10^{15} m^{-3}. In figure (5.23), the x-axis shows time and can be converted to real time (in *second*), by multiplying numbers on the *x-axis* by a factor of $\Delta t \sim 7.201788348 \times 10^{-11}$. This temporal evolution indicates the following points:

1. The waves are present during the expansion and collapse of low frequency, f_{lf}.

2. The wave amplitude is weak ($\sim 5.2 \times 10^{13}$ m^{-3}) and due of this, waves

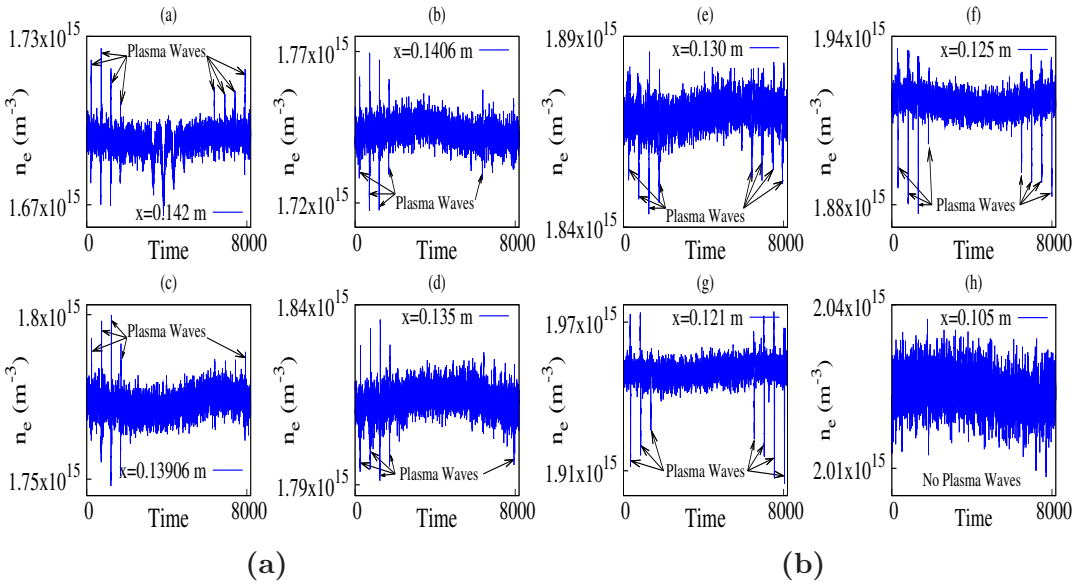

Figure 5.23: *Figure shows temporal evolution of electron density (n_e) in the collisionless case. Temporal evolution of n_e at eight different positions inside the simulation region are plotted here. In figure (a), four positions, starting from the sheath edge towards the bulk plasma are plotted. Waves starts at position 0.142 m near to the sheath edge. In figure (b), the next four positions in the direction of bulk plasma are plotted. The waves finally disappear at 0.105 m. Conditions : argon gas, $J_{lf} = 4$ A/m^2, $J_{hf} = 32$ A/m^2, $f_{lf} = 1.695$ MHz, $f_{hf} = 27.12$ MHz, $H_{lf} = 6.77$, $T_e = 2.5$ eV, $T_i = 0.03$ eV at density 2×10^{15} m^{-3}.*

are hard to observe in the spatial profile of electron density (fig (5.17)). However in temporal evolution waves are clearly observed.

3. The waves starts from near the sheath region at position 0.142 m, and propagate towards bulk and finally disappear near 0.105 m.

Figure (5.24) shows the zoomed part of waves at the position 0.142 m, as indicated in figure (5.23). The frequency of the wave can be calculated with the help of time period between "A" and "B", as shown in figure (5.24). The frequency

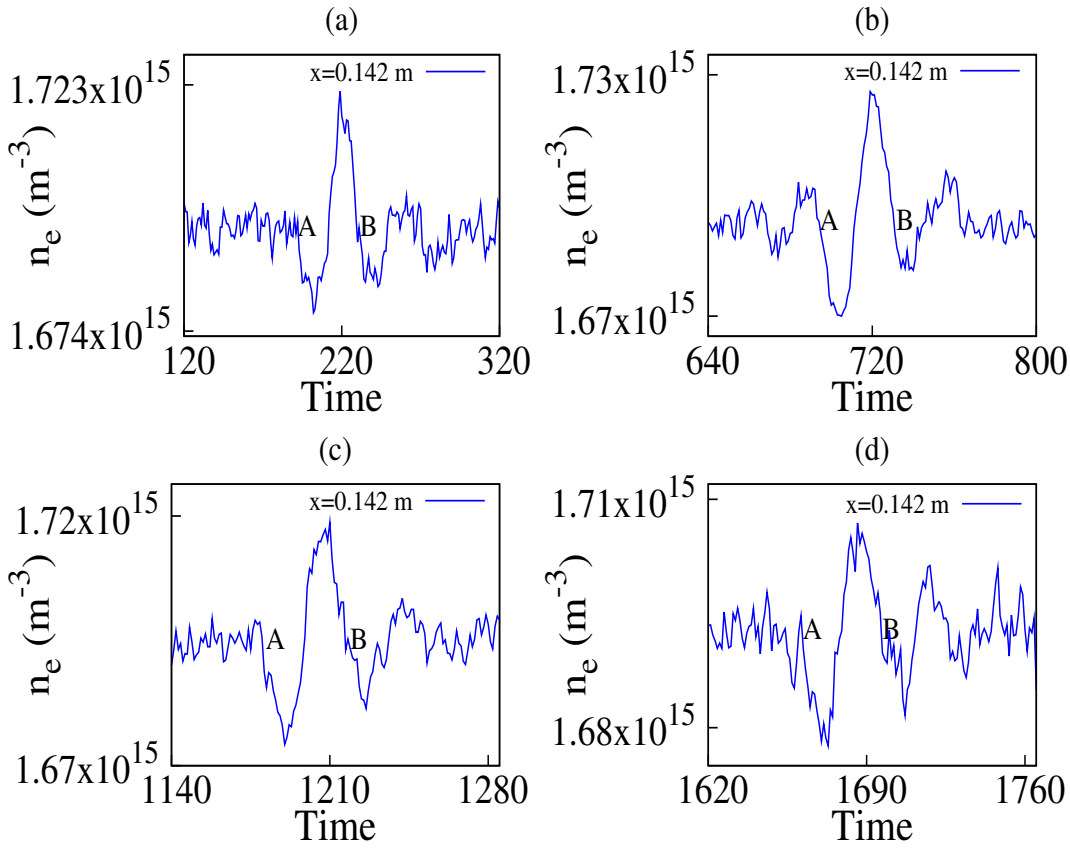

Figure 5.24: *Figure shows zoomed in figure of some waves, at the position 0.142 m, in temporal evolution of electron density n_e as indicated in figure (5.23)*

of the waves are :

- case (a) : $\omega_{wave} = 2.423\ GHz$.
- case (b) : $\omega_{wave} = 2.423\ GHz$.
- case (c) : $\omega_{wave} = 2.493\ GHz$.
- case (d) : $\omega_{wave} = 2.493\ GHz$.

The electron plasma frequency in simulation, $(\omega_{pe})_{sim}$, is 2.3193×10^9 Hz here. It is clear that wave frequency ω_{wave} is always either greater than or equal to $(\omega_{pe})_{sim}$ *i.e.* $\omega_{wave} \geq (\omega_{pe})_{sim}$.

In the above case, the amplitude of the waves is weak. However, we have observed very strong plasma waves in some cases. Figure (5.25) shows the tem-

poral evolution of electron density at the different positions inside the simulation region, for the same initial conditions as shown in figure (5.18) and (5.19). Figure (5.25) shows the propagation of waves in the electron density profile clearly. Here the x-axis shows time and can be converted to real time (in *second*), by multiplying numbers on the *x-axis* by a factor of $\Delta t \sim 2.880715348 \times 10^{-10}$. Here the wave amplitude is very strong and temporal evolution indicates the

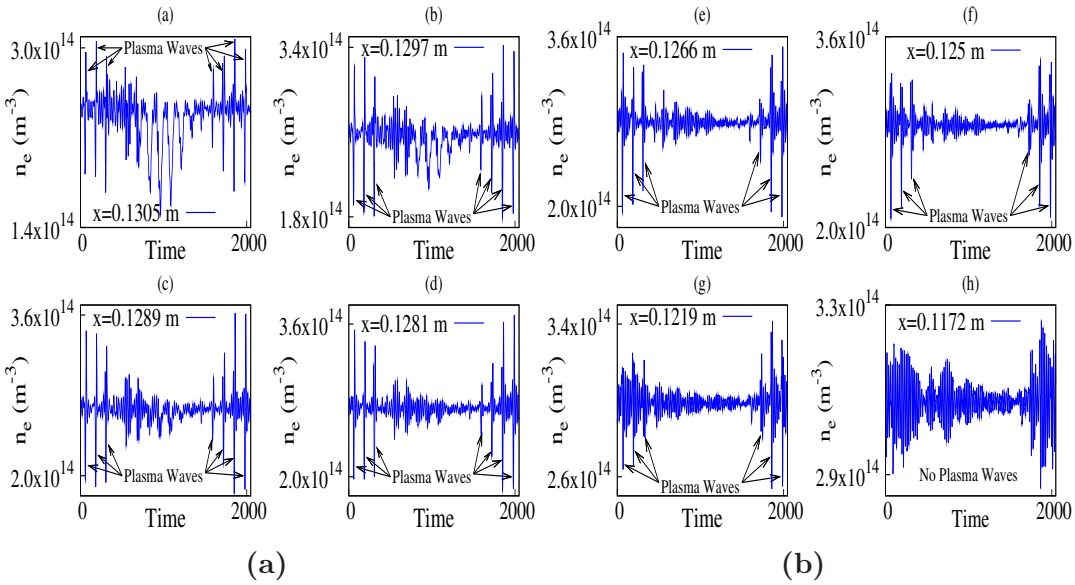

Figure 5.25: *Figure shows temporal evolution of electron density (n_e) in the collisionless case. The temporal evolution of n_e at eight different positions inside the simulation region are plotted here. In figure (a), four positions, starting from the sheath edge towards the bulk plasma are plotted. The waves starts at position 0.1305 m near to the sheath edge. In figure (b), the next four positions in the direction of bulk plasma are plotted. The waves finally disappear at 0.1172 m. Conditions : argon gas, $J_{lf} = 1.1\ A/m^2$, $J_{hf} = 8.8\ A/m^2$, $f_{lf} = 1.695\ MHz$, $f_{hf} = 27.12\ MHz$, $H_{lf} = 4.2$, $T_e = 2.5\ eV$, $T_i = 0.03\ eV$ at density $3 \times 10^{14}\ m^{-3}$.*

following points:

1. The waves are present during the expansion and collapse of low frequency, f_{lf}.

2. The wave amplitude is high ($\sim 1.6 \times 10^{14}$ m^{-3}) and due to this, waves are clearly observed in the spatial and temporal profile of electron density (fig (5.19)).

3. The waves starts from near to the sheath region at position 0.1305 m. It propagates towards the bulk plasma and finally disappears near 0.1172 m.

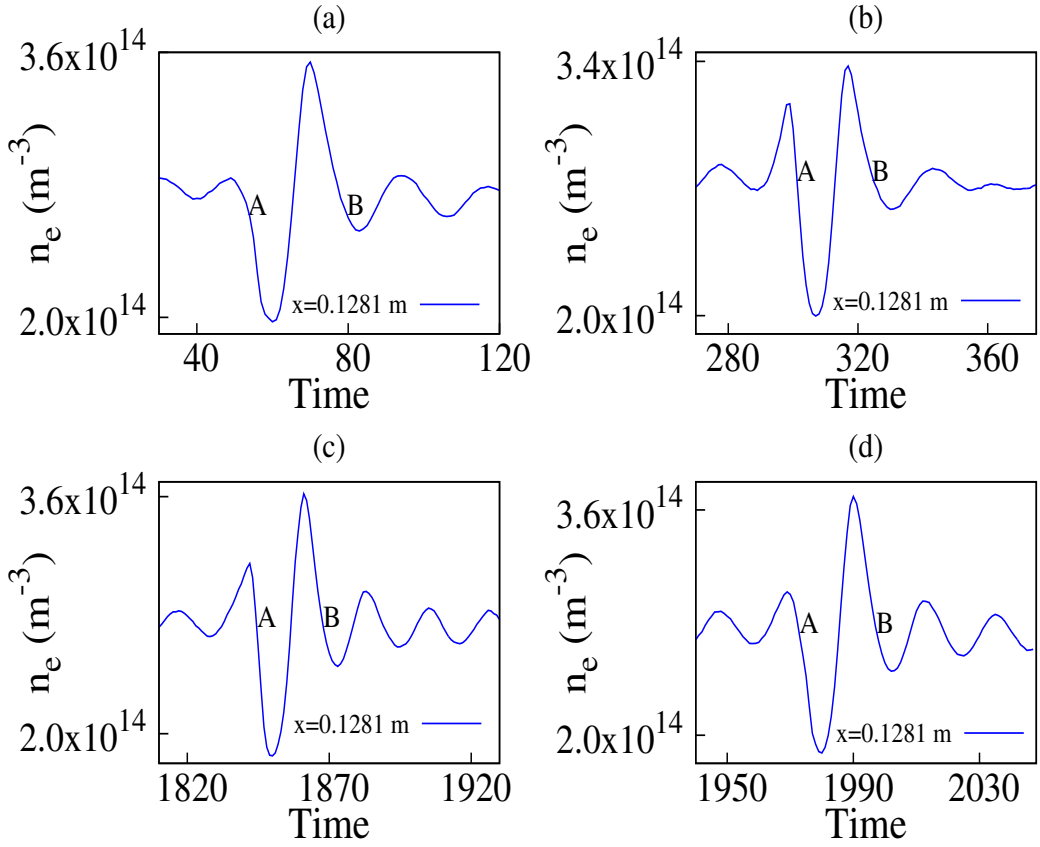

Figure 5.26: *Figure shows zoomed in figure of some waves, at the position 0.1281 m, in the temporal evolution of electron density n_e as indicated in figure (5.25).*

Figure (5.26) shows the zoomed part of waves at the position 0.1281 m, as

indicated in figure (5.25). The frequency of the waves can be calculated with help of time period between "A" and "B", as shown in the figure (5.26). The frequency of waves are :

- case (a) : $\omega_{wave} = 0.9088\ GHz.$
- case (b) : $\omega_{wave} = 0.9483\ GHz.$
- case (c) : $\omega_{wave} = 0.9483\ GHz.$
- case (d) : $\omega_{wave} = 0.9483\ GHz.$

The electron plasma frequency in simulation, $(\omega_{pe})_{sim}$, is 0.9097 GHz. It is clear that wave frequency ω_{wave} is always either greater than or equal to $(\omega_{pe})_{sim}$ *i.e.* $\omega_{wave} \geq (\omega_{pe})_{sim}$.

5.8 Summary

Using analytic and self-consistent particle-in-cell models, the electron dynamics inside a sheath region of a dual frequency RF capacitive discharge have been investigated in connection with the collisionless heating through the Fermi acceleration mechanism. Stochastic heating in dual-frequency is controlled mainly by six scaling parameters (*i.e.* J_{lf}, J_{hf}, T_e, ω_{lf}, ω_{hf} and n_{sm}). There are different ways of scaling these parameters and two different approaches are discussed here.

In the *first approach* benchmarking of the dual-frequency analytical model is the same as that used by Kawamura *et al.* [1] where H_{lf} is calculated by varying J_{lf} and n_{sm} simultaneously. However in the Kawamura *et al.* simulation, the number of data points are rather small *i.e.* $H \sim 5.0 - 8.2$. Present simulation results widen the range of $\mathbf{H}_{lf}$ *i.e.* $H_{lf} \sim 1.77 - 29.2$ which are in fair agreement with the dual-frequency analytical model given by Kawamura *et al.* [1] which is the extension of the single-frequency analytical model given by Kaganovich *et al.* [91]. Here the lower and higher frequency current drive amplitudes are varied

from $J_{lf} = 0.5 - 11.12$ A/m^2 and $J_{hf} = 4.0 - 88.96$ A/m^2 at the corresponding densities of 1.1×10^{14} - 4×10^{15} m^{-3} . Here the ratio of $J_{hf}/J_{lf} = 8$ for all set of simulations.

In the *second approach* the stochastic heating is studied by keeping density constant and by varying the ratio of J_{hf}/J_{lf}, by changing the lower current density amplitude J_{lf}. Stochastic heating at two different densities *i.e.* 5×10^{14} m^{-3} and 1×10^{15} m^{-3} has been investigated. At constant density the simulation results agree with the dual-frequency analytical model given by Kawamura *et al.* [1] in a certain range of H_{lf}. It is observed that H_{lf} is in fair agreement with the dual-frequency analytical model, given by Kawamura *et al.* [1], for the range of $5.8-9.0$ and $9.4-12.35$ at the densities of 5×10^{14} m^{-3} and 1×10^{15} m^{-3} respectively. The presence of field reversal regions at the time of low frequency sheath expansion and collapse is identified. The most probable reason for the field reversal regions at multiple times during an RF period is electron fluid compression and rarefaction while the high frequency expands and collapses. The signature of ion reflection is also observed above the upper critical limit of H_{lf} because of field reversal regions.

The stochastic heating produced by the combined frequencies, *i.e.* f_{lf} and f_{hf}, and heating produced by each frequency effect separately has been compared to the PIC simulation. Our PIC simulation indicates that the stochastic heating may be significantly enhanced when two frequencies act together.

The evidence of strong plasma waves is observed in the simulation of dual frequency capacitive discharges. The applied lower and higher frequency is $f_{lf} = 1.695$ MHz and $f_{hf} = 27.12$ MHz respectively, so the ratio of $f_{hf}/f_{lf} = 16$ here. It is clear that high frequency is overlapped 16 times on the lower frequency. The overlapping of high frequency on low frequency is significant at the time of low frequency sheath expansion and collapse. As a result, the

quasi-neutrality breaks down when the modulation of high frequency on low frequency is strong that causes the launching of waves near the sheath edge at multiple times during an RF period. It is also observed that the waves do not penetrate deep inside the bulk plasma. The spatiotemporal profile of electric field indicates the presence of strong field reversal regions near the sheath edge. The field reversal regions are present when the high frequency sheath expands and collapses during the low frequency sheath expansion and retreats towards the electrode. In the dual- frequency case the field reversal is present at multiple times near to the sheath edge. The most probable reason for this field reversal is electron fluid compression and rarefaction while the high frequency sheath expands and collapses (place where the modulation of high frequency on low frequency is significant). The profile of charge separation in PIC simulation also indicates the trapping of electrons near to the field reversal regions. In steady state these trapped electrons are significant, and the trapping and untrapping of electrons at these field reversal positions during the high frequency sheath expansion causes electron plasma wave formation near to the sheath region. Electron plasma waves are also clearly visible at multiple times near to the sheath edge.

The frequency of these waves are calculated here by investigation of temporal evolution of the electron density. This temporal evolution indicates that waves are present during the expansion and collapse of low frequency, f_{lf}. The frequency of these waves are calculated and it is clear that wave frequency ω_{wave} is always either greater than or equal to $(\omega_{pe})_{sim}$ i.e. $\omega_{wave} \geq (\omega_{pe})_{sim}$.

CHAPTER 6

Conclusion and Future Work

6.1 Conclusion

The objective of this research work is to stretch our understanding of the phenomena related with the sheaths present in capacitive discharges, and further enhance our capability to use plasmas adequately. The primary interest is to study the stochastic heating phenomenon in single and dual frequency capacitive discharges. The nature of the heating mechanism that provides the energy needed to sustain a plasma at low-pressure conditions in capacitively coupled discharges is discussed in this work. The particle-in-cell simulation technique is used here to model a current-driven, semi-infinite, 1-D plasma in contact with an electrode. To benchmark the analytical models and their assumptions, only the area near the sheath/presheath regions is modeled here. Inside the code, ionization is ignored as it is assumed that it is not important over a sheath length. The plasma is treated as being completely collisionless for most of the

results presented in this research work. However the code can handle the elastic scattering for the electrons and charge-exchange for the ions. A constant collision frequency is assumed in case of collisions.

A particular distribution function is assumed for each of the species present, to model a semi-infinite plasma which lies outside the simulation region. Drifting Maxwellians are assumed here for all of the species. Other distribution functions could be used. Again, simulations with a single ion species are studied here but more ion species could be included. Here for all sets of results, planar geometry is used but cylindrical and spherical geometry can be used by generalization of the method.

6.2 Study of Stochastic Heating by Scaling of Parameters in Single Frequency CCP Discharges

In collisionless case, the mechanism by which the electrons gain energy and are heated in the RF sheath is the motivation of this research work. With the help of analytical models and a self-consistent PIC code, the electron dynamics inside the sheath region of a single frequency RF capacitive discharge have been investigated in connection with stochastic heating through the Fermi acceleration mechanism. Four scaling parameters (*i.e.* $\tilde{J}_0$, T_e, ω_{rf} and n_{sm}) can control the stochastic heating. There are different ways to scale these parameters and three different approaches are discussed here:

- In the *first approach* benchmarking of the analytical model is the same as that used by Kawamura *et al.* [1] where H is calculated by varying $\tilde{J}_0$ and n_{sm} simultaneously. Present simulation results widen the range of **H**

i.e. $H \sim 0.6 - 18$ which are in fair agreement with the Kaganovich *et al.* model in this range. Analytical models do not account for electron loss at the electrode, so in order to compare the simulation results with analytical models, the contribution to the power per unit area by the electrons which are being lost at the electrode is excluded here. The results obtained indicate that the simulation data, which excludes the electron loss at an electrode, more closely approach the Lieberman model especially for lower values of H.

- In the *second approach* the stochastic heating is studied by keeping density constant and by varying the current density amplitude $\tilde{J}_0$. A range of different densities from 2×10^{14} m^{-3} to 1×10^{16} m^{-3} has been investigated. At constant density the simulation results agree with Kaganovich *et al.* [91] in a certain range of H. In each case after a upper critical limit of H (in which the analytical model agrees with simulation) the stochastic heating increases rapidly. The electron dynamics of the heating mechanism is different for these cases and present analytical formula for stochastic heating calculations need to be improved. Signature of ion reflection from near sheath region is also observed. The presence of field reversal near the sheath region at the time of sheath expansion is the main reason of ion reflection.

- In the *third approach* the effect of electron temperature T_e on stochastic heating for the density 5×10^{15} m^{-3} has been investigated. Here T_e is varied from $1.7 - 10$ eV. It is observed that H is in fair agreement with the Kaganovich *et al.* [91] model for the range 4 to 13.5, which is roughly the same as that observed for same density in the *second approach* for density 5×10^{15} m^{-3}. The presence of field reversal at the time of sheath expansion and signature of ion reflection from near sheath region is also

observed above the upper critical limit of H.

The average power per unit area scaling with frequency for a constant H is also studied in this work. Two different approaches are discussed here :

- In the *first approach*, the normalized stochastic heating S_{stoc}/S_{stocL} scaling with frequency ω_{rf}/ω_{pe} for two different values of H *i.e.* 5 and 7 is discussed here. For $H = 5$ the density is varied from $\sim 2 \times 10^{14}\ m^{-3}$ to $5 \times 10^{16}\ m^{-3}$ for the applied frequency $f_{rf} \approx 2 - 158\ MHz$. For $H = 7$ the density is varied from $2 \times 10^{14}\ m^{-3}$ to $1 \times 10^{17}\ m^{-3}$ for the applied frequency $f_{rf} \approx 2 - 180\ MHz$. Results show that the normalized stochastic heating versus ω_{rf}/ω_{pe} is almost constant in the range $\sim 0.032 - 0.079$ for $H = 5$ and $\sim 0.024 - 0.065$ for $H = 7$. So for $H = 5$, when $f_{rf}/f_{pi} < 7$ and for $H = 7$, when $f_{rf}/f_{pi} < 6$ the stochastic heating rapidly decreases.

- For the *second approach* H is kept constant by varying only $\tilde{J}_0$ at constant density n_{sm}. The normalized stochastic heating S_{stoc}/S_{stocL} is almost constant from $\omega_{rf}/\omega_{pe} \approx 0.022 - 0.065$ for $H = 7$ at a density of 5×10^{15} m^{-3} and $\omega_{rf}/\omega_{pe} \approx 0.023 - 0.058$ at a density of $1 \times 10^{16}\ m^{-3}$. So density change does not affect the result too much. For $\omega_{rf}/\omega_{pe} < 0.02$ the normalized stochastic heating decreases rapidly for both cases. Results for normalized stochastic heating with a correction term (electrons that are being lost at an electrode) are also shown here. On the other hand normalized stochastic heating is nearly constant $\sim 0.035 - 0.086$ for $H = 3.5$ and $\sim 0.022 - 0.056$ for $H = 7$ at density $1 \times 10^{16}\ m^{-3}$. Here $f_{rf} \approx 13 - 77$ MHz for $H = 3.5$ and $f_{rf} \approx 9 - 51\ MHz$ for $H = 7$. Heating decreases rapidly for $\omega_{rf}/\omega_{pe} < 0.035$ for $H = 3.5$ and $\omega_{rf}/\omega_{pe} < 0.02$ for $H = 7$. So roughly, when $f_{rf}/f_{pi} < 5.8$ for density $5 \times 10^{15}\ m^{-3}$ and $f_{rf}/f_{pi} < 6$ for density $1 \times 10^{16}\ m^{-3}$, the heating decreases rapidly. It is also noticeable that the correction term (electrons that are being lost at electrode)

is significant below $\omega_{rf}/\omega_{pe} < 0.04$ for $H = 3.5$ and $\omega_{rf}/\omega_{pe} < 0.02$ for $H = 7$. So the range in which the normalized stochastic heating is almost constant, changes for different H at the same density.

6.3 Study of Wave Phenomena in Single Frequency CCP Discharges

Another important point in this research is the existence of electron plasma waves near the plasma-sheath interface that has been observed and investigated in chapter 4. The electron plasma waves appear in the sheath vicinity because of the break down of quasi-neutrality due to an overshoot of high velocity electrons into the bulk plasma. The Landau damping mechanism by which the oscillating energy to be transferred to electron thermal energy is also discussed here. It is also noticed that the sheath structure is modified during the sheath expansion and can be seen in the spatiotemporal profile of electron density. The spatiotemporal profile of electric field shows the presence of strong reverse electric field near modified sheath region. The possible reason for this reversed electric field is compression and rarefaction of the electron fluid when the sheath expands and collapses. There is evidence of electron trapping near reverse field region in the charge separation profile. The trapping and untrapping of electrons during the expansion and collapse of the sheath causes the launching of waves from near the sheath region. The evidence of significant displacement current in this region is also observed.

Finally the temporal evolution of electron plasma waves is discussed. The frequency of the wave ω_{wave} is calculated and it is greater than or equal to ω_{pe}. This is evidence that these waves are electron plasma waves. The effect of electron elastic collisions on waves are also studied. The modified sheath region

near the sheath edge also disappears at high collision rates *i.e.* high pressure.

6.4 Study of Stochastic Heating and Wave Phenomena in Dual Frequency Capacitive Discharges

The electron dynamics inside the sheath region in dual-frequency capacitive discharges have been studied in connection with the stochastic heating through Fermi acceleration mechanism. Six parameters (*i.e.* J_{lf}, J_{hf}, T_e, ω_{lf}, ω_{hf} and n_{sm}) can control the stochastic heating in dual-frequency analytical model given by Kawamura *et al.* [1]. We can scale these parameters in different ways and two different approaches are discussed here.

- In the *first approach* benchmarking of the dual-frequency analytical model is the same as that used by Kawamura *et al.* [1] where H_{lf} is calculated by varying J_{lf} and n_{sm} simultaneously. However in her case the number of data points are rather small (*i.e.* 5-8.2). The present research work widen the range of H_{lf} (*i.e.* 1.77-29.2) which is fairly agree with the dual-frequency analytical model given by Kawamura *et al.* [1]. For present approach the lower and higher frequency current drive amplitudes are varied from $J_{lf} = 0.5 - 11.12$ A/m^2 and $J_{hf} = 4.0 - 88.96$ A/m^2 at the corresponding densities of 1.1×10^{14} - 4×10^{15} m^{-3} . Here the ratio of $J_{hf}/J_{lf} = 8$ for all set of simulations.

- In the *second approach* the stochastic heating is studied by keeping density constant and by varying the ratio of J_{hf}/J_{lf}, by changing the lower current density amplitude J_{lf}. Here for two different densities *i.e.* 5×10^{14} m^{-3} and 1×10^{15} m^{-3} the stochastic heating has been investigated. For

constant density case, the simulation results agree with the dual-frequency analytical model given by Kawamura *et al.* [1] in a certain range of H_{lf}. It is observed that H_{lf} is in fair agreement with the dual-frequency analytical model for the range of $5.8 - 9.0$ and $9.4 - 12.35$ at the densities of 5×10^{14} m^{-3} and 1×10^{15} m^{-3} respectively. The presence of field reversal regions at the time of low frequency sheath expansion and collapse is identified. The signature of ion reflection is also observed above the upper critical limit of H_{lf} because of field reversal regions.

The evidence of strong plasma waves is observed in the simulation of dual frequency capacitive discharges. The applied lower and higher frequency is $f_{lf} = 1.695$ MHz and $f_{hf} = 27.12$ MHz respectively, so the ratio of $f_{hf}/f_{lf} = 16$ here. The overlapping of high frequency on low frequency is significant at the time of low frequency sheath expansion and collapse. As a result, the quasi-neutrality breaks down when the modulation of high frequency on low frequency is strong that causes the launching of wave near sheath edge at multiple times during an RF period. The spatiotemporal profile of electric field indicates the presence of strong field reversal regions near the sheath edge. The field reversal regions are present when high frequency sheath expands and collapses during the low frequency sheath expansion and retreats towards electrode. In dual-frequency case the field reversal is present at multiple times near to the sheath edge.

6.5 Future Work

As we discussed, waves in single-frequency capacitively coupled plasma discharges starts near the sheath edge, travel towards bulk plasma and finally damp and disappear. The future work in single-frequency case aims:

- to develop a theoretical explanation for wave phenomenon and field reversal which lies near modified sheath region during the sheath expansion, as obtained from our PIC simulation.

It is well known that dual frequency discharges are attractive because the high frequency source can sustain the plasma and control the ion flux while the low frequency source can control the sheath voltage and the mean ion bombarding energy. Thus it is possible to control both the ion flux and ion energy independently, which is especially desirable for dielectric etch applications. We have observed strong amplitudes waves, field reversal effect and electron trapping in dual-frequency discharges. In dual-frequency case, future work is :

- to develop an analytical model for wave phenomena and field reversal.
- investigation of the effect of electron elastic collisions on waves.

Bibliography

[1] E. Kawamura, M. A. Lieberman, and A. J. Lichtenberg, "Stochastic heating in single and dual frequency capacitive discharges," *Phys. Plasmas*, vol. 13, p. 053506, 2006.

[2] A. Bogaerts, E. Neyts, R. Gijbels, and J. van der Mullen, "Gas discharge plasmas and their applications," *Spectrochimica Acta Part B: Atomic Spectroscopy*, vol. 57(4), pp. 609–658, 2001.

[3] D. M. Manos and D. L. Flamm, "Plasma etching: An introduction," *Academic Press, New York*, 1989.

[4] A. Grill, "Cold plasma in material fabrication: from fundamentals to applications," *IEEE Press, New York*, 1994.

[5] S. Samukawa and T. Mieno, "Pulse-time modulated plasma discharge for highly selective, highly anisotropic and charge-free etching," *Plasma Sources Sci. Technol.*, vol. 5, pp. 132–138, 1996.

[6] M. A. Lieberman and A. J. Lichtenberg, "Principles of plasma discharges and materials processing," *Wiley, New York*, 2005.

[7] M. A. Lieberman, "Plasma discharges for materials processing and display applications," *in: H. Schluter, A. Shivarova (Eds.), Advanced Technologies Based on Wave and Beam Generated Plasmas, NATO Science Series,*, vol. 67, Kluwer, Dordrecht, pp. 1–22, 1999.

[8] D. M. Manos and D. L. Flamm, "Plasma etching, an introduction," *Academic Press, San Diego, CA*, 1988.

[9] L. Martinu and D. Poitras, "Plasma deposition of optical films and coatings," *J. Vac. Sci. Technol. A*, vol. 18, p. 2619, 2000.

[10] J. W. Coburn and H. F. Winters, "Plasma-assisted etching in microfabrication," *Ann. Rev. Mater. Sci.*, vol. 13, p. 91, 1983.

[11] B. Chapman, "Glow discharge processes," *Wiley-Interscience, New York*, 1980.

[12] A. Anders, "Handbook of plasma immersion ion implantation and deposition," *John Wiley & Sons (New York)*, 2000.

[13] T. Lafleur, R. W. Boswell, and J. P. Booth, "Enhanced sheath heating in capacitively coupled discharges due to non-sinusoidal voltage waveforms," *Applied Phys. Lett.*, vol. 100(19), p. 194101, 2012.

[14] T. Lafleur and J. P. Booth, "Control of ion flux and ion energy in ccp discharges using non-sinusoidal voltage waveforms," *J. Phys. D: Appl. Phys.*, vol. 45, p. 395203, 2012.

[15] T. Lafleur, P. A. Delattre, E. V. Johnson, and J. P. Booth, "Separate control of ion flux and ion energy in capacitively coupled radio-frequency

discharges using voltage waveform tailoring," *Applied Phys. Lett.*, vol. 101, p. 124104, 2012.

[16] F. W. Perkins, "Radiofrequency sheaths and impurity generation by icrf antennas," *Nucl. Fusion*, vol. 29(4), p. 583, 1989.

[17] J. R. Myra, D. A. D'Ippolito, and M. J. Gerver, "Faraday screen sheaths and impurity production during ion cyclotron heating," *Nucl. Fusion*, vol. 30(5), p. 845, 1990.

[18] R. Van Nieuwenhove and G. Van Oost, "Experimental study of sheath currents in the scrape-off layer during icrh on textor," *Plasma Phys. Controlled Fusion*, vol. 34(4), p. 525, 1992.

[19] F. W. Perkins *Bull. Am. Phys. Soc.*, vol. 34, p. 2093, 1989.

[20] J. R. Myra and D. A. D'Ippolito *Bull. Am. Phys. Soc.*, vol. 37, p. 1602, 1992.

[21] D. A. D'Ippolito, J. R. Myra, M. Bures, and J. Jacquinot, "A model of sheath-driven impurity production by icrf antennas," *Plasma Phys. Controlled Fusion*, vol. 33(6), p. 607, 1991.

[22] D. A. D'Ippolito, J. R. Myra, J. Jacquinot, and M. Bures *Proceedings of the Ninth Topical Conference on Radio Frequency Power in Plasmas, Charleston, SC (American Institute of Physics, New York)*, p. 177, 1992.

[23] H. L. Berk, D. D. Ryutov, and Y. A. Tsidulko, "Temperaturegradient instability induced by conducting end walls," *Phys. Fluids B*, vol. 3(6), p. 1346, 1991.

[24] X. Garbet, L. Laurent, J.-P. Roubin, and A. Samain, "A model for the turbulence in the scrape-off layer of tokamaks," *Nucl. Fusion*, vol. 31(5), p. 967, 1991.

[25] J. R. Myra and D. A. D'Ippolito, "Resonance cone interaction with a self-consistent radio-frequency sheath," *Phys. Rev. Lett.*, vol. 101, p. 195004, 2008.

[26] Y. P. Raizer, "Gas discharge physics," *Springer-Verlag (Berlin)*, 1991.

[27] P. Chabert and N. Braithwaite, "Physics of radio-frequency plasmas," *Cambridge University Press*, 2011.

[28] V. A. Godyak, "Statistical heating of electrons at an oscillating plasma boundary," *Sov. Phys. - Tech. Phys.*, vol. 16(7), pp. 1073–1076, 1972.

[29] V. A. Godyak, "Steady-state low-pressure rf discharge," *Sov. J. Plasma Phys.*, vol. 2, p. 78, 1976.

[30] M. A. Lieberman, "Analytical solution for capacitive rf sheath," *IEEE Trans. Plasma Sci.*, vol. 16(6), p. 638, 1988.

[31] I. D. Kaganovich and L. D. Tsendin, "The space-time-averaging procedure and modeling of the rf diacharge, part ii: Model of collisional low-pressure rf discharge," *IEEE Trans. Plasma Sci.*, vol. 20(2), pp. 66–75, 1992.

[32] V. A. Godyak *Soviet Radio Frequency Discharge Research, Delphic Associates in Falls Church*, vol. VA, 1986.

[33] V. A. Godyak and O. A. Popov, "Experimental investigation of resonant rf discharge," *Sov. J. Plasma Phys.*, vol. 5, p. 227, 1979.

[34] I. D. Kaganovich, "Anomalous capacitive sheath with deep radio - frequency electric-field penetration," *Phys. Rev. Lett.*, vol. 89, p. 265006, 2002.

[35] D. Bohm, "Minimum ionic kinetic energy for a stable sheath," *The Characteristics of Electrical Discharges in Magnetic Fields, MacGraw-Hill, New York*, vol. Chapter 3, pp. 77–86, 1949.

[36] K. U. Riemann, "The bohm criterion and sheath formation," *J. Phys. D: Appl. Phys.*, vol. 24, p. 493, 1991.

[37] F. F. Chen, "Introduction to plasma physics," *Plenum Press, New York and London*, 1974.

[38] K. U. Riemann, "The bohm criterion and boundary conditions for a multicomponent system," *IEEE Transactions on Plasma Science*, vol. 23, p. 709, 1995.

[39] L. D. Landau, "On the vibration of the electronic plasma," *J. Phys. (USSR)*, vol. 10, p. 25, 1946.

[40] A. I. Akhiezer and A. S. Bakai *Sov. Phys. Dokl.*, vol. 16, p. 1065, 1971.

[41] M. Surendra and D. B. Graves, "Particle simulations of radio-frequency glow discharges," *IEEE Trans. Plasma Sci.*, vol. 19, p. 144, 1991.

[42] M. M. Turner, "Pressure heating of electrons in capacitively coupled rf discharges," *Phys. Rev. Lett.*, vol. 75, pp. 1312–1315, 1995.

[43] G. Gozadinos, M. M. Turner, and D. Vender, "Collisionless electron heating by capacitive rf sheaths," *Phys. Rev. Lett.*, vol. 87, p. 135004, 2001.

[44] V. A. Godyak and R. B. Piejak, "Abnormally low electron energy and heating-mode transition in a low-pressure argon rf discharge at 13.56 mhz," *Phys. Rev. Lett.*, vol. 65, p. 996, 1990.

[45] F. Schneider and Z. Angew, "Mechanish of h.f. discharge between plane plates," *Phys.*, vol. 6, p. 456, 1954.

[46] H. S. Butler and G. S. Kino, "Plasma sheath formation by radiofrequency fields," *Phys. Fluids*, vol. 6, p. 1346, 1963.

[47] M. Klick, "Nonlinearity of the radio-frequency sheath," *J. Appl. Phys.*, vol. 79, p. 3445, 1996.

[48] E. Fermi, "On the origin of the cosmic radiation," *Phys. Rev.*, vol. 75, p. 1169, 1949.

[49] J. M. Keller and W. B. Pennebaker, "Electrical-properties of rf sputtering systems," *IBM J. Res. Develop*, vol. 23, p. 3, 1979.

[50] U. Buddemeier, U. Kortshagen, and I. Pukropski, "On the efficiency of the electron sheath heating in capacitively coupled radio frequency discharges in the weakly collisional regime," *Appl. Phys. Lett.*, vol. 67(2), pp. 191–193, 1995.

[51] C. G. Goedde, A. J. Lichtenberg, and M. A. Lieberman, "Self-consistent stochastic electron heating in radio frequency discharges," *J. Appl. Phys.*, vol. 64(9), pp. 4375–4383, 1988.

[52] M. J. Kushner, "Montecarlo simulation of electron properties in rf parallel plate capacitively coupled discharges," *J. Appl. Phys.*, vol. 54(9), pp. 4958–4965, 1983.

[53] M. J. Kushner, "Mechanisms for power deposition in ar/sih$_4$ capacitively coupled rf discharges," *IEEE Trans. Plasma Sci.*, vol. 14(2), p. 188, 1986.

[54] A. E. Wendt and W. N. G. Hitchon, "Electron heating by sheaths in radio frequency discharges," *J. Appl. Phys.*, vol. 71(10), pp. 4718–4726, 1992.

[55] M. Surendra and D. B. Graves, "Electron acoustic waves in capacitively coupled, low-pressure rf glow discharges," *Phys. Rev. Lett.*, vol. 66(11), p. 1469, 1991.

[56] M. Surendra and M. Dalvie, "Moment analysis of rf parallel-plate-discharge simulations using the particle-in-cell with monte carlo collisions technique," *Phys. Rev. E*, vol. 48(5), p. 3914, 1993.

[57] M. M. Turner, "Collisionless heating in capacitively-coupled radio frequency discharges," *Electron Kinetics and Applications of Glow Discharges, edited by U. Kortshagen and L. D. Tsendin(Plenum Press, New York) NATO ASI Series B*, vol. 367, 1998.

[58] G. Gozadinos, D. Vender, M. M. Turner, and M. A. Lieberman, "Collisionless electron heating by capacitive radio-frequency plasma sheaths," *Plasma Sources Sci. Technol.*, vol. 10, p. 117, 2001.

[59] D. Vender and R. W. Boswell, "Electron-sheath interaction in capacitive radio-frequency plasmas," *J. Vac. Sci. Technol. A*, vol. 10(4), pp. 1331–1338, 1992.

[60] T. Mussenbrock and R. P. Brinkmann, "Nonlinear electron resonance heating in capacitive radio frequency discharges," *Appl. Phys. Lett.*, vol. 88(15), p. 151503, 2006.

[61] T. Mussenbrock and R. P. Brinkmann, "Nonlinear plasma dynamics in capacitive radio frequency discharges," *Plasma Sources Sci. Technol.*, vol. 16(2), p. 377, 2007.

[62] U. Czarnetzki, T. Mussenbrock, and R. P. Brinkmann, "Self-excitation of the plasma series resonance in radio-frequency discharges: An analytical description," *Phys. Plasmas*, vol. 13, p. 123503, 2006.

[63] M. A. Lieberman, A. J. Lichtenberg, E. Kawamura, T. Mussenbrock, and R. P. Brinkmann, "The effects of nonlinear series resonance on ohmic and stochastic heating in capacitive discharges," *Phys. Plasmas*, vol. 15(6), p. 063505, 2008.

[64] T. Mussenbrock, R. P. Brinkmann, M. A. Lieberman, A. J. Lichtenberg, and E. Kawamura, "Enhancement of ohmic and stochastic heating by resonance effects in capacitive radio frequency discharges: A theoretical approach," *Phys. Rev. Lett.*, vol. 101, p. 085004, 2008.

[65] D. Ziegler, T. Mussenbrock, and R. P. Brinkmann, "Nonlinear dynamics of dual frequency capacitive discharges: a global model matched to an experiment," *Plasma Sources Sci. Technol.*, vol. 17, p. 045011, 2008.

[66] B. G. Heil, U. Czarnetzki, R. P. Brinkmann, and T. Mussenbrock, "On the possibility of making a geometrically symmetric rf-ccp discharge electrically asymmetric," *J. Phys. D: Appl. Phys.*, vol. 41(16), p. 165202, 2008.

[67] D. Vender and R. W. Boswell, "Numerical modeling of low-pressure rf plasmas," *IEEE Trans. Plasma Sci.*, vol. 18(4), pp. 725–732, 1990.

[68] S. K. Park and D. J. Economou, "Analysis of low pressure rf glow dis-

charges using a continuum model," *J. Appl. Phys.*, vol. 68(8), p. 3904, 1990.

[69] V. A. Godyak and N. Sternberg, "Dynamic model of the electrode sheaths in symmetrically driven rf discharges," *Phy. Rev. A*, vol. 42(4), p. 2299, 1990.

[70] T. J. Sommerer, W. N. G. Hitchon, R. E. P. Harvey, and J. E. Lawler, "Self-consistent kinetic calculations of helium rf glow discharges," *Phys. Rev. A*, vol. 43, pp. 4452–4472, 1991.

[71] R. W. Boswell and J. J. Morey, "Self-consistent simulation of a parallel plate rf discharge," *Appl. Phys. Lett.*, vol. 52, pp. 21–23, 1988.

[72] M. A. Lieberman, "Dynamics of a collisional, capacitive rf sheath," *IEEE Trans. Plasma Sci.*, vol. 17, pp. 338–341, 1989.

[73] D. B. Graves, "Fluid model simulations of a 13.56-mhz rf discharge: Time and space dependence of rates of electron impact excitation," *J. Appl. Phys.*, vol. 62(1), p. 88, 1987.

[74] P. Bletzinger and M. J. Flemming, "Impedance characteristics of an rf parallel plate discharge and the validity of a simple circuit model," *J. Appl. Phys.*, vol. 62(12), p. 4688, 1987.

[75] V. A. Godyak, R. B. Piejak, and B. M. Alexandrovich, "Electrical characteristics of parallel-plate rf diacharges in argon," *IEEE Trans. Plasma Sci.*, vol. 19(4), pp. 660–676, 1991.

[76] R. H. Bruce, "Ion response to plasma excitation frequency," *J. Appl. Phys.*, vol. 52(12), p. 7064, 1981.

[77] K. Köhler, D. E. Horne, and J. W. Coburn, "Frequency dependence of ion bombardment of grounded surfaces in rf argon glow discharges in a planar system," *J. Appl. Phys.*, vol. 58(9), p. 3350, 1985.

[78] M. Klick, "Resistive model of the rf discharge including additional dc currents and electrodes," *Phys. Rev. E*, vol. 1, pp. 591–603, 1993.

[79] L. Tonks, "The high frequency behavior of a plasma," *Phys. Rev.*, vol. 19, p. 1458, 1931.

[80] L. Tonks, "Plasma-electron resonance, plasma resonance and plasma shape," *Phys. Rev.*, vol. 38, p. 1219, 1931.

[81] A. Dattner, "Resonance densities in a cylindrical plasma column," *Phys. Rev. Lett.*, vol. 10, p. 205, 1963.

[82] J. V. Parker, J. C. Nickel, and R. W. Gould, "Resonance oscillations in a hot nonuniform plasma," *Phys. Fluids*, vol. 7, p. 1489, 1964.

[83] J. Taillet, "Resonance-sustained radio frequency discharges," *Am. J. Phys.*, vol. 37, p. 423, 1969.

[84] J. Schulze, B. G. Heil, D. Luggenhölscher, T. Mussenbrock, R. P. Brinkmann, and U. Czarnetzki, "Electron beams in asymmetric capacitively coupled radio frequency discharges at low pressures," *J. Phys. D: Appl. Phys.*, vol. 41, p. 042003, 2008.

[85] J. Schulze, Z. Donkó, B. G. Heil, D. Luggenhölscher, T. Mussenbrock, R. P. Brinkmann, and U. Czarnetzki, "Electric field reversals in the sheath region of capacitively coupled radio frequency discharges at different pressures," *J. Phys. D: Appl. Phys.*, vol. 41, p. 105214, 2008.

[86] J. Schulze, B. G. Heil, D. Luggenhölscher, and U. Czarnetzki, "Electron beams in capacitively coupled radio-frequency discharges," *IEEE Trans. Plasma Sci.*, vol. 36, p. 1400, 2008.

[87] T. Mussenbrock, D. Ziegler, and R. P. Brinkmann, "A nonlinear global model of a dual frequency capacitive discharge," *Phys. Plasmas*, vol. 13, p. 083501, 2006.

[88] C. K. Birdsall and A. B. Langdon, "Plasma physics via computer simulation," *Adam Hilger, Bristol*, 1991.

[89] R. W. Hockney and J. W. Eastwood, "Computer simulation using particles," *Adam Hilger, Bristol*, 1988.

[90] T. J. Sommerer, W. N. G. Hitchon, and J. E. Lawler, "Electron heating mechanisms in helium rf glow discharges: a self-consistent kinetic calculation," *Phys. Rev. Lett.*, vol. 63(21), p. 2361, 1989.

[91] I. D. Kaganovich, O. V. Polomarov, and C. E. Theodosiou, "Revisiting the anomalous rf field penetration into a warm plasma," *IEEE Trans. Plasma Sci.*, vol. 34(3), pp. 696–717, 2006.

[92] J. A. Bittencourt, "Fundamentals of plasma physics," *Springer-Verlag, New York*, 2004.

[93] G. G. Lister, "Low-pressure gas discharge modeling," *J. Phys. D: Appl. Phys.*, vol. 25, p. 1649, 1992.

[94] B. G. Heil, R. P. Brinkmann, and U. Czarnetzki, "A hybrid, one-dimensional model of capacitively coupled radio-frequency discharges," *J. Phys. D: Appl. Phys.*, vol. 41, p. 225208, 2008.

[95] F. H. Harlow, "A machine calculation method for hydrodynamic problems," *Los Alamos Scientific Laboratory report*, 1956.

[96] J. M. Dawson, "Thermal relaxation in a one-species, one-dimensional plasma," *Phys. Fluids*, vol. 7(3), p. 419, 1964.

[97] O. Buneman, "Fast numerical procedures for computer experiments on relativistic plasmas," *Relativistic Plasmas(The Coral Gables Conference), Benjamin, NY*, 1968.

[98] O. Buneman, "Experiments with a large 3-d, e-m particle code," *Bulletin of the American Physical Society*, vol. 20(10), p. 1328, 1975.

[99] O. Buneman, "Advance from 2d electrostatic to 3d electromagnetic particle simulation," *Computer Physics Communication*, vol. 12(1), p. 21, 1976.

[100] O. Buneman, C. W. Barnes, J. C. Green, and D. E. Nielsen, "Principles and capabilities of 3-d, e-m particle simulations," *Journal of Computational Physics*, vol. 38(1), p. 1, 1980.

[101] C. K. Birdsall, "Particle-in-cell charged-particle simulations, plus monte carlo collisions with neutral atoms, pic-mcc," *IEEE Trans. Plasma Sci.*, vol. 19(2), pp. 65–85, 1991.

[102] V. Vahedi, G. DiPeso, C. K. Birdsall, M. A. Lieberman, and T. D. Rognlien, "Capacitive rf discharges modelled by particle-in-cell monte carlo simulation. i: analysis of numerical techniques," *Plasma Sources Sci. Technol.*, vol. 2, pp. 261–272, 1993.

[103] V. Vahedi, C. K. Birdsall, M. A. Lieberman, G. DiPeso, and T. D. Rognlien, "Capacitive rf discharges modelled by particle-in-cell monte

carlo simulation. ii: Comparison with laboratory measurements of electron energy distribution functions," *Plasma Sources Sci. Technol.*, vol. 2, pp. 273–278, 1993.

[104] T. E. Nitschke and D. B. Graves, "Matching an rf sheath model to a bulk plasma model," *IEEE Trans. Plasma Sci.*, vol. 23(4), p. 717, 1995.

[105] K.-U. Riemann, "The influence of collisions on the plasma sheath transition," *Phys. Plasmas*, vol. 4(11), p. 4158, 1997.

[106] G. Gozadinos, D. Vender, and M. M. Turner, "Boundary conditions and particle loading for the modeling of a semi-infinite plasma," *Journal of Computational Physics*, vol. 172, pp. 348–355, 2001.

[107] M. Surendra and D. Vender, "Collisionless electron heating by radio-frequency plasma sheaths," *Appl. Phys. Lett.*, vol. 65(2), pp. 153–155, 1994.

[108] R. Chodura, "Plasma-wall transition in an oblique magnetic field," *Phys. Fluids*, vol. 25(9), pp. 1628–1633, 1982.

[109] L. D. Landau and E. M. Lifshitz *Electrodynamics of Continuous Media, Oxford, U.K: Pergamon*, 1960.

[110] A. J. Lichtenberg and M. A. Lieberman *Regular and Chaotic Dynamics, New York: Springer-Verlag*, 1992.

[111] S. M. Ulam, "On some statistical properties of dynamical systems, in," *Proc. 4th Berkeley Symp. Mathematical Ststistics Probability, Univ. California*, vol. 3, p. 315, 1961.

[112] G. M. Zaslavskii and B. V. Chirikov, "Mechanism for fermi acceleration in a one-dimensional case," *Sov. Phys. Dokl.*, vol. 9(11), pp. 989–992, 1965.

[113] A. Brahic, "Numerical study of a simple dynamical system," *Astron. Astrophys.*, vol. 12, p. 98, 1971.

[114] M. A. Lieberman and A. J. Lichtenberg, "Stochastic and adiabatic behavior of particles accelerated by periodic forces," *Phys. Rev. A*, vol. 5, p. 1852, 1972.

[115] A. J. Lichtenberg, M. A. Lieberman, and R. H. Cohen, "Fermi acceleration revisited," *Physica*, vol. 1D, p. 291, 1980.

[116] M. A. Lieberman and V. A. Godyak, "From fermi acceleration to collisionless discharge heating," *IEEE Trans. Plasma Sci.*, vol. 26(3), pp. 955–986, 1998.

[117] M. A. Lieberman, "The dynamics of fermi acceleration," *In Uwe Kortshagen and Lev D. Tsendin, editors, Electron Kinetics and Application of Glow Discharges*, vol. 367 of NATO ASI Series B, Plenum Press, New York, pp. 215–226, 1998.

[118] A. J. Lichtenberg, "Application of mapping dynamics to analysis of a capacitive rf discharge," *In Uwe Kortshagen and Lev D. Tsendin, editors, Electron Kinetics and Application of Glow Discharges*, vol. 367 of NATO ASI Series B, Plenum Press, New York, pp. 227–240, 1998.

[119] D. Gabor, E. A. Ash, and D. Dracott, "Langmuir's paradox," *Nature*, vol. 176, pp. 916–919, 1955.

[120] J. Pavkovich and G. S. Kino, "R.f. theory of the plasma sheath," *Proceedings of the VIth International Conference on Ionization Phenomena in Gases*, vol. 3, p. 39, 1963.

[121] R. W. Gould, "Radio frequency characteristics of the plasma sheath," *Phys. Lett.*, vol. 11, p. 236, 1964.

[122] H. M. Mayer, "Measurements with a wide-band probe," *Proceedings of the VIth International Conference on Ionization Phenomena in Gases*, vol. 4, pp. 129–134, 1964.

[123] V. A. Godyak, O. A. Popov, and A. H. Khanna, "Effective collision frequency of the electrons in rf discharge," *Sov. J. Plasma Phys.*, vol. 2, p. 560, 1976.

[124] A. I. Akhiezer and A. S. Bakai, "Stochastic plasma heating by rf fields," *Sov. J. Plasma Phys.*, vol. 2(4), pp. 359–361, 1976.

[125] Y. R. Alanakyan, "Fermi acceleration and rf particle heating," *Sov. Phys. - Tech. Phys.*, vol. 24(5), pp. 611–612, 1979.

[126] U. Kortshagen, C. Busch, and L. D. Tsendin, "On simplifying approaches to the solution of the boltzmann equation in spatially inhomogeneous plasmas," *Plasma Sources Sci. Technol.*, vol. 5, pp. 1–17, 1996.

[127] A. S. Smirnov and L. D. Tsendin, "The space-time-averaging procedure and modeling of the rf diacharge," *IEEE Trans. Plasma Sci.*, vol. 19(2), pp. 130–140, 1991.

[128] I. D. Kaganovich and L. D. Tsendin, "Low-pressure rf diacharge in the free-flight regime," *IEEE Trans. Plasma Sci.*, vol. 20(2), pp. 86–92, 1992.

[129] I. D. Kaganovich, V. I. Kolobov, and L. D. Tsendin, "Stochastic electron heating in bounded radio-frequency plasmas," *Appl. Phys. Lett.*, vol. 69(25), pp. 3818–3820, 1996.

[130] Z. Wang, A. J. Lichtenberg, and R. H. Cohen, "Space-averaged kinetic analysis of stochastically heated electropositive and electronegative rf capacitive discharges," *Plasma Sources Sci. Technol.*, vol. 8, pp. 151–161, 1999.

[131] U. Buddemeier and I. D. Kaganovich, "Collisionless electron heating in rf gas discharges: Ii. the role of collisions and non-linear effects," *In Uwe Kortshagen and Lev D. Tsendin, editors, Electron Kinetics and Application of Glow Discharges*, vol. 367 of NATO ASI Series B, Plenum Press, New York, pp. 283–291, 1998.

[132] O. A. Popov and V. A. Godyak, "Power dissipated in low-pressure radio-frequency discharge plasmas," *J. Appl. Phys.*, vol. 57, p. 53, 1985.

[133] V. A. Godyak, R. B. Piejak, and B. M. Alexandrovich, "Measurement of electron energy distribution in low-pressure rf discharges," *Plasma Sources Sci. Technol.*, vol. 1(1), pp. 36–58, 1992.

[134] M. J. Colgan, N. Kwon, Y. Li, and D. E. Murnick, "Time- and space-resolved electron-impacy excitation rates in an rf glow discharge," *Phys. Rev. Lett.*, vol. 66, pp. 1858–1861, 1991.

[135] T. Gans, V. S. von der Gathen, and H.-F. Döbele, "Spectroscopic measurements of phase-resolved electron energy distribution function in rf-excited discharges," *Europhys. Lett.*, vol. 66, pp. 232–238, 2004.

[136] T. Gans, J. Schulze, D. O'Connell, U. Czarnetzki, R. Faulkner, A. R. Ellingboe, and M. M. Turner, "Frequency coupling in dual-frequency capacitively coupled radio-frequency discharges," *Appl. Phys. Lett.*, vol. 89, p. 261502, 2006.

[137] J. Schulze, B. G. Heil, D. Luggenhölscher, R. P. Brinkmann, and U. Czarnetzki, "Stochastic heating in asymmetric capacitively coupled rf discharges," *J. Phys. D: Appl. Phys.*, vol. 41, p. 195212, 2008.

[138] M. Surendra, D. B. Graves, and I. J. Morey, "Electron heating in low-pressure rf glow discharges," *Appl. Phys. Lett.*, vol. 56(11), pp. 1022–1024, 1990.

[139] D. Vender, "Numerical studies of the low-pressure rf plasmas," *Ph.D. dissertation, The Australian National University, Canberra*, 1990.

[140] A. H. Sato and M. A. Lieberman, "Electron-beam probe measurements of electric fields in rf discharges," *J. Appl. Phys.*, vol. 68, p. 6117, 1990.

[141] M. Surendra, "Radiofrequency discharge banchmark model comparison," *Plasma Sources Sci. Technol.*, vol. 4, pp. 56–73, 1995.

[142] G. W. Hammett and F. W. Perkins, "Fluid moment models for landau damping with application to the ion-temperature-gradient instability," *Phys. Rev. Lett.*, vol. 25, p. 3019, 1990.

[143] R. P. Brinkmann, "Beyond the step model: Approximate expressions for the field in the plasma boundary sheath," *J. Appl. Phys.*, vol. 102, p. 093303, 2007.

[144] R. P. Brinkmann, "From electron depletion to quasi-neutrality: the sheathbulk transition in rf modulated discharges," *J. Phys. D: Appl. Phys.*, vol. 42, p. 194009, 2009.

[145] F. Finger, U. Kroll, V. Viret, A. Shah, W. Beyer, X. M. Tang, J. Weber, A. Howling, and C. Hollenstein, "Influences of a high excitation frequency (70 mhz) in the glow discharge technique on the process plasma

and the properties of hydrogenated amorphous silicon," *J. Appl. Phys.*, vol. 71(11), p. 5665, 1992.

[146] A. A. Howling, J. L. Dorier, C. Hollenstein, U. Kroll, and F. Finger, "Frequency effects in silane plasmas for plasma enhanced chemical vapor deposition," *J. Vac. Sci. Technol. A*, vol. 10, p. 1080, 1992.

[147] J. Dutta, U. Kroll, P. Chabloz, A. Shah, A. A. Howling, J. L. Dorier, and C. Hollenstein, "Dependence of intrinsic stress in hydrogenated amorphous silicon on excitation frequency in a plasmaenhanced chemical vapor deposition process," *J. Appl. Phys.*, vol. 72(7), p. 3220, 1992.

[148] V. Vahedi, C. K. Birdsall, M. A. Lieberman, G. DiPeso, and T. D. Rognlien, "Verification of frequency scaling laws for capacitive radio-frequency discharges using two-dimensional simulations," *Phys. Fluids B*, vol. 5, pp. 2719–2729, 1993.

[149] S. Rauf and M. J. Kushner, "Nonlinear dynamics of radio frequency plasma processing reactors powered by multifrequency sources," *IEEE Trans. Plasma Sci.*, vol. 27(5), pp. 1329–1338, 1999.

[150] K. Bera, D. Hoffman, S. Shannon, G. Delgadino, and Y. Ye, "Frequency optimization for capacitively coupled plasma source," *IEEE Trans. Plasma Sci.*, vol. 33(2), pp. 382–383, 2005.

[151] J. Borovsky, "The dynamic sheath: objects coupling to plasmas on electron-plasma frequency time scales," *Phys. Fluids*, vol. 31, pp. 1074–1100, 1988.

[152] Y. M. Aliev, I. D. Kaganovich, and H. Schl´uter, "Collisionless electron heating in rf gas discharges: I. quasilinear theory," *In Uwe Kortshagen*

and Lev D. Tsendin, editors, Electron Kinetics and Application of Glow Discharges, vol. 367 of NATO ASI Series B, Plenum Press, New York, pp. 257–281, 1998.

[153] Y. M. Aliev, I. D. Kaganovich, and H. Schl′uter, "Quasilinear theory of collisionless electron heating in radio frequency gas discharges," *Phys. Plasmas*, vol. 4(7), pp. 2413–2421, 1997.

[154] F. F. Chen, "Introduction to plasma physics and controlled fusion," *Plenum Press, New York and London*, 1984.

[155] B. Tsurutani and G. Lakhina, "Some basic concepts of wave-particle interactions in collisionless plasmas," *Reviews of Geophysics*, vol. 35(4), pp. 491–502, 1997.

[156] I. B. Berstein, J. M. Greene, and M. D. Kruskal, "Exact nonlinear plasma oscillations," *Phys. Rev.*, vol. 108(3), pp. 546–550, 1957.

[157] G. Manfredi, "Long-time behavior of nonlinear landau damping," *Phys. Rev. Lett.*, vol. 79(15), pp. 2815–2818, 1997.

[158] M. V. Medvedev, P. H. Diamond, M. N. Rosenbluth, and V. I. Shevchenko, "Asymptotic theory of nonlinear landau damping and particle trapping in waves of finite amplitude," *Phys. Rev. Lett.*, vol. 81(26), pp. 5824–5827, 1998.

[159] T. Gans, V. Schulz-von der Gathen, and H. F. Döbele, "Prospects of phase resolved optical emission spectroscopy as a powerful diagnostic tool for rf-discharges," *Contrib. Plasma Phys.*, vol. 44, pp. 535–540, 2004.

[160] D. O'Connell, T. Gans, D. Vender, U. Czarnetzki, and R. Boswell, "Plasma ionization through wave-particle interaction in a capacitively

coupled radio-frequency discharge," *Phys. Plasmas*, vol. 14(3), p. 034505, 2007.

[161] D. O'Connell, T. Gans, A. Meige, P. Awakowicz, and R. W. Boswell, "Plasma ionization in low-pressure radio-frequency discharges - part i: Optical measurements," *IEEE Trans. Plasma Sci.*, vol. 36(4), p. 1382, 2008.

[162] A. Meige, D. O'Connell, T. Gans, and R. W. Boswell, "Plasma ionization in low-pressure radio-frequency discharges - part ii: Particle-in-cell simulation," *IEEE Trans. Plasma Sci.*, vol. 36(4), p. 1384, 2008.

[163] I. D. Kaganovich, "Effects of collisions and particle trapping on collisionless heating," *Phys. Rev. Lett.*, vol. 82(2), pp. 327–330, 1999.

[164] T. Gans, C. C. Lin, V. Schulz-von der Gathen, and H. F. Döbele, "Phase-resolved emission spectroscopy of a hydrogen rf discharge for the determination of quenching coefficients," *Phys. Rev. A, Gen. Phys.*, vol. 67(1), p. 012707, 2003.

[165] M. M. Turner and M. B. Hopkins, "Anomalous sheath heating in a low pressure rf discharge in nitrogen," *Phys. Rev. Lett.*, vol. 69(24), pp. 3511–3514, 1992.

[166] U. Czarnetzki, D. Luggenholscher, and H. F. Döbele, "Space and time resolved electric field measurements in helium and hydrogen rf-discharges," *Plasma Sources Sci. Technol.*, vol. 8(2), pp. 230–248, 1999.

[167] R. A. Gottscho, "Glow-discharge sheath electric fields: negative-ion, power, and frequency effects," *Phys. Rev. A, Gen. Phys.*, vol. 36(5), pp. 2233–2242, 1987.

[168] B. P. Wood, M. A. Lieberman, and A. J. Lichtenberg, "Sheath motion in a capacitively coupled radio frequency discharge," *IEEE Trans. Plasma Sci.*, vol. 19(4), pp. 619–627, 1991.

[169] C. Ramsauer, "Über den wirkungsquerschnitt der gasmoleküle gegenüber lengsomen electronen," *I-Fortsetzung, Ann. Phys. (Lpz)*, vol. 66, pp. 546–561, 1921.

[170] R. E. Brode, "The absorption coefficient for slow electrons in gases," *Phys. Rev.*, vol. 25, pp. 636–644, 1925.

[171] R. E. Brode, "The absorption coefficient for slow electrons in gases," *Rev. Mod. Phys.*, vol. 5, pp. 257–292, 1933.

[172] S. Trajmar and J. W. McKonkey, "Benchmark measurements of cross sections for electron collisions: Analysis of scattered electrons," *Advances in Atomic, Molecular, and Optical Physics, Bederson and Walther (eds.)*, vol. 33, pp. 63–89, 1994.

[173] A. Zecca, G. P. Karwasz, and R. S. Brusa, "One century of experiments on electron-atom and molecule scattering : A critical review of integral cross sections i. atoms and diatomic molecules," *La Rivista del Nuovo Cimento*, vol. 19, pp. 1–146, 1996.

[174] C. Yamabe, S. J. Buckman, and A. V. Phelps, "Measurement of free-free emission from low-energy-electron collisions with ar," *Phys. Rev. A*, vol. 27(3), pp. 1345–1352, 1983.

[175] A. Perret, P. Chabert, J. Jolly, and J. P. Booth, "Ion energy uniformity in high-frequency capacitive discharges," *Appl. Phys. Lett.*, vol. 86(2), p. 021501, 2005.

[176] H. H. Goto, H. D. Lowe, and T. Ohmi, "Dual excitation reactive ion etcher for low energy plasma processing," *J. Vac. Sci. Technol. A*, vol. 10(5), p. 3048, 1992.

[177] H. H. Goto, H. D. Lowe, and T. Ohmi, "Independent control of ion density and ion bombardment energy in a dual rf excitation plasma," *IEEE Trans. Semicond. Manuf.*, vol. 6(1), p. 58, 1993.

[178] J. Robiche, P. C. Boyle, M. M. Turner, and A. R. Ellingboe, "Analytical model of a dual frequency capacitive sheath," *J. Phys. D: Appl. Phys.*, vol. 36(5), pp. 1810–1816, 2003.

[179] J. P. Booth, C. S. Corr, G. A. Curley, J. Jolly, and J. Guillon, "Fluorine negative ion density measurement in a dual frequency capacitive etch reactor by cavity ring-down spectroscopy," *Appl. Phys. Lett.*, vol. 88, p. 151502, 2006.

[180] M. A. Worsley, S. F. Bent, N. C. M. Fuller, and T. Dalton, "Characterization of neutral species densities in dual frequency capacitively coupled photoresist ash plasmas by optical emission actinometry," *J. Appl. Phys.*, vol. 100(8), p. 083301, 2006.

[181] S. K. Karkari and A. R. Ellingboe, "Effect of radio-frequency power levels on electron density in a confined two-frequency capacitively-coupled plasma processing tool," *Appl. Phys. Lett.*, vol. 88(10), p. 101501, 2006.

[182] G. A. Curley, D. Maric, J. P. Booth, C. S. Corr, P. Chabert, and J. Guillon, "Negative ions in single and dual frequency capacitively coupled fluorocarbon plasmas," *Plasma Sources Sci. Technol.*, vol. 16, pp. S87–S93, 2007.

[183] J. Jolly and J. P. Booth, "Atomic hydrogen densities in capacitively coupled very high-frequency plasmas in h2 : Effect of excitation frequency," *J. Appl. Phys.*, vol. 97(10), p. 103305, 2005.

[184] P. C. Boyle, A. R. Ellingboe, and M. M. Turner, "Independent control of ion current and ion impact energy onto electrodes in dual frequency plasma devices," *J. Phys. D: Appl. Phys.*, vol. 37(5), pp. 697–701, 2004.

[185] H. C. Kim, J. K. Lee, and J. W. Shon, "Analytic model for a dual frequency capacitive discharge," *Phys. Plasmas*, vol. 10(11), pp. 4545–4551, 2003.

[186] M. M. Turner and P. Chabert, "Electron heating mode transitions in dual frequency capacitive discharges," *Appl. Phys. Lett.*, vol. 89(23), p. 231502, 2006.

[187] M. M. Turner and P. Chabert, "Collisionless heating in capacitive discharges enhanced by dual-frequency excitation," *Phys. Rev. Lett.*, vol. 96(20), p. 205001, 2006.

[188] M. M. Turner and P. Chabert, "Electron heating mechanisms in dual-frequency capacitive discharges," *Plasma Sources Sci. Technol.*, vol. 16(2), p. 364, 2007.

[189] M. M. Turner, "Collisionless heating in radio-frequency discharges: a review," *J. Phys. D: Appl. Phys.*, vol. 42(19), p. 194008, 2009.

[190] P. Chabert, P. Levif, J. L. Raimbault, J. M. Rax, M. M. Turner, and M. A. Lieberman, "Electron heating in multiple-frequency capacitive discharges," *Plasma Phys. Control. Fusion*, vol. 48(12B), p. B231, 2006.

[191] M. A. Lieberman, J. Kim, J. P. Booth, P. Chabert, J. M. Rax, and M. M. Turner *SEMI Technology Symposium, SEMICON Korea 2003*, pp. 31–37, 2003.

[192] R. N. Franklin, "The dual frequency radio-frequency sheath revisited," *J. Phys. D: Appl. Phys.*, vol. 36(21), p. 2660, 2003.